MICROSCOPIC DYNAMICS

OF AMYLOID β FIBRILLIZATION

by

Yuechuan Xu

A Dissertation Submitted to

William A. Brookshire Department of Chemical and Biomolecular Engineering,

College of Engineering

In Partial Fulfillment of the Requirements for the Degree of

Doctor of Philosophy

in Chemical Engineering

Chair of Committee: Peter G. Vekilov

Committee Member: Navin Varadarajan

Committee Member: Vassiliy Lubchenko

Committee Member: Dominique Maes

Committee Member: Peter G. Wolynes

Committee Member: Mehmet A. Orman

University of Houston

December 2021

Acknowledgements

I want to thank all of those who have helped and supported me along this journey, regardless of the magnitude. Thank you for shaping me into who I am today and witnessing what I have achieved.

I would like to express my most sincere gratitude to my advisor Dr. Peter Vekilov, who taught me the utmost importance of integrity, honesty, and being hard-working not only in academia but also in life. I am eternally grateful for the opportunity to work in the Vekilov lab to explore amyloid β, without which it would have been impossible for me to become the scientist, and the person I am today. You lead me into the world of scientific research and helped me develop and grow the amyloid β project while overcoming multiple challenges. I will continue to treat science and live life with respect and dedication the way you inspired me in the past 5 years.

I would like to thank all my committee members for all the valuable suggestions and discussions along the way. You helped me expand the perspectives on the amyloid β project and inspired me to explore aspects of the project that I did not think of, which ultimately shapes this project into much richer figure.

I would like to thank Dr. Peter Wolynes for continuously working with us to help us gain deeper insights into kinetics and thermodynamics of amyloid β fibrillization and understand many phenomena at the molecular level, as well as his group members, especially Kaitlin Knapp, for performing simulation studies to couple with our experiments. Our collaboration has resulted in multiple successful paper publications.

I would like to thank Dr. Patrick Cirino and Dr. Richard Willson for giving me access to their labs to perform all molecular biology related experiments of my project.

I would like to thank all my group members for always helping me and supporting me throughout the years; to Dr. Mohammad Safari, thank you for initiating the project with me, helping me produce the amyloid β peptide and all those long nights and gossiping; to Dr. Wenchuan Ma, thank you for helping me with AFM, countless lunches we had together, all the jokes we shared, all the laughs we had on your SQQQ holdings in year 2020, and the good relationship we came to have.

I would like to thank my parents for setting me up to be in the position where I am today. Thank you for always supporting me and believing in me.

Finally, I would like to thank my wife Yajie Jiang for always being there for me over the past 10 years. Thank you for taking care of our dog Ginger with me, who gave us unmeasurable joy during my graduate school career. Thank you for being the best mother to our daughter, Charlotte Lexi Xu, who is the best daughter I could possibly ask for. And yes, thank you, Charlie for being my little girl and bringing so much sunshine into my life. No words can explain how much I love you.

Abstract

Amyloid fibrils are β-sheet-rich protein assemblies, which could trigger various diseases, including Alzheimer's. One crucial step in searching for cures is to understand the aggregation mechanism; yet despite ever-developing techniques and tools, it remains poorly understood. Common experimental methods bear certain limitations. In this study, we employed time-resolved in situ scanning probe microscopy to directly probe the fibrillization pathway of amyloid-β 40, a short peptide believed to be responsible for Alzheimer's.

Amyloid plaque deposition is the hallmark of Alzheimer's. The fibrillization pathway is extraordinarily complex. Numerous fundamental questions remain unanswered. To elucidate the nature of the intermediate state for Aβ monomer incorporation into fibril, we employed time-resolved in situ atomic force microscopy to monitor the growth of single fibrils at various peptide and urea concentrations. We proved that AFM is a reliable tool for direct measurement of individual fibril growth rates. The growth rates do not correlate with the fibril thickness, indicating lack of cooperativity between adjacent protofilaments during growth. The opposite ends on a fibril grow at similar rates and are steady, in contrast to the "stop-and-go" mechanism. Most importantly, the bimolecular rate constant for monomer incorporation into fibril is significantly smaller than the diffusion limit, indicating an intermediate state with relatively high free energy. With urea in the system, we discovered that both the Aβ peptide solubility and the fibril growth rate constant increase. We attribute this behavior to the presence of a frustrated complex supported by nonnative contacts in the equilibrium structure of the fibril tip.

Further investigation of the role of frustrated complex in intermediate state focused on the "Dutch variant" E22QAβ, which is responsible for early-onset Alzheimer's. The E22QAβ peptide exhibits a lower solubility and a significantly higher growth rate constant, confirming the role of E22 residue in the frustrated contacts that impedes fibrillization. Fibrils nucleated on supported phospholipid bilayers were also investigated, for their distinct polymorphism and toxic nature, and possible relationship to a modified frustrated fibrillization intermediate state. We found that lipid bilayers interact with Aβ oligomers and fibrils, and different curvatures induce different polymorphisms and kinetics of fibrillization.

Table of Contents

List of Figures

Chapter 1: Protein Condensation Diseases

1.1 Protein Folding and Protein Aggregation Disease

1.1.1 Protein Structure Hierarchy

Proteins are large and complex molecules that play critical roles in the human body. They fold into stable conformations templated by amino acid sequences and local biological environments in order to perform normal functions, though unstructured proteins also play crucial roles in numerous areas (e.g., cell cycle control, transcriptional regulation, and transmembrane signal reception) [1–4]. The structure of a protein molecule increases in complexity following a primary-secondary-tertiary-quaternary hierarchy.

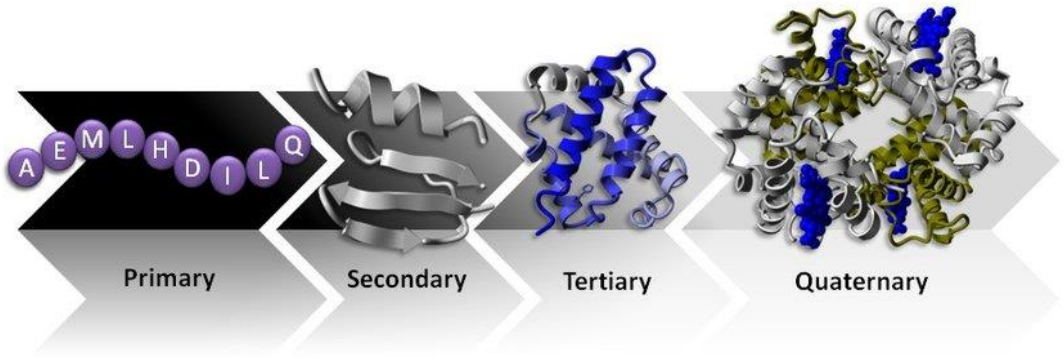

Fig. 1.1 Protein Structures.

Figure 1.1 Hierarchy of protein structures in the order of increasing complexity [5].

Primary structure is the most basic level of protein structure, determined by amino acid sequence and held by peptide bonds. Although the primary structure is usually represented in plain text consisting of letters for amino acid sequence, its importance should not be overlooked. It can be used, with the aid of computer modeling tools, to

predict the higher order structure and the folding pattern of a given amino acid sequence. If the folded structure of a certain polypeptide is unknown, another polypeptide with known structure and similar amino acid sequence could be a template for structural prediction [6].

The interactions formed between the atoms of the polypeptide backbone, excluding the side chains, are mostly hydrogen-bonding networks. These hydrogen bonds do not include any amino acid side chains in a polypeptide, which lead to local spatial conformations of polypeptide chains and such conformations are represented by coil-like α-helix and repeating β-sheet, defined as secondary structure. Secondary structures are important parts of the folding motifs that contribute to higher order structures like folds and domains that could perform specific functions (e.g., nucleotide-binding folds) [1, 7]. The secondary structure of a protein can be altered through either mutation in the amino acid sequence or external stress. Clinically, misfolded protein molecules in the form of repeated β-sheets could lead to amyloid fibrils and plaques deposition that leads to tissue and cell damage causing diseases (e.g., Alzheimer's disease and sickle cell anemia) and this will be the focus of this dissertation [7–10].

Tertiary structure builds up on secondary structure and involves interactions between side groups, which can be polar, non-polar, or charged. It coordinates the specific spatial arrangements of secondary structure and the locations of all functional groups of a single polypeptide chain. Most protein molecules contain compact units within a single polypeptide chain that define molecular stability and functional independence, called domains, which are a part of the tertiary structure (e.g., DNA-binding domain) [1, 2]. In a correctly folded protein molecule with tertiary structure, non-polar side chains mostly cluster at the inner core and hydrogen bonds and ionic bonds formed between other side

chains contribute to the overall 3-D structure, with disulfide bonds and covalent bonds as reinforcement [11].

A protein molecule with tertiary structure is capable of performing its normal function; however, a number of them rely on forming oligomers with other polypeptide chains to give rise to specific structures and complex functionalities, representing the highest level of complexity in protein structure, the quaternary structure (e.g., hemoglobin and antibodies) [1, 2, 12–14]. Not all proteins have quaternary structures and the subunits within a quaternary structure could be the same or different polypeptides.

1.1.2 Protein Folding

Protein folding is the process by which a polypeptide chain adopts its native structure, usually the conformation with the lowest free energy by which the protein molecule becomes functional. There had been controversies on how proteins fold and why they fold this way even more than half a century after Anfinsen *et al.* demonstrated protein folding as a straightforward biophysical process [15, 16]. Two major questions hovered at the beginning of the protein folding investigations: How can amino acid sequence determine the native structure of a protein? How can a protein fold so quickly despite countless possible conformations [17]? At the early stage of exploring protein folding, following Anfinsen's experiment which showed that ribonuclease could fold without any outside help rather quickly [16], researchers simply assumed that proteins fold through distinct pathway while transforming through distinct intermediate states and all proteins should find the native structure through a predetermined route instead of searching among the vast number of various structural options, albeit with no explanations as to why and how [15, 18, 19]. It became widely accepted after Anfinsen's experiments that the native

structure does not depend on the folding route or production or folding methods of the peptide, instead it only depends on the amino acid sequence and solution conditions [16, 17, 20, 21]. These works thus enabled in vitro protein folding research and indicated that natural selection can act to change an amino acid sequence and ultimately the native structure and the functionalities of proteins, but folding kinetics and thermodynamics are more of a physical chemistry matter [17].

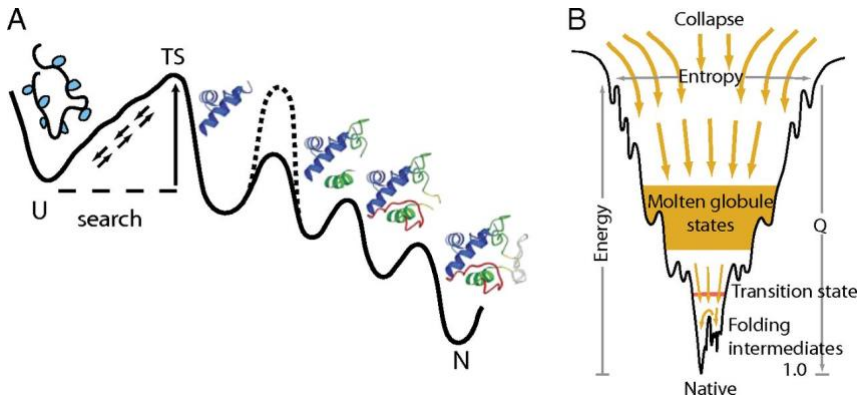

Fig. 1.2 Two Different Scenarios of Protein Folding Pathway.

Figure 1.2 **(A).** Free energy of a protein fold through distinct pathway. U, unfolded state; TS, transition state; N, native state. (**B).** Folding funnel. Protein fold through unknown routes and intermediate states [15, 22].

What led to the theoretical community to explore a new view of folding pathway was a realization that partially folded proteins were unable to equilibrate to a common structure and their ensemble nature [18, 19, 23–25]. The stochastic search of conformations before protein reaches native conformation screens through a vast number of irrelevant possible intermediate states, while the kinetic trap begins to project its impact of keeping

protein in the unfolded or native state within physiological environment [26, 27]. This stochastic idea of protein intermediate states reveals the concept of "energy landscape" or "folding funnel" as in Fig. 1.2B, in which folding properties can be related to free energy [24, 28, 29]. It was concluded that proteins must fold to native structures through many different routes and intermediate states. The folding kinetics should be regarded as a progressive collection of partially folded structures into an ensemble rather than a pre-determined single pathway of intermediate states [30]. They must fold energetically downhill, representing a decrease of total internal free energy, and narrow down horizontally, representing a decrease in accessible conformations in the scheme of a typical folding funnel [24, 28, 29]. And the landscape picture was filled by qualitative concepts derived from "energy landscape theory", independent of structural and thermodynamic information and could be applied to any protein or polymers of interest. Even without any constraints that could excluded some scenarios, it has been widely accepted that proteins fold through many independent pathways, regardless of predictability [15, 31, 32].

To travel from the top of the folding funnel to the bottom, proteins progress from unfolded state (U) to fully folded native state (N) while passing through many intermediate states which are hard to characterize, although the so-called compact intermediate "molten globule" state in which proteins exist in stable conformations bounded by certain conditions, is easily probed. The ideal unfolded protein should be a random coil, in which all possible conformations have similar free energies. Exceptions could be made when polypeptide chains come into too close proximity and between atoms close in the covalent structure, which could reduce local flexibility [33]. There are countless possible random coil conformations of a single protein, therefore it would be impossible to encounter a fully

unfolded protein on a finite timescale and also each protein molecule in a sample of fully unfolded proteins will probably adapt a unique conformation at any given instant of time. It would require time longer than the age of universe for a protein to sequentially survey all possible states before reaching the native conformation [34]. In order to characterize such a random initial stage, the environment must be satisfactory for proteins to adapt to nearly random states. Strong denaturants (e.g., 6 M Guanidine-HCl and 8 M urea) have been demonstrated to enforce proteins to have the average hydrodynamic properties of random coils. In these experiments, no non-random structures were observed except for a few small, random hydrophobic clusters, making the coil nearly random for experimental purposes [35–37]. There has been evidence, that other denaturing conditions without strong denaturants (e.g., extremes of pH or temperature) cannot make unfolded proteins true random coils because it is virtually impossible for all 20 amino acids with diverse chemical properties to establish balanced interactions within the polypeptide chain and with the solvent [38–41]. Nevertheless, unfolded states generated under different conditions are indistinguishable thermodynamically which could lead to a random spectrum of non-native conformations that can be used for experimental characterization purposes [38, 39, 42].

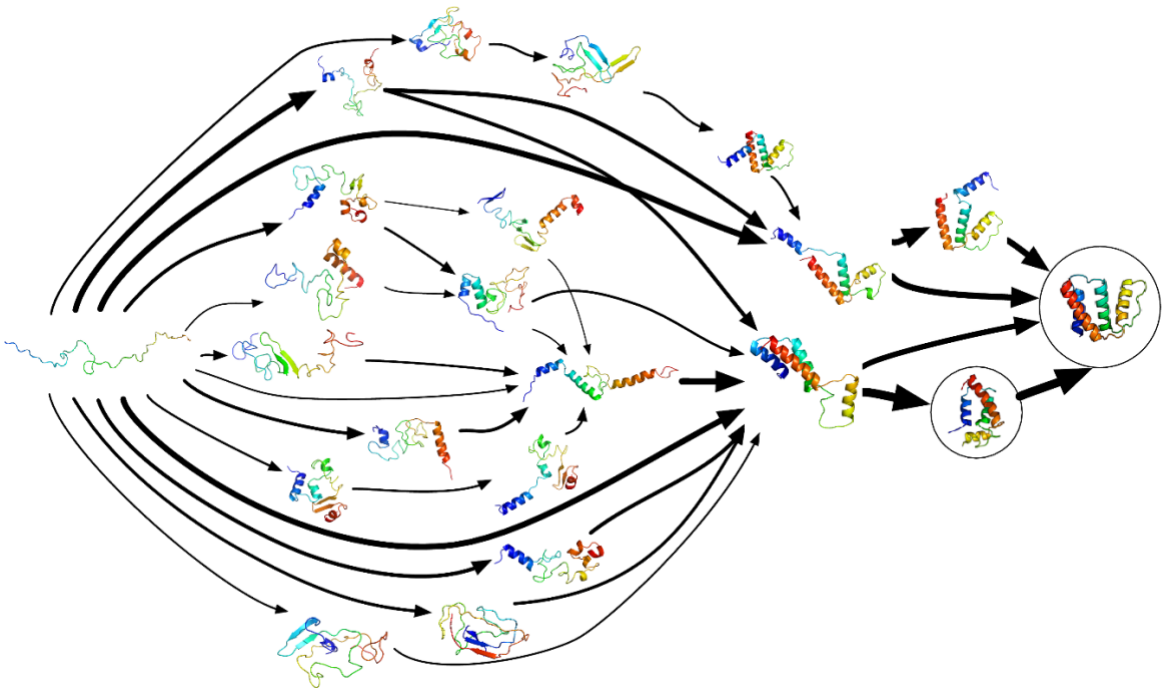

Fig. 1.3 Example of Protein Folding Pathways.

Figure 1.3 A Markov state model illustrating 15 of the highest flux folding pathways between the unfolded and native states of ACBP. Line thicknesses are proportional to pathway folding flux. The Markov state model contained 2000 macrostates [43].

The unfolded and native states for almost all proteins and those conformations that are stable at equilibrium conditions which are easily accessible and characterized. The intermediate states inside the folding funnel are rather hard to capture, as some of them are not thermodynamically stable or unable to equilibrate to a common structure [18, 19, 23–25, 33]. There exist proteins that have been observed under certain conditions could maintain stable conformations which are neither fully folded nor fully unfolded [33, 44, 45]. Several most common features among molten globules are as following, they are

thermodynamically stable, have similar backbone secondary content to native state but lack native tertiary structure, their enthalpy is closer to the fully unfolded state than to the native state and their interconversions with unfolded state are rapid while slow with the folded state [33, 44, 45]. Circular dichroism spectroscopy has been employed extensively to provide direct evidence on change of tertiary and secondary content in molten globules [46]. Changing pH by adding acids can induce protein unfolding and reach molten globule state, sometimes in combination with low concentration of urea or guanidine-HCl to further stabilize the molten globule [47, 48]. The molten globule state has enabled researchers gain more insights into the protein folding problems as it provides a stable intermediate state for probing.

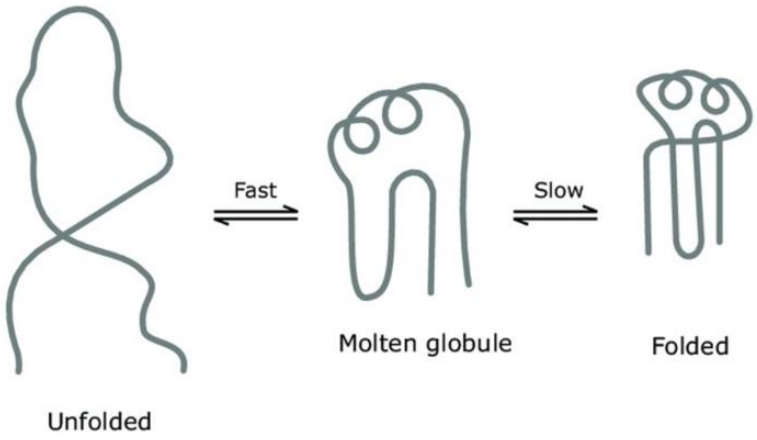

Fig. 1.4 Molten Globule Schematics.

Figure 1.4 The molten globule state is an intermediate state in the folding pathway when a polypeptide chain converts from an unfolded to a folded native state [49].

The native state is the correctly folded form of proteins by which they can perform their normal biological functions. The native conformations of proteins have been investigated and known in great details thanks to technique like X-ray crystallography and nuclear magnetic resonance (NMR) but the scope is not within the discussions in this thesis [33, 50, 51]. One process by which proteins fold is called hydrophobic collapse. This theory states that in the early stages of folding, polypeptide chain forms initial secondary structures, creating locally rich hydrophobic areas. As the protein molecule interacts with aqueous solvent, the inability of interacting with solvent causes these hydrophobic regions to cluster and collapse into a tertiary conformation with a hydrophobic core that is shielded by outside hydrophilic residues [52, 53]. Hydrophobic collapse can be visualized as a part of the folding funnel theory that leads proteins to their lowest accessible free energy state. To describe it in the context of thermodynamics and only consider the side chain contributions (polypeptide backbone maintains stability by extensive hydrogen bonding networks within the backbone) [54], polar polypeptide side chains can form hydrogen bonds with solvent, maintaining the stability of structure within localized segments of the polypeptide whereas hydrophobic side chains cannot establish any significant interactions, leading to a decreased entropy of the overall system. By clustering the hydrophobic regions, the solvent can significantly reduce surface area exposed to non-polar side chains thus reduces those areas of decreased entropy. Through this process, the individual flexibility and entropy of the polypeptide chain decreases; however, the dissociative degrees of freedom available to the molecules and the overall entropy of the system increases, resulting in a thermodynamically favorable folded polypeptide [55–57].

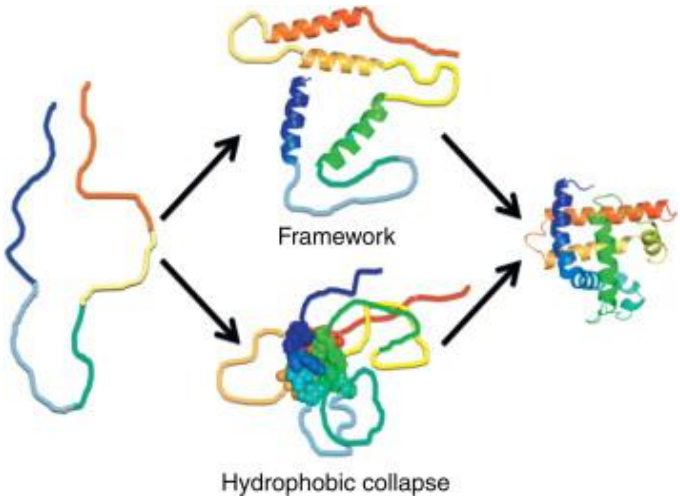

Fig. 1.5 Illustration of the Extreme Interpretations of the Hydrophobic Collapse Models.

Figure 1.5 The bottom structure, with burial of hydrophobic side chains and no explicit secondary structure, corresponds to the hydrophobic collapse model [56].

In an ideal case, all proteins would fold to their native state and perform their designated functions; however, this is not always the case. What happens when proteins do not fold the way they should?

1.1.3 Protein Aggregation Disease

A protein is considered misfolded when it cannot reach its normal, native state. There could be a wide spectrum of underlying causes, some are relatively easier to identify (e.g., mutations) while some requires more in-depth research, though without guaranteed answers [58]. Proteins in the human body misfold more frequently than to our liking and the cells do have multiple established mechanisms to combat these problems. Chaperones, in addition to their widely known function of aiding protein folding, can be further induced

in response to abnormal accumulation of unfolded or misfolded proteins. They constantly respond to perturbations and play crucial roles in aiding misfolded proteins to reestablish the correct conformations [59, 60]. In the cases when misfolded proteins cannot be properly refolded, proteasome, autophagy and degradation mechanisms will be deployed to degrade and clean up these misfolded proteins [60–62]. Any dysfunction of these mechanisms will interrupt the refolding or clearance processes of misfolded protein, which potentially could lead to protein aggregation and ultimately protein aggregation disease.

Misfolding, as mentioned, is influenced by amino acid sequence, which is why a mutation-related cause is easier to be identified [63, 64]. Moreover, misfolding is also influenced by bewildering non-genetic conditions that leads to irregular pH, temperature, and stressed environment, engendering accelerated loss of native conformations [65–67]. This process usually leads proteins into a thermodynamically unfavorable state and by the nature of seeking lower free energy levels and more stability, proteins tend to form aggregations. From the hydrophobic collapse standpoint, when hydrophobic patches of the polypeptides cannot bury themselves properly, they are more likely to aggregate with other hydrophobic patches in the proximity, thus protein aggregations arise [57, 68]. In terms of how protein misfolding causes disease, there are five major pathways: improper degradation, improper localization, dominant-negative mutations, gain of toxic function and amyloid accumulation [69–73].

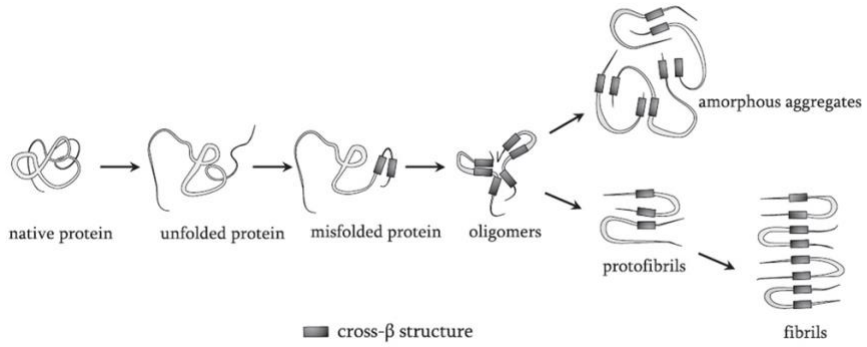

Fig. 1.6 Example of Protein Misfolding and Aggregation through Amyloidosis.

Figure 1.6 Under certain circumstances proteins undergo conformational changes that result in unfolding and partial misfolding that are associated with the tendency to aggregate. [68].

This thesis will focus on the amyloid formation pathway as AD is closely related to it. Amyloidosis causes protein aggregate to accumulate in organs or tissues and could be either hereditary or acquired, all of which are important aspects of AD. We will discuss this in detail in the following chapters.

1.2 Alzheimer's Disease

Alzheimer's disease (AD) is the most common cause of dementia, and it is not a normal part of aging. It affects more than 6 million Americans of ages 65+ and as the number of elderly Americans grows rapidly due to aging society as a whole, this number is expected to reach 12.7 million barring an effective cure or treatment. The mortality rate among elderlies is roughly 1/3, exceeding breast and prostate cancer combined. Caregiving for AD patients not only takes a huge toll on individual families but also on society, costing

355 billion dollars on the national level. AD is most common among the age group of 65 and up but it does not negate the fact that early-onset AD also makes up a huge portion of total AD cases, although the cause and pathology may be different. On the global level, AD affects more than 44 million people, and the caregiving situation is even more challenging in some parts of the world. The world urgently needs a cure or treatment of AD [74, 75].

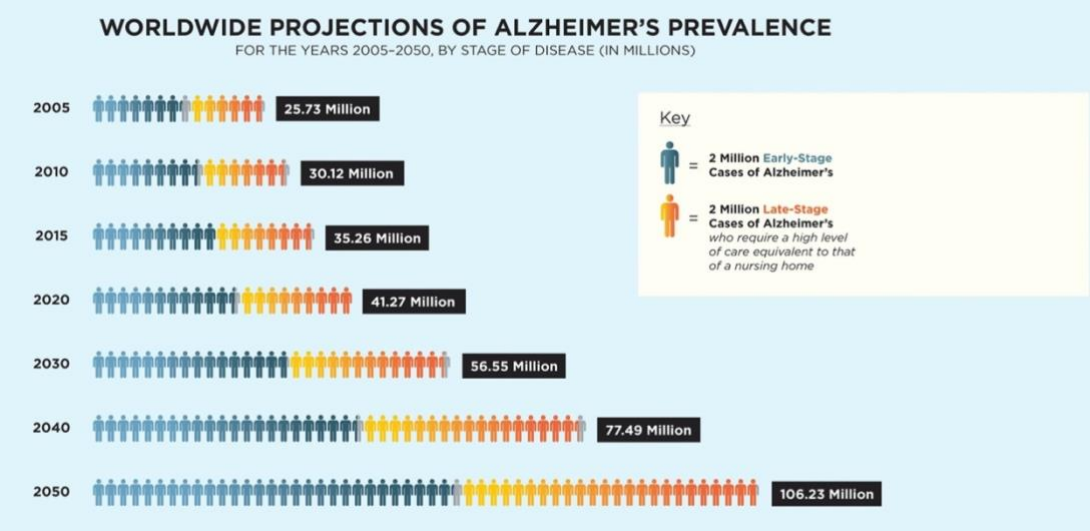

Fig. 1.7 Worldwide Projections of Alzheimer's Prevalence [76]**.**

The hallmarks of AD include senile amyloid plaques, cerebral amyloid angiopathy, neurofibrillary tangle, glial responses, and synaptic function loss [77]. Despite having a variety of characteristic neuropathological symptoms, timely and accurate diagnosis of AD still remains challenging. First, to distinguish early stage AD from dementia is difficult as neuropathological changes of AD start to develop 10-15 years before the first clear sign of clinical impairments. Dementia is usually the last stage of AD, and there lacks a biomarker for AD and effective imaging approaches, as a result, most patients are deep into the late

stage of AD when the diagnosis is made, posing an even more challenging situation for treatment and intervention. Misdiagnosis at early stages could also happen, leading to waste of resource and ineffective treatments [78, 79]. Second, the classical AD diagnoses are made thorough neuropsychological evaluation, patient interview, blood-sample analysis, and advanced imaging. The use of amyloid and tau analysis is a useful method because it provides information on specific protein changes in the brain; however, there is large variation between testing facilities, so the threshold of pathological levels varies even using the same methods. The major limitation is that, as mentioned, there are no clear-cut biomarkers [80]. Advanced methods like PET-amyloid camera are not available in every clinical setting, limiting the accuracy of diagnosis. Outside of universities and neurological clinics, diagnostic methods are simpler and even limited, thus misdiagnoses are more frequent. Furthermore, the knowledge of neuropathological processes in AD and normal aging and how to distinguish between them is not entirely understood [78].

One of the reasons that there is no effective cure or treatment for AD is a lack of consensus on what really causes AD. There are still many unproven or undiscovered underlying disease mechanisms. In this thesis, we will focus on one of the most popular hypotheses, the amyloid hypothesis.

1.3 Alzheimer's Disease Pathophysiology

1.3.1 Amyloid Hypothesis

One of the most popular hypotheses of cause of AD centers on the amyloid β fibrils and plaques, which can be found in the patients' brain [81, 82]. They are composed of a major peptide, amyloid-β.

1.3.1.1 Amyloid-β

Aβ is a peptide that contains 39-43 amino acids derived from cleavage of amyloid precursor protein (APP), a transmembrane protein expressed at high levels in brain, by β- and γ-secretase [83]. The exact function of APP is still widely investigated, although it has been implicated as a regulator of synapse formation, antimicrobial activity, and iron exports [83–87]. Depending on the proteolytic site, these secretase enzymes produce two types of Aβ commonly known as Aβ40 and Aβ42 with Aβ 1-42 having two extra amino acids at c-terminus (isoleucine and alanine).

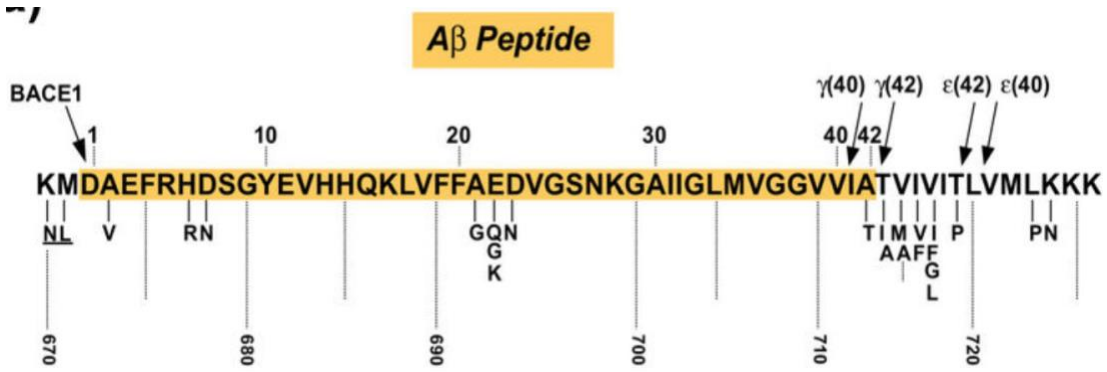

Fig. 1.8 APP and Aβ Sequence Map [88]**.**

Hot debates have been going on for decades whether Aβ42 or Aβ40 contributes more to fibril formation. Although Aβ40is present at 5- to 10-fold higher concentrations than Aβ42 and is overrepresented in mature fibrils and plaques, one cannot conclude simply based on the level of abundancy. Previous experiment injecting freshly solubilized Aβ peptides into rat brains showed that Aβ40 but not Aβ42 consistently forms amyloid fibrils in brain [89, 90], while Aβ42 forms amyloid fibrils spontaneously via incubation in vitro by direct visualization using immunostaining, indicating the molecular events

underlying the fibrillogenesis of Aβ in the AD brain [90, 91]. The findings in such experiments, however, do not contradict the fact that Aβ42 dominates in early diffuse plaques while Aβ40 dominates in core plaques with many amyloid fibrils [90, 91]. As a matter of fact, the amyloid hypothesis cascade starts with the increased ratio of Aβ42 to Aβ40 in the human system [92]. Logically speaking, an increasing level of Aβ and Aβ42 to Aβ40 ratio and initial deposition of Aβ42 are necessary to initiate pathological processes but not sufficient to develop mature plaques without the facilitation by Aβ40 [90–92].

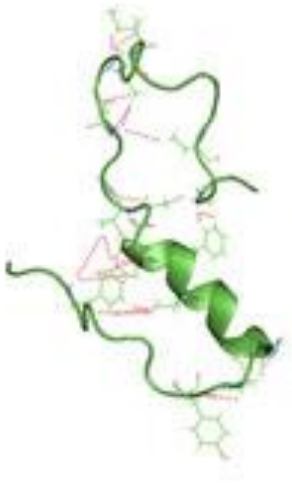

Fig. 1.9 Aβ 2lfm Structure Representation [93]**.**

The amyloid hypothesis is constantly under scrutiny mostly because the therapeutics designed for targeting amyloid plaques do not seem to ameliorate symptoms of AD or show significant cognitive improvement in patients [94]. Previous studies have shown that, in the presence of amyloid depositions, degeneration of nerve cells and neuronal loss were not observed, nor was there impairment of cognitive functions [95]. Recent developments in amyloid imaging enabled visualization of amyloid accumulation

in the patients' brains. It was found that there are healthy patients with amyloid plaques as well as AD patients without them [96, 97]. Some conclude that the amyloid hypothesis is not causative of AD. While it is still premature to draw conclusions even with overwhelming amount of evidence that amyloid might be the cause of AD, it certainly provides more depth for this hypothesis.

1.3.1.2 Soluble Oligomers and Mature Fibrils

Earlier studies assume that large plaques were responsible for neuron damages and disease pathogenesis [98]. Experiments have shown that in cultured neurons, Aβ fibrils increase action potential frequency and lead to membrane depolarization [99]. More specific experiments conducted on rats revealed that direct injection of Aβ fibrils into the hippocampus impairs synaptic transmission and plasticity and causes memory deficits [100]. However, more and more evidence has emerged to indicate that soluble Aβ oligomers may be more toxic than fibrils and may directly induce AD-related pathological events [101–103]. Infusion of oligomeric Aβ into the left ventricles of rat brains showed impairment of learning and memory functions [104]. Several groups proposed different mechanisms of oligomer toxicity in terms of disrupting neuron membrane receptors therefore compromising neurological functions [105, 106]. It has even been suggested that fibril formation might be a protection mechanism of the human body by acting as insoluble secretion of toxic oligomers. This is not surprising, however, as one can explain the rationales simply by common structural sense: oligomers are smaller in size and readily soluble therefore they can easily diffuse in cells to affect the cytoplasm and extracellular space, while fibrils are insoluble and stable [98, 107, 108].

Despite the recent interest in neurotoxic oligomers [92, 102, 103], the correlation of Aβ fibrils and plaques to AD is still actively scrutinized [81, 109–116], especially the fibril structures and fibrillization mechanisms [117, 118]. Aβ forms a variety of stable and structurally disparate amyloid fibrils both in vivo and in vitro [81, 109, 119]. Distinct fibril structures have been linked to divergent clinical outcomes [109]. Emerging evidence suggests that fibrils of Aβ polymorphs that form in the presence of lipid membranes, which are abundant in vivo, may be highly neurotoxic [120, 121]. Furthermore, in early-onset familial forms of AD, especially those associated with the Arctic and Iowa variants of Aβ, it is generally accepted that extensive fibrillization of mutant Aβ is the primary cause of cerebral amyloid angiopathy [122–124]. In addition, even though the structures of the toxic oligomers may be distinct from those of mature fibrils, understanding the molecular-level processes of fibril growth may be informative of oligomer behaviors and must play a part in the systems biology [109, 119, 125].

It is believed that Aβ fibril formation is controlled by stochastic nucleation. Hortschansky *et al*. reported repeatable sigmoid behavior of ThT fluorescence signal when monitoring fibril growth under various conditions [126]. The sigmoid curve represents three stages. The first stage is the nucleation stage in which Aβ monomers cluster to form nuclei. Because these nuclei yet to have abundant ordered β-sheet structure, the signal does not grow significantly. When the nuclei reach a critical nucleus size, the fibrils start to grow by adding Aβ monomers to the end to fibril strands, which corresponds to the growth stage of the sigmoid curve. When Aβ monomers are depleted in the solution, the saturation stage of the curve is reached. For each experiment they were able to extract a lag and a growth phase, which was fitted by exponential function. It was found that the lag time decreases

and the rate constant increases with increasing concentrations of Aβ [126]. Their data showed that such random nucleation process could lead to heterogeneity or to aggregates of different structures, for example, fibrils, protofibrils and oligomers as confirmed by other groups [127].

One of the most widely accepted fibril growth mode is the Chen-Ferrone-Wetzel model. According to this model, amyloid fibrils grow by adding monomers to the two ends of fibril strands and the growth follows a first order kinetic behavior [128]. At first when there is no fibril present, largely unstructured Aβ monomers cluster to form nucleus. When it reaches a critical nucleus, it then grows to fibrils by the model described above. The growth also follows a two-step dock-and-lock mechanism in which the monomer first docks with the fibrils then the monomer/fibril complex undergoes conformational change to let the monomer adopt the structure that is commensurate with the fibrils [129].

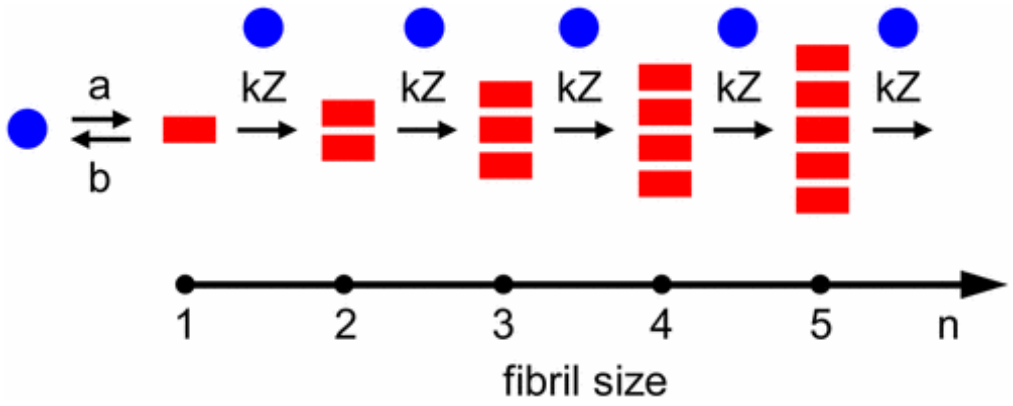

Fig. 1.10 Basic Model of Monomer Addition to Fibrils [128]**.**

But the reality is that, the assembly of Aβ peptides into fibrils is probably more complex than the simple models proposed [129]. After the peptides diffuse toward each other, they establish contacts between their amino acid residues and realign these contacts

to find conformations that minimize the free energy of the emerging structure [125]. Not only is there nucleation and growth by monomer "lock-and-dock", but also, after further growth, the longer fibrils may fracture, doubling the number of growing tips and releasing peptide oligomers, which in turn boost nucleation [130, 131]. The fibrils also can branch by secondary nucleation. Both processes autocatalytically accelerate fibrillization [132]. This complex series of events can lead to explosive growth of both oligomers and fibrils and encourage the spread of the aggregates and disease in patients' brains. Signs of frustration during monomer incorporation into the fibril were also observed in simulation studies [125], pointing to an elaborate mechanism.

Common experimental methods for aggregation studies focus on indirect spectroscopic characterizations and rough quantitative microscopic characterizations, which bear certain limitations [110, 133, 134]. The entangled fibrillization processes are typically studied in bulk assays [132, 135], which often employ agents such as Thioflavin T that fluoresce at a specific wavelength when bound to an amyloid structure [136]. The fluorescence signal is assumed to scale with the total fibril mass, which increases due to fibril nucleation, growth, fragmentation, and branching occurring in parallel [137]. The presence of a fluorescent tag that binds to the fibrils, however, may modify the kinetics. In bulk assays, the contributions of each of the constituent processes to the evolution of the signals cannot be directly evaluated but must be assessed from fits to models in which each step is expected to obey simple kinetic laws [132, 135]. Usually, fibril growth has been approximated as a simple bimolecular reaction between the fibril tips and solute peptides [110, 135]. Recent studies have employed AFM and fluorescence microscopy to monitor the growth of individual amyloid fibrils of diverse proteins and peptides [133, 134, 137–

144]. In contrast with the steady bimolecular reaction at the fibril tips, usually assumed in the models of bulk fibrillization, the growth trajectories sometimes incorporate periods of complete stagnation and the two ends of a fibril often grow at distinct rates. Asymmetric, unsteady, stagnant, and non-bimolecular fibril growth modes have not been considered in the current models. As a consequence, the molecular mechanisms of fibril growth have remained elusive, severely restraining the search for ways to suppress amyloid fibrillization.

1.3.1.3 Amyloid Interactions with Lipid Bilayers

Aβ fibrils have been studied extensively in vitro [110, 138, 141, 145]. To truly understand Aβ fibrillization, it is important to consider the environment that Aβ is constantly in. There have been a lot of studies focused on the modulatory effects that are relevant to Aβ's true biological context, trying to further the understanding of mechanism of Aβ. Among them, one particularly important factor is the lipid bilayer [146–148]. In the human brain, Aβ is inevitably in close contact with lipid membrane rich environments: Aβ peptide is derived from APP [83], which is a transmembrane protein itself; Aβ can form aggregated entities inside organelles [149]. Despite emerging interest, many questions stay unanswered. For example, it was found that amyloid fibrils formed in the presence of lipid membranes may be highly neurotoxic [120, 121]; however, the mechanism responsible for neurotoxicity is not well understood. Aβ concentrations in vivo was found to be ~5 nM [150, 151], whereas fibrillization in vitro requires concentrations level at μM levels, which could be due to an increased effective concentration resulted from decreased diffusion by lipids [152].

Lipid bilayers come in different charges, different phases, and different curvatures, etc. It has been found that lipid with different charges interact with Aβ in different fashions

[153, 154]; reduced lipid bilayer thickness facilitates oligomers formation but inhibits mature fibril growth, which could in turn disrupt bilayer integrity [155]; lipid bilayers with smaller curvature has a higher binding affinity to Aβ [156]. In addition, lipid rafts, cholesterol level, associated salt and pH have been shown to affect fibrilization [157–159].

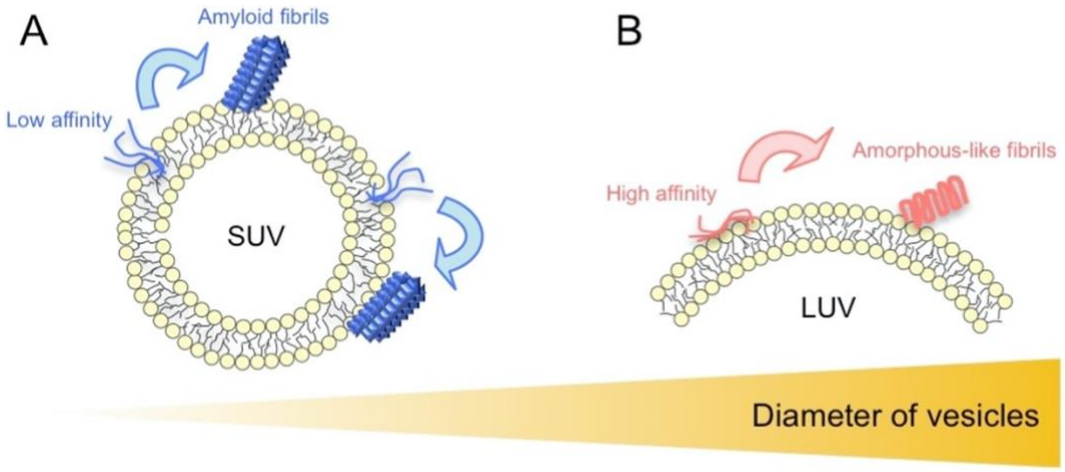

Fig. 1.11 Schematic Models of Amyloid Nucleation and Amorphous Aggregation on the Surface of Liposome Membranes [156**].**

The current literatures is not at all without its disagreements. Hot debates have been going on about whether lipid bilayers interact with Aβ monomers directly. Some state that lipid bilayers with different curvatures bind to monomeric Aβ through different models, while some state that they do not interact at all, rather, only interacting at a higher order oligomers states [160–162]. Besides this, the community has not agreed on whether the lipid bilayers act as a stimulant to fibrillization, or as an inhibitor [161, 163].

1.3.2 Genetic Hypothesis

Approximately 95% of Alzheimer's cases occur in people over the age of 65, defined as the sporadic AD as opposed to the early-onset AD, accounting for 5% of all cases, of which 20% is purely genetic, categorized as the familial Alzheimer's disease (FAD) [88].

Although the reason behind the onset of AD is still unclear, it is believed that genetic factors play a crucial role. There are two major parts to the genetic theory, the genetic risk factor, and mutations. The strongest genetic risk factor is APOEε4, which is one of three major alleles of apolipoprotein E (APOE) [145]. APOE plays a major role in lipid-binding proteins, transporting lipids, fat-soluble vitamins, and cholesterol into the lymph system and then into blood and the APOEε4 allele disrupts these functions. 40%-80% of Alzheimer's patients possess at least one copy of the APOEε4 allele and this allele increases the risk of AD by three times in heterozygotes and by 15 times in homozygotes [146]. The other theory is that APOE enhances proteolytic clearance of Aβ peptides but the APOEε4 allele is not as effective as others, resulting in an increased vulnerability to AD [147]. Despite overwhelming evidence suggesting APOEε4 correlates with AD, studies have shown that people with APOEε4 alleles, high cholesterol levels and high blood pressure show a further increase in the risk of developing AD by three times. It may be important to keep cholesterol levels low in order to reduce AD risk, even with APOEε4 alleles. Nigerian people have the highest observed frequency of APOEε4 alleles, yet AD is rare among their populations. This may be due to their low cholesterol levels in the general population [148, 149].

The 1% FAD among total AD cases can be attributed by mutations based on a number of pieces of evidence. The APP gene is located on chromosome 21, which had been linked to AD by multiple genetic studies and by the observation that Downs's Syndrome patients develop dementia to different degrees accompanied with similar neuropathology [88, 92]. One of the major mutations causative of familial Alzheimer's disease (FAD) aggregates around the proteolytic site of β- (BACE1) and γ-secretase, resulting in more Aβ being released into extracellular environment. For example, the KM670/671NL Swedish mutation, upstream of Aβ position 1increases total Aβ secretion [150]. It increases the affinity between APP sequence and BACE1 and enables BACE1 process the APP sequence early in the Golgi network compartment as opposed to cell surface and early endosomes in the case of wile type (WT) sequence, enhancing Aβ productions [151–153]. The other mutations cluster around the region within the Aβ sequence, changing the charge distribution and the structures of Aβ, promoting fibril formation [88]. Specifically, the mutations causative of cerebral amyloid angiopathy (CAA), characterized by extensive amyloid buildup around vasculatures, cluster around the central region of APP sequence [154, 155]. Data have identified a turn in the V24-K28 region of Aβ, which could be critical for folding and is in part stabilized by sites in the central region of APP sequence. These mutations destabilize the turn and promotes fibrils formation. In addition, these mutated peptides also appear to be more resistant to degrading enzymes [88, 155, 156]. We should not ignore the mutations in secretase, either. The presenilin (PSEN) proteins form the catalytic core of γ-secretase, the protease that catalyzes the last step in secreting Aβ peptide. In some cases, mutated PSEN overexpression significantly increases the level of Aβ in the system, while there were cases in which

reduces the level of Aβ40 and in turn increases the ratio of Aβ42 to Aβ40, a step of AD cascade as described in Chapter 1.3.1.1.

1.3.2.1 Dutch Variant

The Dutch variant Aβ has a single mutation at site 22. The glutamic acid originally at position 22 is replaced by glutamine, changing it from an acidic side group to a polar neutral side group. Dutch mutation was identified as being causative of hereditary cerebral hemorrhage with amyloidosis Dutch type (HCHWA-D) [157]. The neuropathy of HCHWA-D is distinct from that of AD, being characterized by severe amyloid deposition around the vasculature, termed as cerebral amyloid angiopathy (CAA). Patients with severe cases develop cerebral hemorrhages and stroke in addition to parenchymal plaques [88]. It is still unclear why the Dutch variant causes early-onset AD; however, existing studies should at least provide some perspectives. Watson *et al.* proposed that Dutch variant has a propensity for formation of β-sheet structures in solution. They found that E22Q mutant peptides assume conformations with higher affinity to heparin, which favors interactions between β-sheet structures, compared to WT peptide. The affinity between E22Q peptide and heparin is similar to that between preformed Ac fibrils and heparin [158]. It was also found that Dutch mutant deposit at a rate ~200% faster than the WT peptide because the Dutch mutant peptide forms oligomers and fibrils more readily owing to the fact that it converts from random coils to β-sheet structures one order of magnitude faster than the WT does [159, 160]. Simulation study conducted by Baumketner *et al.* has shown that E22Q does not alter the β turn fold in position 21-30 but slightly weakens the position 22-28 salt-bridge contacts. What is more significant is that it weakens the interactions between position 22-28 and the central hydrophobic core at position 17-21. A direct manifestation

of this is the complete disappearance of hydrophobic contact in region 19-24, which in turn increases β-sheet content in the central hydrophobic core [155, 161].

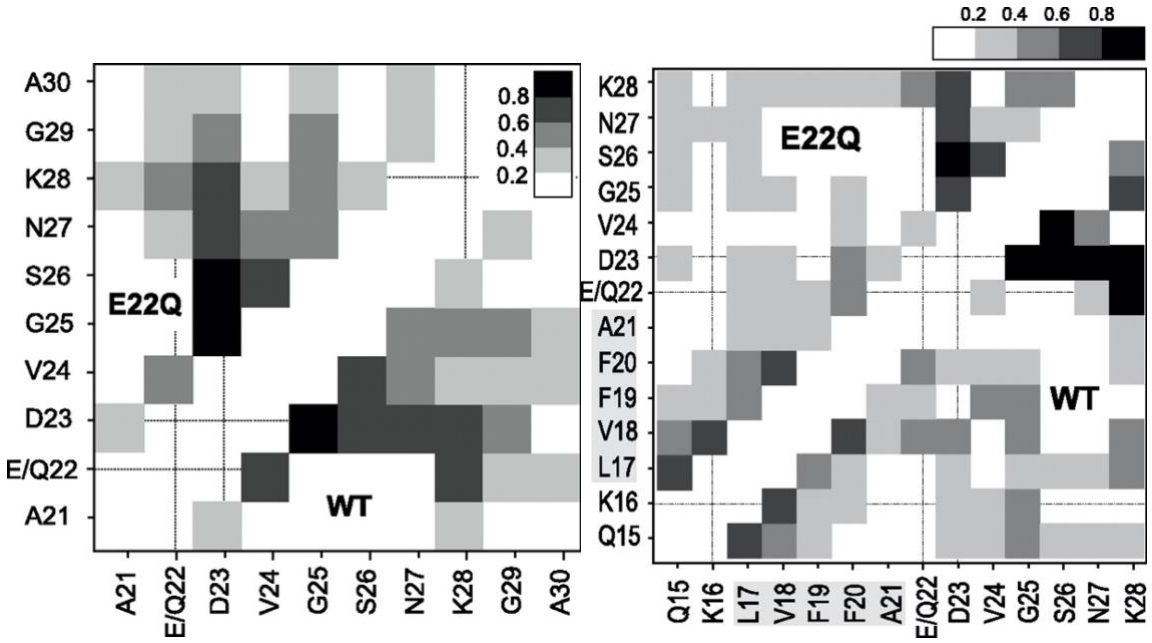

Fig. 1.12 Probability Map of Interresidue Contacts Computed in the Present Simulations for Aβ15–28WT (lower right triangle) and Aβ15–28E22Q (upper left triangle) [155]**.**

Dissociation simulations have shown that positions 17-20 on a peptide monomer are the last to break from fibrils, consistent with the fact that the central hydrophobic core serves as the docking site for Aβ monomer incorporation to fibrils as the hydrophobic core is exposed to the solvent. Once the monomer docks to the fibril via the 17-20 region, this region refolds into a β-like structure following by a transition to β-sheet structure at position 14-16 and 30-36, and the free energy cost of these processes is reduced in Dutch variant [155, 162].

We explored Dutch variant Aβ40 experimentally in Chapter 4.

1.3.3 Cholinergic Hypothesis

The cholinergic hypothesis is the oldest theory regarding AD, first proposed in 1976 [163]. It was believed that reduced production of acetylcholine, a crucial neurotransmitter that functions as chemical messengers to transmit signals from neurons across the synapse to a target cell, initiates AD. This premise has since been adopted as the basis for therapeutics development.

For more than 30 years, studies of AD patients' brains have consistently found signs of abnormalities in the cholinergic pathways, through which thalamus plays roles in awareness, attention, and memory, that correlate well with cognitive levels. As a result, the dysfunction of cholinergic pathways was attributed to cognitive decline associated with AD [164, 165]. At the early stage of AD research, this hypothesis was widely accepted because of strong support from animal and human experiments showing cholinergic antagonists impairing memory related functions [166]. Based on this evidence, therapeutic approaches addressing cognitive loss associated with AD mainly have focused on a cholinergic replacement strategy, among which cholinergic ligands to improve cholinergic functions and acetylcholinesterase inhibitors to reduce acetylcholine clearance have been the most popular [167].

It was not long before the community started to challenge this hypothesis. Therapeutics based on restoring cholinergic function, though sometimes beneficial, have not proved to be a cure. In all cases, they treat the symptoms associated with AD temporarily but have neither halted nor reversed AD itself [168]. Investigations into early stages of AD originally aiming to find diagnostic measures also challenged the validity of

the cholinergic hypothesis. A number of studies in which the brains of patients diagnosed with mild cholinergic impairment or early/mild AD reported that the activity of acetylcholine related enzymes was not reduced, and in some cases was actually upregulated [169, 170]. These studies eventually led to several suggestions: it is unlikely that a cholinergic marker could be an early indicator of AD, cholinergic deficit could not be identified prior to patients becoming symptomatic, and cholinergic dysfunction may not be causative to AD [161]. Nevertheless, the cholinergic hypothesis helped develop a new strategy to treat cognitive decline in AD patients and is of great significance to the battle with AD.

1.3.4 Tau Hypothesis

The tau hypothesis was developed based on the discovery of extensive neurofibrillary tangles inside nerve cell bodies [171]. Tau proteins are a group of six high soluble proteins that primarily maintain the stability of microtubules and are abundant in neurons. The significance of tau proteins is that they play parts in keeping the cytoskeleton and structures stable in nerve cells.

The tau protein hypothesis starts with hyperphosphorylation. Hyperphosphorylated tau proteins then begin to pair with other tau molecules as paired helical filaments, which later develop into neurofibrillary tangles [171]. These tangles would disintegrate microtubules, destroy the cytoskeletons of neurons, and eventually collapse neuron's transport system [191]. What's more striking is that these tau aggregates may also propagate in the fashion of prion and induce normal tau proteins to form neurofibrillary tangles [192]. In addition, mutant forms of tau protein can cause enhanced neurotoxicity [193].

Therapeutics developed on the basis of the tau hypothesis fall into several different categories: tau assembly inhibitors, tau kinase inhibitor and microtubule stabilizers. It is not hard to understand as the main goal is to prevent hyperphosphorylation and aggregation of tau and improve microtubule stability [194]. The effectiveness of tau-related therapeutics remains to be further studied [195].

There have been researches into the cross-over between the tau and amyloid hypothesis. As described in Chapter 1.3.2, people with APOEε4 alleles are more likely to develop AD partly because APOEε4 is inferior to other alleles in amyloid clearance. It turns out that APOEε4 could also enhance tau hyperphosphorylation [196]. GSK3 is another factor that regulates both tau and APP. It affects enzymatic processing of APP, which leads to an increased level of Aβ in the system and stimulates tau hyperphosphorylation at the same time [197, 198]. In addition, APP and tau act together to mediate synaptic toxicity and dysfunction of either party could disrupt iron homeostasis. Specifically, APP regulates efflux of ferrous ions with the help of tau transporting APP to cell surface and if tau develops into neurofibrillary tangles, APP tracking to cell surface will be significantly reduced, leading to abnormal iron accumulation [199–201].

Chapter 2: Steady, Symmetric, and Reversible Growth and Dissolution of Individual Amyloid-β Fibrils

2.1 Background

The kinetics of amyloid assembly have typically been investigated in bulk assays [136, 173, 174], in which the recorded signal reflects a convolution of molecularly distinct events: nucleation, growth, fragmentation, and fibril surface-catalyzed nucleation. It is hard to untangle these processes [137]. Recently, valuable insights have come from studies focused on the growth of individual amyloid fibrils, observed by AFM and fluorescence microscopy [110, 133, 134, 137–142]. These studies have raised several questions concerning the mechanisms of Aβ40 fibril growth. Is fibril growth steady or do periods of stagnation alternate with bursts of growth? Do parallel adjacent protofilaments cooperate to grow faster or slower than isolated ones? Do opposing fibril ends grow at similar rates in a symmetrical fashion? Do fibrils grow by incorporation of monomers or of dimers and higher oligomers? Is the sequence of molecular-level events leading to incorporation in a fibril exactly reversed during dissolution? Is the incorporation of Aβ monomers in a fibril delayed by a kinetic barrier or is its rate limited only by monomer diffusion? Here we monitor the growth of individual Aβ40 fibrils by time-resolved in situ AFM to address these questions [204].

2.2 Materials and Methods

Solution Preparation. Deionized (DI) water was produced by a reverse osmosis ion exchange system (Rios-8 Proguard 2, MilliQ Q-guard, MilliporeSigma). LB-ampicillin growing media was prepared by dissolving LB (Sigma Aldrich) in DI water and adding 100 mg mL^{-1} ampicillin stock solution, prepared by dissolving ampicillin sodium salt

(Fisher Scientific) in DI water, to a final concentration of 20 g L^{-1} and 100 μg mL^{-1}. IPTG (isopropyl β-D-1-thiogalactopyranoside, Sigma Aldrich) stock solution was prepared by dissolving IPTG in DI water to a concentration of 100 mM. Sonication buffer was prepared by dissolving Tris and EDTA (ethylenediaminetetraacetic acid, Sigma Aldrich) in DI water to a concentration of 10 mM and 1 mM, respectively. pH was adjusted to 8.0 using HCl (Sigma Aldrich). Binding buffer was prepared by dissolving urea (Sigma Aldrich) in the sonication buffer to a concentration of 8 M. pH was adjusted to 8.0 using HCl. Elution buffer was prepared by dissolving NaCl (Sigma Aldrich) in the binding buffer to desired concentrations. pH was adjusted to 8.0 using HCl. Size-exclusion chromatography (SEC) buffer was prepared by dissolving ammonium acetate (Sigma Aldrich) in DI water to a concentration of 50 mM. pH was adjusted to 8.5 using NaOH (Sigma Aldrich). Thioflavin T (ThT, Sigma Aldrich) solution was prepared by dissolving ThT in DI water and the concentration was determined by measuring absorbance at 416 nm using a DU800 Spectrophotometer (Beckman Coulter) with $\varepsilon_{280,EtOH} = 26.6$ mM^{-1} cm^{-1} . Fibril incubation buffer was prepared by dissolving sodium phosphate monohydrate (Mallinckrodt) in DI water to a concentration of 40 mM. pH was adjusted to 7.4 using NaOH.

Aβ40 Expression and Purification. pET-Sac-Abeta(M1-40) plasmid inserted in E. coli DH5alpha (Addgene) was extracted using a QIAprep Spin Miniprep Kit (QIAGEN) and kept in a glycerol stock for long term storage. To express Aβ40, the plasmid was transformed into E. coli BL21(DE3) (strain provided by Dr. Patrick Cirino, University of Houston) by electroporation and a single colony of the transformed E. coli from an overnight LB agar plate was inoculated into 10 mL of LB-ampicillin growing media. The culture was incubated in a MaxQ 5000 shaker (Barnstead Lab-Line) for four hours before

diluting 100-fold using the same media. When the optical density of the culture at 600 nm reached 0.5 – 0.6 (measured using a NOVOstar Plate Reader, BMG Labetch), IPTG stock solution was added to the culture to a concentration of 100 μM. The culture was subsequently allowed to grow for four hours in the shaker before cells were pelleted. All incubation procedures were performed at 37 ºC controlled by the shaker.

The cells were re-suspended in 20 mL of ice-cold sonication buffer, sonicated using a Qsonica Misonix Sonicator XL-2000 (10 W output) on ice for two minutes with 30 seconds interval and centrifuged using an Avanti J-E Ultra Centrifuge (Beckman Coulter) for 12 minutes at 4 ºC and 18000 × g. The supernatant was discarded. After two rounds, the cells were resuspended in ice-cold binding buffer and subjected to the same sonication and centrifugation procedure for one round. The resulted supernatant was collected and filtered using 0.45 μm PES syringe filters (polyethersulfone membrane, VWR International).

The supernatant collected after three rounds of sonication was diluted with ice-cold binding buffer to a final volume of 40 mL. The solution was then mixed with 10 mL of pre-chilled Q Sepharose Fast Flow resin (GE Healthcare Lifescience) equilibrated in ice-cold sonication buffer. The mixture was allowed to fully mix on a STD Vortex Mixer (Fisher Scientific) for 15 minutes, then centrifuged for 15 minutes at 4 ºC and 2500 × g using a Sorvall Legend X1R Centrifuge (Thermo Fisher), and the supernatant was discarded. The resin was then subsequently eluted using 10 mL of elution buffer with 50 mM, 75 mM, 100 mM, and 500 Mm NaCl, respectively, following the same procedures of mixing and centrifugation. All procedures were performed in refrigerator, on ice, or in the

temperature-controlled centrifuge to keep the samples cold. The fractions with most Aβ40 (50 mM and 75 mM NaCl eluates) were collected for further purification.

The two fractions collected were concentrated using a 30kDa molecular weight cut-off (MWCO) Ultra Centrifugal Filtration Unit (Amicon) and the filtrate was subsequently filtered again using a unit with 3kDa MWCO. Retentates from these two steps were adjusted to 500 μL and sent through SEC. Monomeric Aβ40 was isolated by chromatographing the retentates on Superdex 75 16/20 XK column (GE Healthcare Lifescience) utilizing ÄKTA Pure System (GE Healthcare Lifescience), eluting at 0.7 mL min^{-1} with the SEC buffer. Fractions of 0.7 mL containing the desired peptides were collected based on the absorbance peak at 280 nm from the chromatogram, concentrated to 100-150 μM based on productivity, using NanoDrop Lite (Thermo Scientific) by absorbance at 280 nm with ε_{280} = 1490 M^{-1} cm^{-1}, filtered using the 0.45 μm PES syringe filters and stored in -80 ºC.

The identity of the peptides was confirmed using western blot following the BIO-RAD western blot protocol. Primary amyloid beta polyclonal rabbit antibody (Fisher Scientific) was used to bind with Aβ40 and goat anti-rabbit IgG secondary antibody HRP (Fisher Scientific) was used to detect binding of primary antibody. The 1-step Ultra TMB-Blotting HRP Substrate solution (Fisher Scientific) was used to check binding of secondary antibody.

LC-MS Analysis. Liquid chromatography- mass spectroscopy/mass spectroscopy (LC-MS/MS) analysis was conducted using a Shimadzu Prominence LC-20AD XR UPLC system interfaced to a Shimadzu Ion Trap – Time of Flight (IT-ToF) Mass Spectrometer (MS) through an Electrospray Ionization (ESI) source. Separations were achieved using a

1.0 mm ID x 150 mm, 2.7 micron particle size Ascentis Express Peptide ES-C18 column. The column was operated at a flow rate of 0.15 mL min^{-1} with mobile phase A: 0.1% (v/v) formic acid in water and mobile phase B: 0.1% (v/v) formic acid in acetonitrile. The LC gradient for the analytical separation was operated as follows; 5% B (IC), 5% B to 30%B (0.0 min to 12.5 min), 30%B to 50%B (12.5 min to 14.5 min), and 50%B to 95%B (14.5 min to 16.0 min). MS spectra were acquired over the range of m/z 300 to m/z 1200. The open source mass spectrometry tool mMASS was used to assist with data analysis.

Fibril Formation. The kinetics of fibril formation was monitored using the ThT binding assay. The stock Aβ40 was buffer exchanged and diluted to 100 μM in the fibril incubation buffer. To monitor fibril formation, ThT was added to an Aβ40 solution to a final concentration of 100 μM. The ThT fluorescence was monitored at 37 °C with mixing. Measurements were taken every 15 minutes with excitation and emission at 442 nm and 488 nm, respectively, using a SpectraMax Gemini EM Microplate Reader (Molecular Devices). The sigmoid curve representing the collected data points usually saturated after ~10 hrs.

Based on the ThT assay, fibrils were allowed to grow at 37 °C and 300 rpm on a table Inkubator 1000 (Heidolph) for 24 hours (without ThT solution). After 12 hours, visible precipitate of Aβ40 appeared. These fibrils (the first generation) were used as seeds for second-generation fibrils. For this, the stock Aβ40 was buffer exchanged and diluted to 50 μM in the fibril incubation buffer with 10% v/v of the first-generation fibril solution, incubated using the same condition as the first-generation fibril growth.

Time-resolved in situ AFM imaging. We used a multimode atomic force microscope (Nanoscope IV and VIII, Digital Instruments) for all AFM experiments. AFM images were

collected in more gentle tapping mode using Olympus TR800PSA probes (Silicon nitride probe, Cr/Au coated 5/30, 0.15 N/m spring constant) and Bruker SNL-10C probes (Silicon nitride probe, 0.24 N/m spring constant) with tapping frequency 37.2 kHz and 56 kHz. Image sizes ranged from 1 μm × 1 μm to 4 μm × 4 μm. Scan rates were between 1 and 2.52 s^{-1}. Height, amplitude, and phase imaging modes were employed. The captured images contained 256 scan lines at angles depending on the orientation of the monitored fibril. We processed height, amplitude, and phase images by flattening or plane fitting. No low pass or median filters were applied to any AFM images. The temperature in the fluid cell reached equilibrium of 27.0 ± 0.1°C within 15 minutes, which was higher than room temperature (ca. 22°C) due to heating by the AFM scanner and laser. To prepare samples for AFM imaging and growth rate measurements, aliquots of 2 μL of the second-generation fibril solution was added to the fibril incubation buffer. The diluted fibril solution was sonicated for two minutes of with a 15-second interval on ice and was equilibrated at 27 ^{o}C for at least 15 minutes. The stock Aβ40 was then added to the fibril solution and adjusted to the desired concentrations and set to a final volume of 1 mL. To image fibril growth under AFM, ~500 μL of the fibril solution was injected into a liquid cell over a freshly cut mica surface (Ted Pella Inc.). An O-ring was inserted firmly into the liquid cell to avoid leakage.

ANOVA Test. One-way analysis of variance (one-way ANOVA) was employed to test if the growth rates measured with different tip velocities under the same condition are statistically distinguishable. The one-way ANOVA compares the variance between each group to the variance within each group. The F-value, representing the ratio of these two variances, is 1.55, smaller than the critical F-value 3.15, coming from 3 groups of 65

individual measurements with a 95% confidence interval. The p-value, 0.22, is greater than the α-value 0.05. Both F-value and p-values fail to reject the null hypothesis of ANOVA, which states that the mean values are the same for all independent groups.

2.3 Determination of Fibril Growth Rates

We generate fibrils in a stirred solution and deposit them on freshly cleaved mica surfaces mounted on the AFM scanner [205]. We fill the AFM fluid cell with an Aβ40 solution of known concentration in 40 mM phosphate buffer at pH = 7.4. The solution is replenished periodically to maintain constant peptide concentration. We employ the tapping mode of AFM, whereby the substrate, on which the fibrils are deposited, is scanned with an oscillating tip (Fig. 2.1A). The amplitude, the resonance frequency, and the phase shift of the tip vibrations are modulated by the interaction with the fibril and the response is used to deduce its topography [131]. AFM imaging of the mica surface in this solution reveals fibrils firmly attached to the substrate [206]. In time, both ends of the fibrils grow (Fig. 2.1B–E). We select immobile markers on the substrate that are visible in several consecutive images and use them as reference points to measure the displacement of each fibril end along the fibril axis (Fig. 2.1B–E). We evaluate the fibril growth rate as the slope of the time correlation of the fibril end displacement (Fig. 2.1F). As defined, the growth rate characterizes individual fibrils and can be determined uniquely for each of the two fibril ends.

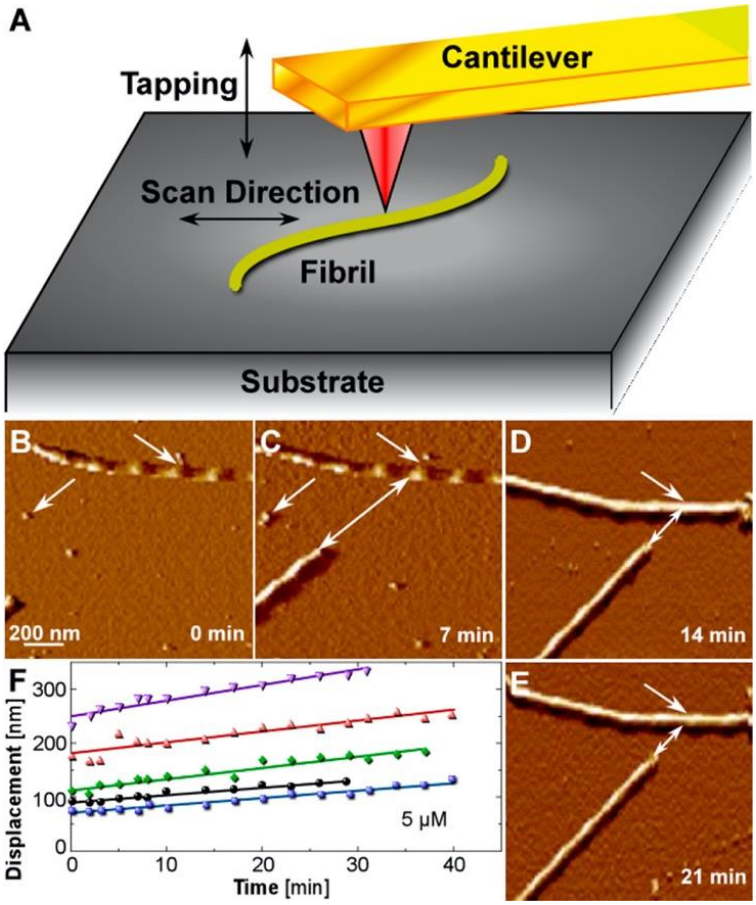

Fig. 2.1 Determination of Growth Rates for Individual Aβ40 Fibrils.

Figure 2.1 **(A).** Schematic of tapping-mode imaging of a fibril deposited on a substrate by an AFM tip. **(B–E).** Time-resolved in situ AFM images showing the growth of an Aβ40 fibril in a 1 μM solution. White arrows indicate immobile reference points. Double-sided arrows indicate the distance between a fibril end and a reference point. Image acquisition times were about 100 s. **(F).** Evolutions of the displacements of five fibril ends and the respective best-fit lines that were used to determine the fibril growth rates at a solution concentration of 5 μM, as indicated in the plot.

The fibril growth rate measurements described above are direct. They do not require fluorescent labeling of the peptide or the presence of fluorophores such as ThT, both of

which could modify the aggregation kinetics and thermodynamics. To address the concern that scanning with the AFM tip might influence fibril growth we examined the impact of the imaging tip and solution shear due to the horizontal motion of the AFM tip in the immediate vicinity of the surface. We found that several changes in scan protocol do not affect the apparent rates of fibril growth. Tip velocities of 1–10 μm s^{-1} would engender a boundary layer around the tip with thickness of the order of a few micrometers in which the shear rates are of the order of 1–10 s^{-1} [207]. Higher solution shear may affect the conformation of unfolding globular proteins [207, 208] and may to a lesser extent impact the conformation of Aβ monomers (in solution, Aβ40 adopts a structure with α-helical and hairpin segments) [113, 125, 180]. The resulting conformational variability may enhance or suppress the fibrillization rates, similar to observations with other protein condensates [210, 211].

Our tests showed, however, that scanning in two perpendicular directions (Fig. 2.2A) produced statistically indistinguishable growth rates (Fig. 2.2B). In a second test, we increased the tip velocity from 2 to 10 μm s^{-1} by varying the image size and scan rate. We analyzed the similarity between the distributions of growth rates obtained with distinct tip velocities (Fig. 2.2C) by one-way analysis of variance (ANOVA), a statistical procedure, which compares the variance between the three groups to the variance within each group of data. The F value, corresponding to the ratio of the two variances, was 1.55, smaller than the critical value of 3.15 for three groups consisting of 65 independent measurements. The p value was 0.22, greater than the significance level of 0.05, certifying that the hypothesis of equality of the three mean growth rates is held. All measurements discussed below were executed with scanning tip velocities between 5 and 10 μm s^{-1}. In a third test, we compared

the fibril growth rates in an area of the substrate that was continuously imaged for 13 min, to those of fibrils outside of the viewing area (Fig. 2.2D–G). The growth rates in both groups were in the range 3–5 pm s^{-1}. As evidence that interaction with the substrate does not modify the growth rates, below we highlight the similarity of the growth rates measured using the present method to those determined from time-dependent bulk growth of fibrils in solution [110].

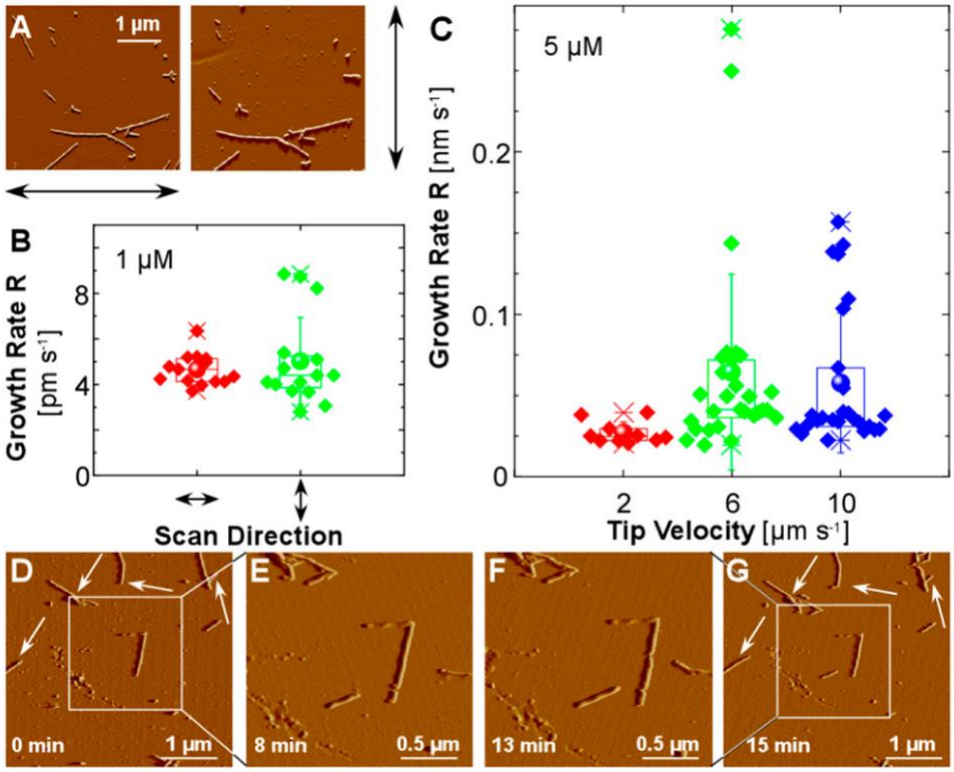

Fig. 2.2 Tests for Imaging Artifacts.

Figure 2.2 **(A).** In situ AFM images showing fibrils growing in 1 µM Aβ40 solution scanned in directions indicated by double-sided arrows. **(B).** Jitter plots of fibril growth rates determined from images collected with the two perpendicular scanning directions

shown in (A). Upper, median, and lower horizontal lines exceed 75, 50, and 25% of the data points, respectively. The times sign (×) indicates fastest and slowest growth rates, spheres mark the average values, and capped vertical bars denote the standard deviations of the data sets. **(C).** Jitter plots of distributions of fibril growth rates at displayed Aβ40 concentration, determined using indicated tip velocities. **(D–G).** Time-resolved in situ AFM images showing the growth of Aβ40 fibrils in a 1 μM solution over 15 min employing embedded scan areas. Tip velocity 5 μm s^{-1}. White box indicates area of zoom-in scans in (E) and (F) after image in (D) was recorded. (G) Image with lower zoom ratio incorporates area scanned in (E) and (F), highlighted in white box. Arrows in (D) and (G) indicate fibrils that grew outside of continuously scanned area observed in (E) and (F). Image acquisition times in (A) and (D)–(G) were about 100 s.

2.4 Fibril Polymorphism, Growth Symmetry, and Growth Rate Variability

Aβ forms several stable distinct polymorph structures both in vivo and in vitro [81, 109, 119, 183]. In most of the studied structures, the constituent monomers fold into a U-contour with sides comprised of β strands [110, 119, 184, 185]. The monomers assemble into a gutter-shaped protofilament with walls formed by β-sheets, in which the constituent β strands align perpendicular to the long protofilament axis [119, 186]. The assembly of two or three parallel protofilaments is classified as a filament and a single fibril often contains several filaments [216]. All elements of this structural hierarchy may attain various morphologies [110, 119, 184]. Whereas Aβ oligomers may contain antiparallel β-strands [125], abundant evidence suggests that the protofilaments found in mature fibrils are built as parallel β-sheets [110, 119]. The two most common structures formed in vitro

consist of either two or three symmetrically arranged protofilaments running parallel to the fibril axis [110, 119, 184]. The threefold symmetric filaments, whose thickness is about 7.0 nm, dominate in quiescent solutions, whereas agitated solutions (like those we use to make our samples) promote a twofold symmetric polymorph (as in Fig. 2.3A), in which the filaments have a roughly rectangular cross-section with dimensions 6 × 5.2 nm^2 [110, 119, 184]. Importantly, the structure of a fibril does not change along its length. Morphological characteristics, such as fibril width, twist period, and mass-per-length, propagate as the fibril grows and transfer from a seed to the newly grown segments [119].

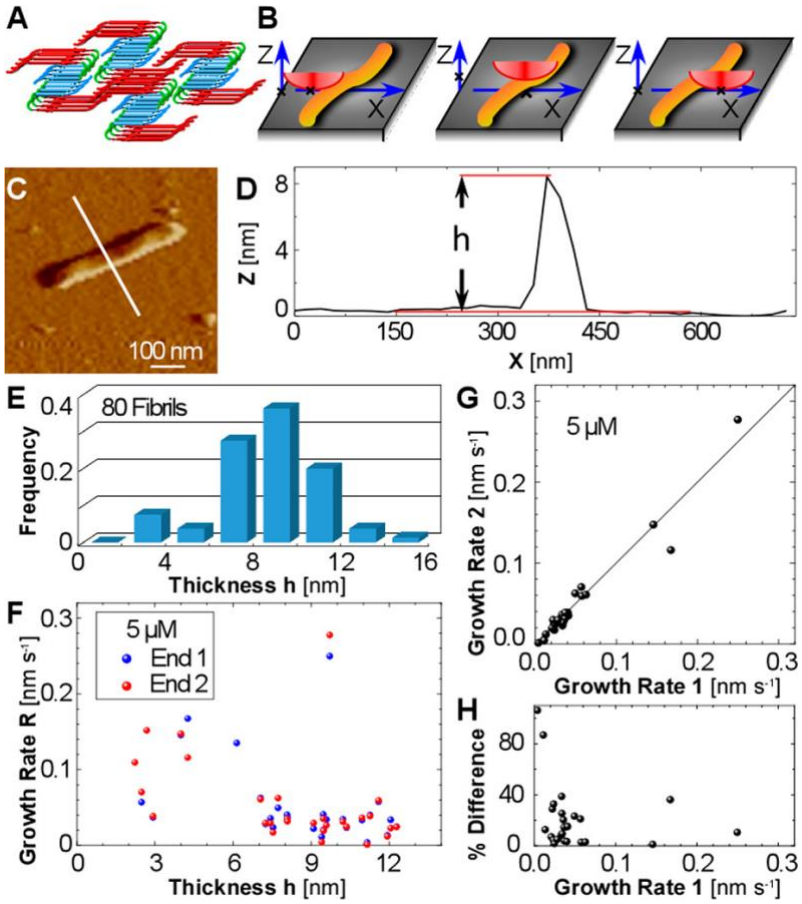

Fig. 2.3 Fibril Thickness and Symmetry of Growth of Two Fibril Ends.

Figure 2.3 **(A).** Schematic of a fibril that consists of four filaments, each composed of two protofilaments related by a twofold axis. Red, green, and blue denote N-terminus, hinge, and C-terminus of the Aβ40 peptide. **(B).** Schematic of the interaction of an AFM tip with a fibril. Here, the x axis extends along the scan direction and the z axis measures separation of tip from substrate. The times sign (×) marks the readouts along the z and x axes when the tip touches the fibril, when the tip is on top of the fibril, and when the tip detaches from the other side of the fibril, respectively. **(C, D).** Illustration of measurement of fibril thickness using AFM. (C) Height mode image of a fibril growing at Aβ40 concentration 1 μM. (D) Height profile along the line in (C) and illustration of thickness h determination. **(E).** Distribution of fibril thicknesses. **(F).** Growth rates of opposing fibril ends plotted as a function of respective fibril thickness. Solution concentration is indicated in the plot. **(G).** Correlation between rates of growth of the two fibrils ends. Three points corresponding to fibrils that only display one end in the AFM field of view have been omitted from this plot. Solution concentration is indicated in the plot. **(H).** Magnitude of the relative discrepancy between the growth rates of the two fibril ends in (G).

The width of a fibril rendered by AFM is a convolution of the shapes of the fibril and the AFM tip (Fig. 2.3B) [131]. The thickness of the fibril, however, determined as the deviation from the height level of the mica substrate (Fig. 2.3B–D), does not suffer from similar exaggeration. We observe that the distribution of the fibrils thicknesses is bimodal, with maxima at 3 and 9 nm (Fig. 2.3E). The lower value is less than the filament thicknesses of both the threefold and twofold Aβ40 polymorphs but is comparable to the height of a single U-shaped protofilament [110, 119, 184]; fibrils consisting of single protofilaments

with mass-to-length ratio of about 9 kDa nm^{-1} (corresponding to a single chain of monomers with molecular weight 4.33 kDa and spacing of 0.47 nm) have been observed in populations of both polymorphs [213, 214, 216]. Consistent with expectations for seeds generated in stirred solutions and the propagation of fibril structure from seed to new growth we conclude that the thinnest fibrils in our experiments represent stand-alone protofilaments of the twofold symmetric polymorph [110, 119]. Evidence discussed below indicates that the thicker fibrils that we observe are likely bundles of filaments of this same twofold symmetric polymorph.

If protofilaments within the same fibril grow sufficiently fast so as to compete for a supply of monomers from the solution, then we would expect decreasing fibril growth rate as fibril thickness increases. The independence of the fibril growth rate of the fibril thickness (Fig. 2.3F) indicates that the convective-diffusive supply of monomers to the fibril end is not a rate-determining step of growth, in contrast to significantly faster (ca. 10 000-fold) growing sickle cell hemoglobin polymers [217, 218]. Importantly, this independence indicates that adjacent protofilaments do not cooperate to assist or hamper monomer incorporation into their respective tips. Thus, models of Aβ40 aggregation assuming single protofilaments are likely to predict adequately the growth dynamics of fibrils comprised of multiple protofilaments [113, 125].

The opposing ends of the majority of the monitored fibrils grow with rates that differ by less than 40% (Fig. 2.3G and H) and the magnitude of this difference is independent of the growth rate (Fig. 2.3H). The differences of the rates between the opposing fibril ends are within the range of variability of the growth rates of individual fibril ends (e.g., Fig. 2.2B). This approximate growth rate symmetry contrasts with

previous measurements of the growth dynamics of single fibrils of other proteins and peptides, including Aβ(25–35) and Aβ42, which showed significant asymmetry of the growth rates whereby one of the fibril ends was found to grow considerably faster than the other end [133, 137, 139, 140].

The majority of the growth rates of individual fibrils grown at identical conditions fall within 50% of the average for these conditions; rare measurements exceed the average by up to 500% (Fig. 2.4A). We tested whether the growth rate variability is due to the presence of different polymorphs in the population of fibrils that we studied (each growth rate data point in Fig. 2.2B and C, 2.3E–H, and 2.4A corresponds to an individual fibril end). Since distinct polymorphs are expected to grow with specific rates and the polymorph identity is preserved during growth, we determined the variability of growth rates evaluated from the displacement of single fibrils [110, 119]. For this, we divided the time evolutions of several fibril end displacements, like those shown in Fig. 2.1F, into segments of five overlapping data points and evaluated the growth rate corresponding to each segment of the time course (Fig. 2.4B, inset). The resulting distributions of the growth rates of individual fibrils (Fig. 2.4B) are comparable to those of batches of fibrils grown under identical conditions (e.g., Fig. 2.2B). This correspondence suggests that the growth rate variability is not due to polymorph diversity. The similarity of the growth rates of fibrils with thickness between 2 and 4 nm to those of thicker fibrils (Fig. 2.3F) strongly suggests that the majority of the fibrils observed here belong to the same twofold symmetric polymorph adopted by the seeds generated in stirred solutions.

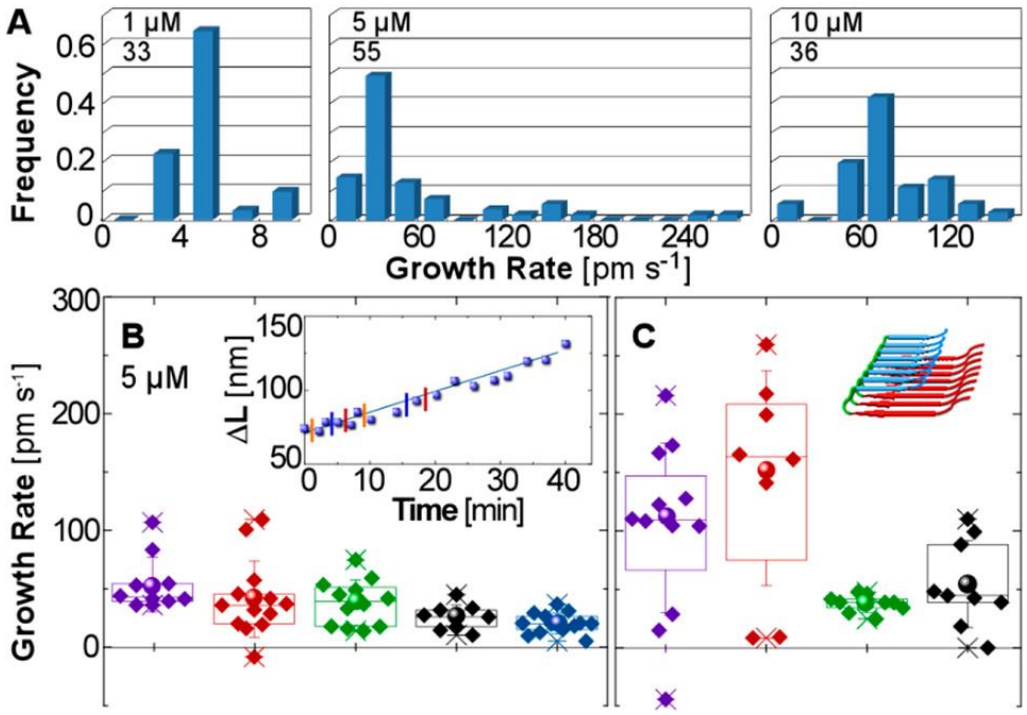

Fig. 2.4 Variability of Fibril Growth Rates.

Figure 2.4 **(A).** Distributions of fibril growth rates at Aβ40 concentrations indicated in the plots. Number of measurements indicated in each plot. **(B, C).** Jitter plots (for definition of notations, please see caption of Fig. 2.2) of growth rate distributions of individual fibrils at the concentration indicated in (B). (B) Determined from the five displacement evolutions in Fig. 2.1E. Color-coding corresponds to Fig. 2.1E. Inset. Illustration of the determination of R from overlapping segments consisting of five points belonging to same displacement ΔL trace in (B) and (C). Pairs of vertical bars of same color bracket ΔL data points used in individual determinations of R. (C) Determined from the displacement evolutions of four fibrils of thickness between 2 and 4 nm. Inset. Schematic of a single protofilament that likely constitutes fibrils with thickness between 2 and 4 nm.

It appears that the growth rate variability is not due to interactions between adjacent protofilaments belonging to the same filament. To see this, we evaluated the variability in the growth rates of individual fibrils with thickness between 2 and 4 nm (Fig. 2.4C) and compared the degree of variability of these thin fibrils to that of thicker fibrils. We assume that the fibrils with measured thicknesses between 2 and 4 nm are single protofilaments. The variability of the growth rates for the thinnest fibrils (Fig. 2.4C) is comparable to or greater than that of thicker fibrils (Fig. 2.2B).

The growth rate fluctuations (Fig. 2.4B and C) and the lack of cooperativity between the individual protofilaments comprising a fibril (Fig. 2.3F) may potentially lead to distinct lengths of the protofilaments and diminished fibril thickness close to the fibril end. We did not observe such thickness variations. A feasible interpretation is that the rate fluctuations are around average values governed by the peptide concentration. Thus, over extended times, the adjacent protofilaments reach similar lengths and the potential length differences are likely lower than can be detected, given the resolution limit of the AFM of about 1 nm.

2.5 Steady or Stop-and-Go Growth?

Stop-and go-kinetics, in which periods of stagnation alternate with bursts of growth, have been observed in several previous studies of amyloid fibrillization at constant supersaturation [137, 139, 144, 190]. The most commonly cited molecular mechanism for stop-and-go kinetics is that a monomer docked at the fibril end adopts a conformation (before or during docking) that impedes further monomer attachment [114]. Growth resumes after the capping monomer detaches or transitions to a conformation that more readily supports continued association [137, 144, 190]. The rest periods vary from several

minutes to several hours, and the lengths accrued between pauses reach between tens of nanometers and micrometers [137, 139, 144, 190].

To discriminate more carefully between steady kinetics and stop-and-go kinetics, we chose a fibril oriented roughly along the scanning direction, which significantly enhances the resolution of the recorded displacement (Fig. 2.5A) [131]. Previous meticulous measurements of the growth kinetics of a bacterial functional amyloid show that the pauses extend at lower supersaturation [139]. We therefore employed a relatively low concentration of Aβ40 of 1 μM to look for pauses. Over 18.5 min, the fibril grew by 4.8 nm, corresponding to an average growth rate of 4 pm s^{-1} (Fig. 2.5B). This evolution remained steady throughout the observation, at about 0.4 nm growth between images that were collected every 100 s (Fig 2.5A). This steady growth does not represent a burst stage since the corresponding growth rate is similar to the average of 33 determinations with independently grown fibrils, summarized in Fig. 2.4A. In all, we monitored the growth of about 200 fibrils at five Aβ40 concentrations ranging from 1 to 10 μM. We never detected any significant periods of stalled growth. Fibril end displacements always evolved steadily, similar to those shown in Fig. 2.1E.

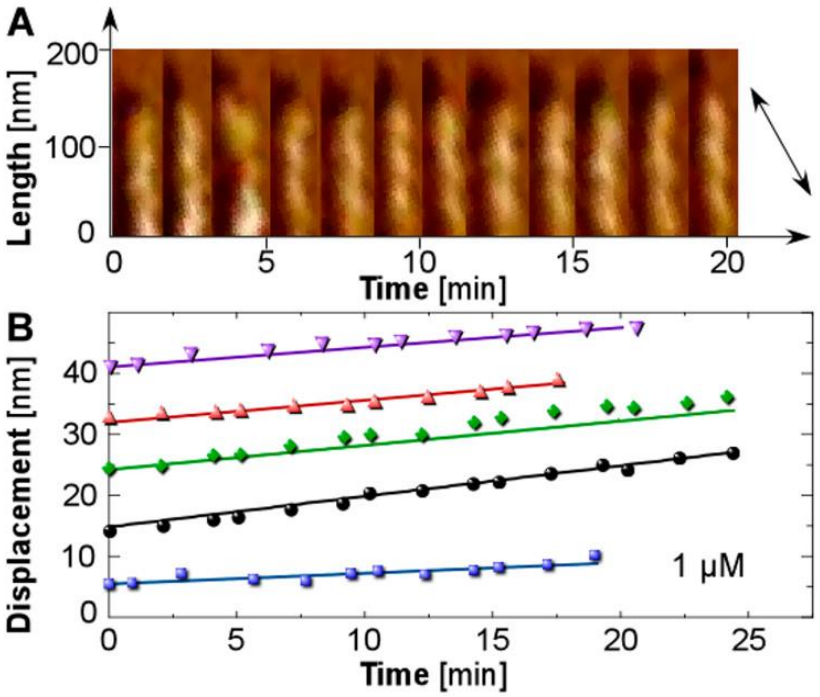

Fig. 2.5 Steady Growth of Fibrils.

Figure 2.5 **(A).** Sequence of images of a fibril growing at 1 μM concentration aligned using an immobile set point to reveal the growth of the fibril. Double sided arrow indicates scanning direction. **(B).** Evolutions of the displacement of the ends of five fibrils at Aβ40 concentration indicated in the plot. Bottom data set corresponds to the image sequence in (A).

The present observation of relatively steady growth contrasts with the results of a detailed previous investigation that did exhibit stop-and-go growth of Aβ40 fibrils [221]. We believe the diverging observations may arise from two differences of the previous studies from the present approach: First, in the previous study the seeds of the fibrils that grew by discontinuous kinetics were generated in quiescent solutions, which, as

highlighted above, favor threefold symmetric filaments [110, 119]. In contrast, the seeds we used were generated in agitated solutions, where mostly twofold symmetric filaments nucleate [110, 119]. Second, the previous studies monitored growth by total internal reflection fluorescent microcopy (TIRFM) in the presence of the dye ThT [221].This dye may itself associate with the active fibrils ends, intermittently poisoning growth.

2.6 Growth Reversibility and the Rate Constant for Monomer Association to the Fibril

Fibrils placed in contact with buffer free of Aβ40 dissolve (Fig. 2.6 A–D) without stirring or agitation, demonstrating the reversibility of Aβ40 fibrillization. Similar to the growth of fibrils in a supersaturated solution of the peptide, the dissolution of the fibrils proceeds at a relatively steady rate (Fig. 2.6E). The correlation between the net fibril growth rate R and the Aβ40 concentration C in the range 0–10 μM is linear (Fig. 2.7A). The slope of the correlation, $(8.4 \pm 0.17) \times 10^{-3}$ nm s^{-1} μM^{-1}, is near the previously reported value for the twofold symmetric Aβ40 fibril polymorph of $(8.68 \pm 0.11) \times 10^{-3}$ nm s^{-1} μM^{-1}, determined by monitoring the evolution of the average length of fibrils grown in bulk solutions [110]. The respective slope for the threefold symmetric polymorph, which was estimated in the same previous study, was lower, at 6.07 ± 0.23 nm s^{-1} μM^{-1} [110]. The close agreement between the kinetics measured here and determined previously for the twofold symmetric polymorph, as well as the significant difference with the threefold symmetric polymorph, provide additional support for our identification of the polymorph studied here as the twofold symmetric polymorph.

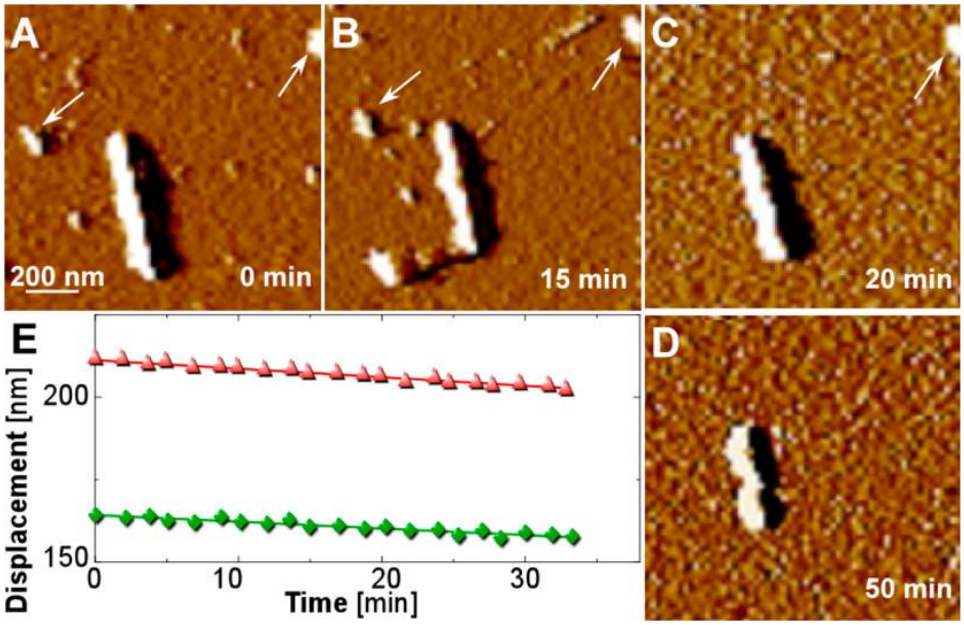

Fig. 2.6 Characterization of Aβ40 Fibril Dissolution.

Figure 2.6 **(A–D).** Time-resolved in situ AFM images showing the dissolution of an Aβ40 fibril in peptide-free buffer. Arrows indicate immobile reference points. **(E).** Evolutions of the displacements of two fibril ends and respective best-fit lines.

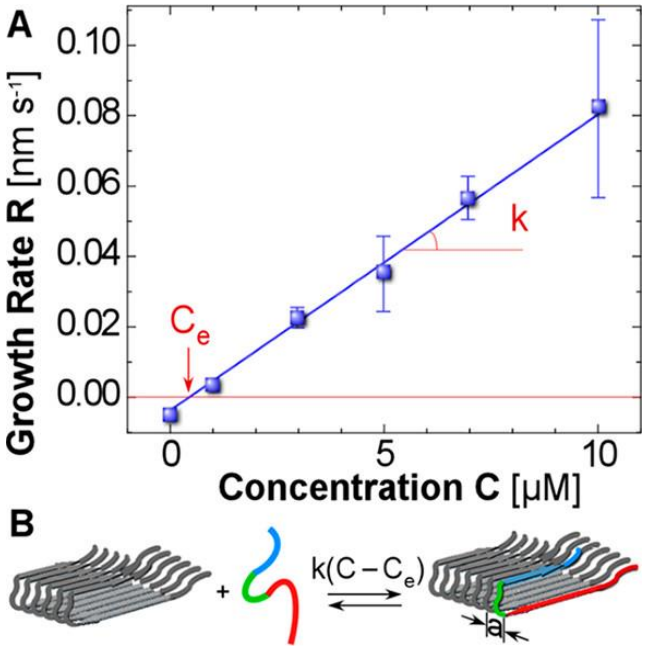

Fig. 2.7 Correlation between Fibril Growth Rate and Aβ40 Concentration.

Figure 2.7 **(A).** Negative growth rates correspond to dissolution. The vertical arrow indicates the concentration at which the fibrils are in equilibrium with the solution, the solubility C_e. The slope of the best-fit line defines the rate constant k. Error bars indicate standard deviation from the average of 20–50 measurements at each concentration. **(B).** Illustration of the relation between the net rate of monomer association to the fibril end $k_a(C - Ce)$ and the rate of fibril growth $R = ak_a(C - C_e)$.

The R(C) correlation crosses the line corresponding to zero growth at $C_e = 0.44 \pm 0.07$ μM, below which the negative values of R correspond to fibril dissolution (Fig. 2.7A). A solution with concentration C_e will thus be in equilibrium with the fibrils, so we can say C_e is the Aβ40 solubility with respect to the twofold symmetric fibril polymorph. The measured C_e is consistent with previous estimates of the solubility for the twofold

symmetric Aβ40 fibril polymorph of 0.40 ± 0.04 and 0.34 ± 0.06 μM that were found, respectively, by following the time evolution of the average length of fibrils grown in bulk solutions and by measuring the concentration of peptide left in solution after fibril growth was completed [110].

The apparent equilibrium between the fibrils and the solution should, of course, be regarded as metastable in view of the possible existence of more ordered condensed states, e.g., crystals or other polymorphs, which may have still lower free energy ΔG [222]. Even if such higher-order structures exist for Aβ40, they are kinetically avoided in the present study possibly owing to seeding with fibrils of a particular polymorph and the slow interconversion between different polymorphs. The ΔG difference between the fibrils studied here and a 1 M Aβ40 solution is the standard free energy of fibrillization $\Delta G^\circ = -k_B N_A T \ln K = k_B N_A T \ln C_e = -36.5$ kJ $mol^{-1} = -8.7$ kcal mol^{-1}, where k_B is the Boltzmann constant, N_A is the Avogadro number, T is temperature, and $K = C_e^{-1} = 2.3$ μM^{-1} is the fibrillization equilibrium constant. This value for ΔG° agrees with previous determinations [223].

The measured dissolution rate is equal in magnitude to the growth rate recorded at a concentration with equivalent deviation from the equilibrium concentration (Fig. 2.7A), implying that growth and dissolution are microscopically reversible. Microscopic reversibility would be violated if, for instance, growth occurred by monomer association, but if the fibril were to dissolve, in contrast, by discharging dimers or other oligomers; the latter scenario would enforce asymmetric rates of growth and dissolution. The observed microscopic reversibility of fibril growth and dissolution represents a reference point for future models of fibril growth and dissolution. The linear correlation between R and C

suggests that the Aβ40 species that associates with the fibril during growth and that dissociates from the fibril during dissolution is a monomer. The net rate of growth of an individual fibril, R, at a given solution peptide concentration, C, represents the algebraic sum of the addition rate, R_a, and the dissociation rate, R_d. We assume that the rate of the unimolecular dissociation reaction, wherein a monomer leaves the fibril tip to yield a free monomer and a shorter fibril, is independent of the solution monomer concentration. Since only dissociation occurs in the absence of solution monomers, the dissolution rate at zero solution peptide concentration can be used to determine the intrinsic dissociation rate. The measured dissolution rate in the absence of solution monomers, R = −4.4 pm s^{-1}, can be converted into a dissociation rate of monomers from a single fiber end in units of molecules per second using the known spacing between monomers along the fibril axis, a = 0.47 nm (Fig. 2.7B) [213, 216]. This conversion yields a dissociation rate of $R_d = 9.4 \times 10^{-3}$ molecules s^{-1} for a fibril end.

Supported by the linear R(C) correlation, we assume that growth of fibrils occurs via the addition of monomers from the solution to an existing fibril end to yield a longer fibril. The rate of the bimolecular reaction between a monitored fibril end and solute monomers is proportional to the concentration of monomers in the solution, $R_a = k_aC$. If, rather than a single fiber study, we carried out a bulk experiment with many free fiber ends, the total rate would also be proportional to the concentration of these ends. When the solution monomer concentration is equal to the equilibrium concentration, $C = C_e = 0.44$ μM, the rates of dissociation and addition are equal in magnitude, $R_d = R_a(C_e) = k_aC_e$. With $R = a(R_a – R_d)$, the rate law corresponding to the linear R(C) correlation (Fig. 2.7A) is $R = ak_a(C – Ce)$. Using the slope of the R(C) correlation, 8.4×10^{-3} nm s^{-1} μM^{-1}, and the spacing

between monomers, a = 0.47 nm, we determine $k_a = 1.8 \times 10^4$ M^{-1} s^{-1}. This value is well below the diffusion limit for reactions in solution of about 10^{10} M^{-1} s^{-1}, indicating that the monomer addition reaction is not diffusion-limited, and a relatively large free energy barrier must be overcome to incorporate a monomer into a fibril. It therefore seems likely that the rate-limiting step of this reaction involves a conformational rearrangement that occurs from a pre-equilibrium where a monomer binds, but nonspecifically, to the fibril tip before transforming into the next growth-competent fibril tip configuration, as has been suggested by previous theoretical work [113, 125, 180]. The experimental approaches that could address this process will be discussed in detail in Chapter 3.

2.7 Conclusions

We have demonstrated that time-resolved in situ atomic force microcopy provides a way directly to measure the growth rates of individual Aβ40 fibrils without introducing complicating features that may confuse other commonly employed techniques. The ability faithfully to characterize the growth kinetics of individual amyloid fibrils provides an opportunity to explore the specific mechanistic details that control monomer association to fibrils.

We have identified the Aβ40 fibrils studied here as the twofold symmetric polymorph based on the good correspondence between the fibril growth rate constant to previous determinations for this polymorph. The population of fibrils includes not only single protofilaments but also filaments and bundles of filaments. The growth rate, however, turns out to be independent of the fibril thickness, implying that adjacent protofilaments do not cooperate to assist or hamper monomer incorporation into their respective tips. Correspondingly, models of Aβ40 monomer association to single

protofilaments may adequately describe the growth of thicker fibrils. The fibrils of the polymorph we studied grow steadily. The opposing ends of the fibrils grow with similar rates. These observations contrast with the "stop-and-go" kinetics and asymmetric growth that have been observed with amyloids formed from other peptide fragments or from Aβ40 whose seeds were generated differently and thus likely belong to the threefold symmetric polymorph.

The linear correlation between fibril growth rate and concentration suggests that the Aβ40 species that associates with the fibril during growth and dissociates from the fibril during dissolution is a monomer. Growth and dissolution of the Aβ40 amyloids are microscopically reversible, i.e., the sequence of molecular-level events leading to incorporation of a monomer to a fibril is exactly reversed during dissolution. The observed microscopic reversibility and unimolecular mechanisms of fibril growth and dissolution represent important reference points for models of fibril growth and dissolution.

The observed reversibility of fibrillization and symmetry of growth and dissolution allows the determination of the Aβ40 solubility with respect to the twofold symmetric fibril polymorph, as the interpolated concentration where the net rate of growth is zero. The solubility, C_e = 0.44 μM, and the standard free energy of fibrillization, ΔG° = −36.5 kJ mol^{-1} = −8.7 kcal mol^{-1}, determined from the solubility, agree with previous determinations for the twofold symmetric polymorph.

The correlation between fibril growth rate and concentration corresponds to a rate coefficient for association of monomers to the fibril end $k_a = 1.8 \times 10^4$ M^{-1} s^{-1}. This value is significantly slower than the diffusion limit implying that the transition state for incorporation of a monomer into a fibril of the twofold polymorph features a relatively

high free energy. The rate-limiting step of this reaction may involve a conformational rearrangement of a monomer nonspecifically bound to the fibril tip to a growth-competent configuration.

2.8 Supplementary Results

The results presented in this section serve as validation to procedures in the method section.

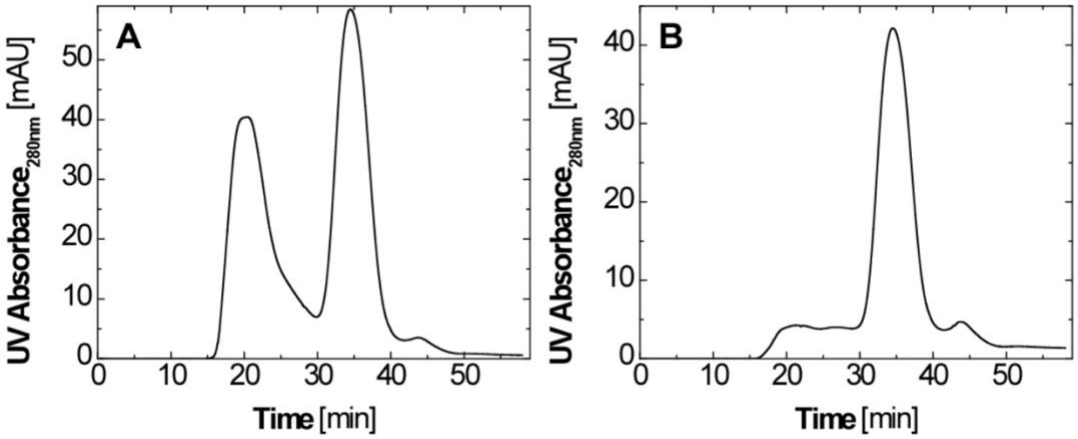

Fig. 2.8 SEC Chromatograms of Aβ40 Solution.

Figure 2.8 **(A).** Chromatogram of SEC separating Aβ(M1-40) from 30k MWCO retentate. UV absorbance at 280 nm recorded by built-in detector of ÄKTA Pure System. **(B).** Chromatogram of SEC separating Aβ(M1-40) from 3k MWCO retentate. The peak at 35 minutes correspond to the desired Aβ(M1-40) peptide.

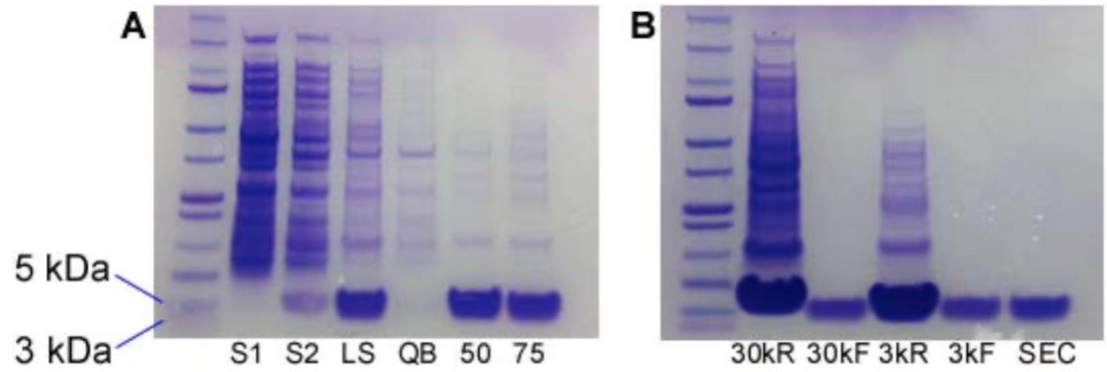

Fig. 2.9 SDS-PAGE Monitoring of Purification.

Figure 2.9 **(A-B).** Electrophoresis on 4%-12% Bis-Tris gels of all fractions eluted from chromatography column. Leftmost lanes are protein molecular weight standards (Position Plus Protein Dual Xtra, BIO-RAD), relative molecular weight indicated in the figure. Lowest band in each lane corresponds to Aβ40. S1, supernatant after first round of sonication and centrifugation; S2, supernatant after second found; LS, whole cell lysate after solubilizing with urea; QB, supernatant after binding cell lysate to Q-Sepharose; 50, elution using buffer with 50 mM NaCl; 75, elution using buffer with 75 mM NaCl; 30kR, retentate of 30 kDa MWCO filtration; 30kF, filtrate of 30 kDa MWCO filtration; 3kR, retentate of 3 kDa MWCO filtration; 3kF, filtrate of 3 kDa MWCO filtration; SEC, peak fractions of desired Aβ40 peptide from SEC separation.

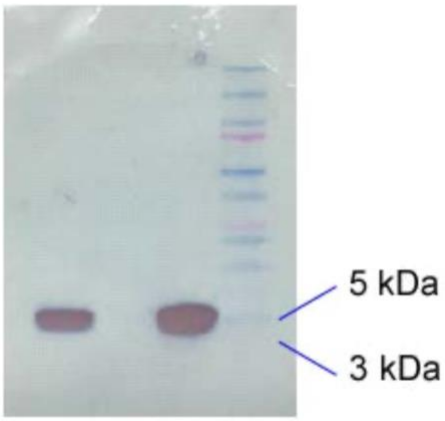

Fig. 2.10 Western Blot.

Figure 2.10 The color appearances of both lanes confirm the presence of Aβ40. Left lane shows the SEC fraction same as in Fig. 2.9B. Middle lane shows the concentrated fraction of the SEC fraction. Right lane represents the same protein molecular weight standards used in Fig. 2.9.

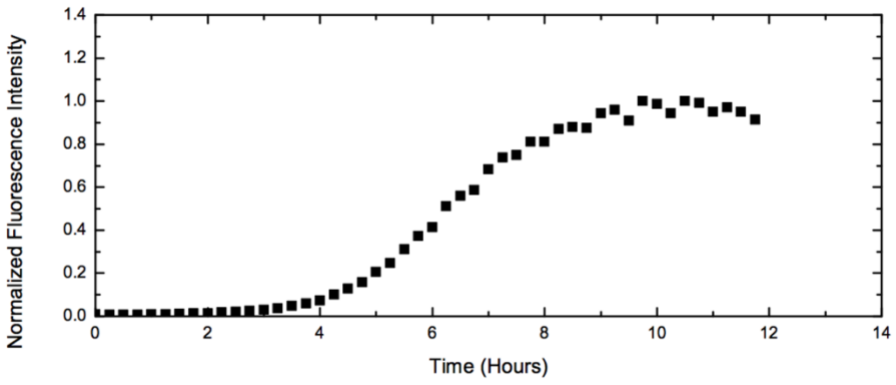

Fig. 2.11 ThT Monitoring of Fibril Growth.

Figure 2.11 ThT fluorescence assay of Aβ40 fibril formation over the period of 12 hours. Fibrils rich in β-sheet structure starts to appear after four hours indicated by increasing fluorescence signal. Fibril formation completes after 10-12 hours.

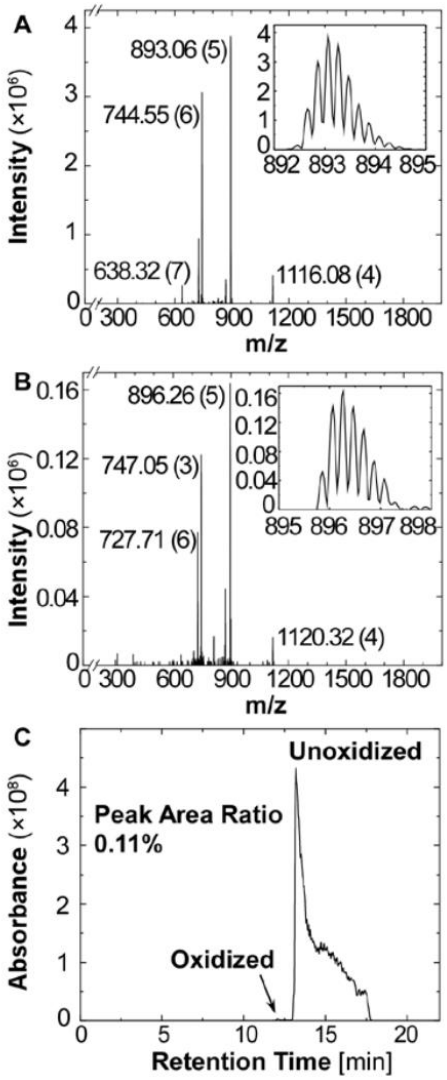

Fig. 2.12 LC-MS Characterizations of the Aβ(M1-40) Peptide.

Figure 2.12 **(A).** The mass spectrum of the unoxidized Aβ(M1-40) peptide. The inset shows a zoom-in of the peak at m/z 893.06 (5). m/z of major peaks is indicated. Numbers in

parenthesis represent the charges carried by the molecules. **(B).** The mass spectrum of the oxidized Aβ(M1-40) peptide. The inset shows a zoom-in of the peak at 896.26 (5) The mass difference between the unoxidized and the oxidized peptide is 16 g mol^{-1}, corresponding to one oxygen atom. **(C).** Chromatogram of the Aβ(M1-40) peptide sample. The fractions represented by the oxidized and the unoxidized peaks were used for the mass spectrometry. The peak area ratio between the oxidized and the unoxidized fraction is shown in the plot. The amount of oxidized peptide is insignificant.

Chapter 3: Frustrated Peptide Chains at the Fibril Tip control the Kinetics of Growth of Amyloid-β Fibrils

3.1 Background

To elucidate the intermediate state of Aβ fibrillization, we synergistically join experiments with simulations. We examine the mechanisms of Aβ fibril growth by monitoring individual fibrils as in Chapter 2. Of the two reagents in the bimolecular reaction between fibril tips and the dissolved peptides that leads to fibril growth, the fibril tips are at a concentration lower by orders of magnitude than the peptide concentration. Hence, insight into the structures and dynamics of the fibril tips may potentially provide a route to block fibrillization by agents operational at substantially lower concentrations than those needed to suppress other stages of fibrillization. Our most-powerful tools are the correlations between the measured growth rates, peptide concentration in the solution, and the effect of denaturant, which directly illuminate the mechanism of peptide incorporation and can be compared quantitatively to computer simulations. For insights on the energetics of the intermediate and transition states for fibril incorporation, we study the effect of added urea, whose impact on the formation of interchain and intrachain contacts is relatively well understood from studies of protein folding. The direct determination of individual fibril growth rates that we employ affords the opportunity to elucidate the mechanistic complexity arising from the concurrent binding and folding of the incoming peptide chains [224].

3.2 Materials and Methods

All procedures regarding solution preparation, Aβ expression and purification, fibril formation and AFM sample preparation and formation are the same as those

described in Chapter 2.2 unless specified otherwise. In AFM sample preparation, urea (Sigma Aldrich) was added to fibril incubation buffer based on experiment needs, i.e., adjusted to different concentrations.

The Growth of Freshly Cut Fibrils. Existing fibrils deposited on the AFM substrate were monitored under AFM for several minutes as described above. To cut a fibril, we chose a relatively long one, which spanned about 50% of the image width. To ensure a good cut we rotated the scan angle so that the angle between the fibril and fast scan direction angle was at least 45 degrees. To increase the force of interaction between the tip and the fibril, we lowered the amplitude set point to 50% or 60% of the original value and set the scan frequency to 1 Hz to better control the length of the cut out. After the cut was complete, we reset the set point and the scan frequency to their original values to monitor the growth of the freshly cut ends.

3.3 Kinetics of Fibril Growth

To examine the growth of Aβ40 fibrils, we use time-resolved in situ AFM as in Chapter 2 (Fig. 3.1). We deposit fibril seeds on mica and monitor the growth of both fibril ends towards fixed reference points (Fig. 3.1A) in solutions of Aβ40 monomer with known concentrations. We evaluate the fibril growth rate as the slope of the time correlation of the fibril tip displacement (Fig. 3.1E). Previous work in Chapter 2 revealed that the fibril growth rates, and solubility measured using in situ AFM are close to those determined from time-dependent bulk growth of fibrils in solution [110]. This comparison certifies that interactions with the substrate that may strain the fibrils or assist the supply of monomers to the fibril tip do not modify the growth rates, in contradistinction to results with Aβ42, the short amyloid peptide Aβ(12–28), and amylin [112, 116, 143]. We also established that

the opposite ends of individual fibrils grow at similar rates and the growth was relatively steady in Chapter 2. Time resolved in situ AFM monitoring of fibril growth revealed that the fibrils readily dissolved in quiescent peptide-free solutions (Fig. 3.1B and F).

The addition of urea led to a significant increase of the fibril solubility: the fibrils dissolved at concentrations at which they otherwise grew in urea-free solutions (Fig. 3.1C). Urea-induced thermodynamic fibril destabilization, manifested as higher solubility, is consistent with urea's known activity as a universal protein denaturant owing to its favorable interaction with the amide groups of the peptide backbones [223, 224]. This interaction impairs not only the formation of contacts between segments of a single chain that support folded protein structures but also the formation of contacts between distinct chains within amyloid fibrils [145]. Increasing the peptide concentration in the presence of urea, however, leads to growth rates significantly faster than the values recorded at the same peptide concentration in the absence of urea (Fig. 3.1D). The acceleration of fibril growth in the presence of urea would appear to be contrary to destabilization of the contacts that support the fibril structure [227].

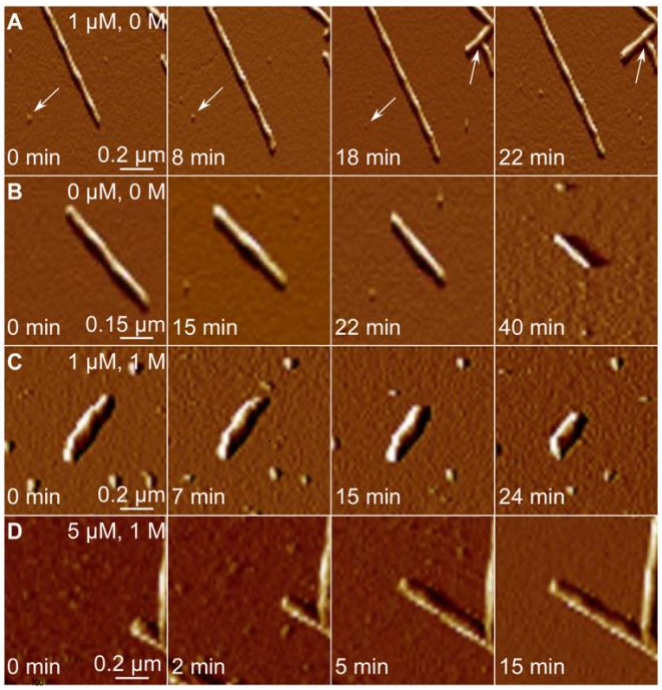

Fig. 3.1 (1) Growth and Dissolution of Aβ40 Fibrils.

Figure 3.1 (1) **(A–D).** Time-resolved in situ AFM images of the evolution of growth and dissolution of Aβ40 fibrils at different concentrations of Aβ40 in μM and urea in M. Arrows in A point to references to measure the displacement of fibril tips.

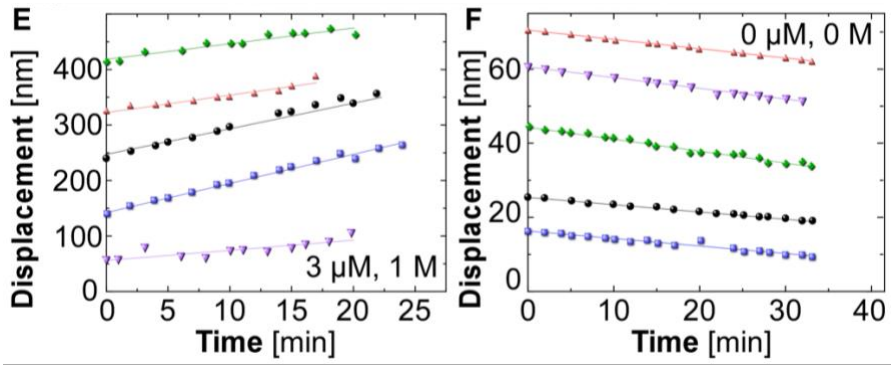

Fig. 3.1 (2) Growth and Dissolution of Aβ40 Fibrils. (E, F).

Figure 3.1 (2) Evolutions of ten fibril ends. Straight lines represent best fits to determine fibril growth rates. E. Fibril growth at Aβ40 at 3 μM in the presence of 1 M urea. F. Fibril dissolution in peptide-free and urea-free buffer.

The correlation between the fibril growth rate R and the Aβ40 concentration C is linear (Fig. 3.2A). The observed linearity implies that the fibrils grow by association of the dominant solution Aβ40 species, whether it be monomer, dimer, or a heavier oligomer [228]. Whereas oligomers of varying compositions are present in Aβ solutions, they reside in equilibrium with the monomers, which capture the majority of the peptide mass in the solution [229]. Growth by association of oligomers in equilibrium with a majority of monomers would manifest as a superlinear (e.g., quadratic, for growth by dimer association) R(C) correlation [228]. We tentatively conclude that Ab40 fibrils grow by association of monomers.

The R(C) correlation crosses the interpolated line of zero growth at C_e = 0.44 ± 0.07 μM from Chapter 2. For C below C_e, the negative values of R correspond to fibril dissolution (Figs. 3.1B and 3.2A). A solution with concentration C_e is in equilibrium with the fibrils (i.e., C_e is the Aβ40 solubility with respect to the fibrils). The equilibrium F_n + M ⇄ F_{n+1}, where F_n and F_{n+1} denote fibrils that differ in length by one monomer M, is characterized by a constant K = $[M]_e^{-1}$, since the addition of a monomer does not modify the fibril concentration and $[F_n]$= $[F_{n+1}]$. Considering the dominance of monomers in the solution, we approximate the equilibrium monomer concentration $[M]_e$ by the total peptide concentration C_e at equilibrium with the fibrils and arrive at K = C_e^{-1} .

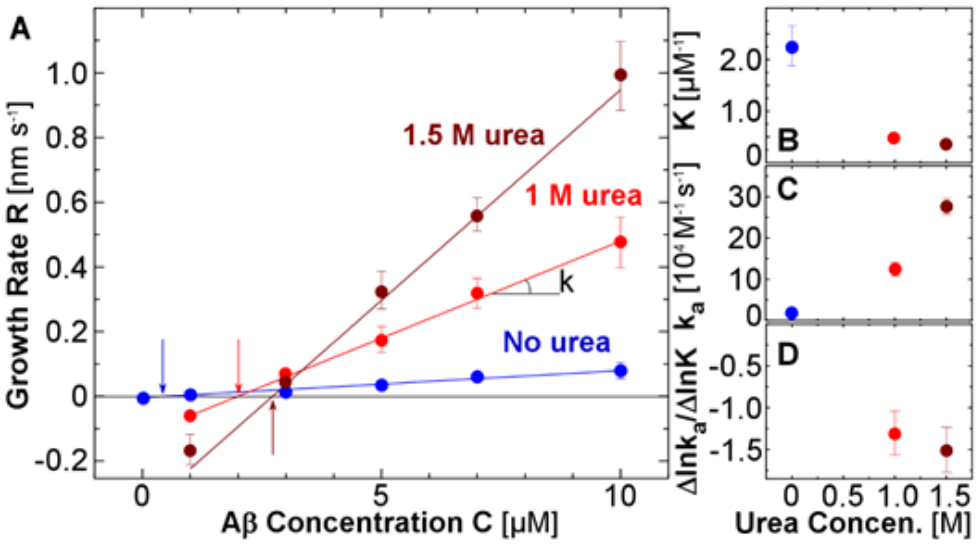

Fig. 3.2 (1) The Kinetics of Aβ40 Fibril Growth.

Figure 3.2 (1) **(A).** The dependences of the growth rates R of individual fibrils on the concentration C of Aβ40 in the absence and the presence of urea at two concentrations. The error bars correspond to the SD from the mean for 20 to 50 measurements illustrated in Fig. 3.1E and F. The arrows mark the respective solubilities C_e. The rate constants k_a are determined from the slopes of the linear correlations. Data in the absence of urea are from Chapter 2. **(B, C).** The equilibrium constant $K = C_e^{-1}$ in B and the rate constant k_a, in C for fibrillization in the absence and presence of urea at two concentrations determined from the R(C) correlations in A. **(D).** The ratio $\Delta \ln k_a = \Delta \ln K$, evaluated from the data in B and C. The error bars in B–D indicate SDs from the mean values evaluated from the R(C) correlations in A.

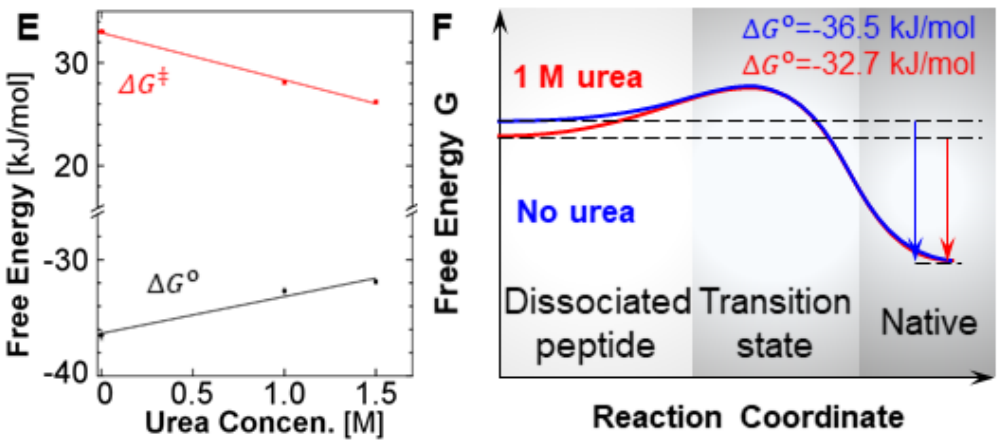

Fig. 3.2 (2) The Kinetics of Aβ40 Fibril Growth.

Figure 3.2 (2) **(E).** The correlations of the free energies for fibrillization ΔG^{o} and of the transition state for incorporation $\Delta G^{\ddagger}$ with the urea concentrations. The error bars indicate the SDs of ΔG^{o} and $\Delta G^{\ddagger}$ and are smaller than the symbol size for most data points. **(F).** Schematic of the free energy landscape along a direct pathway of incorporation of a peptide chain into a fibril tip that does not involve any intermediate states.

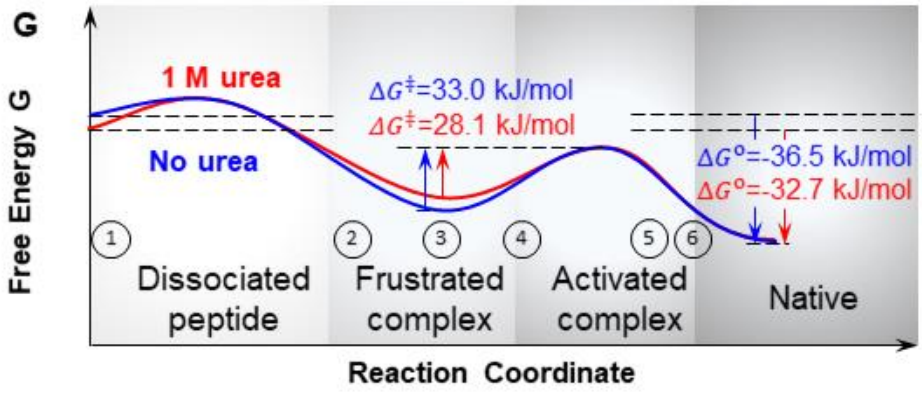

Fig. 3.2 (3) The Kinetics of Aβ40 Fibril Growth.

Figure 3.2 (3) **(G).** Schematic of the free energy landscape along a pathway of incorporation of a peptide chain into a fibril tip that passes through a frustrated intermediate state. The encircled numbers denote approximate locations along the reaction coordinate of the conformations depicted in Fig. 3.3A. In F and G, blue curves and blue $\Delta G^{\ddagger}$ and ΔG^{o} values characterize association to fibrils in the absence of urea, red curves and red $\Delta G^{\ddagger}$ and ΔG^{o} values, in the presence of 1 M urea.

For insights into the mechanisms that guide faster growth in the presence of urea despite the fibril destabilization that this denaturant enforces, we measured the R(C) correlations at two concentrations of urea, 1 and 1.5 M, and compared them to R(C) data in urea-free solutions (Fig. 3.2A). At the three tested compositions, fibrillization was reversible. The growth and dissolution dynamics revealed by AFM images (Fig. 3.1C and D) and the R(C) correlations (Fig. 3.2A) demonstrate that urea acts as an apparent catalyst for growth and dissolution. It leads to both faster fibril growth and faster dissolution (Fig. 3.2A), while increasing the Aβ40 solubility with respect to the fibrils. The solubility boosts with added urea define gains of standard free energy of fibrillization, $\Delta G^{o} = -RT \ln K = RT \ln C_e$, from -36.5 ± 0.4 kJ mol^{-1} in the absence of urea to -32.7 ± 0.3 kJ mol^{-1} at 1 M urea and -31.9 ± 0.2 kJ mol^{-1} at 1.5 M urea, i.e., about 3 kJ mol^{-1} (mole urea)$^{-1}$ (Fig. 3.2E)]. The increasing ΔG^{o} announces the expected urea-enforced destabilization of the fibrils relative to the solute monomers. We use fibrils seeds that were generated without urea, and previous work has established that the structure of a fibril persists after the growth conditions deviate from those during fibril nucleation [109, 183, 184]. The uniformity of the fibril structure during growth in the presence and absence of urea ascribes the

destabilization of the fibrils relative to the solution to urea-imposed lower free energy of the solute peptide chains (Fig. 3.2 F and G). We model the linear R(C) correlation as $R = ak_a(C - C_e)$, where a = 0.47 nm is the contribution of an incorporated monomer to the protofilament length [214], and k_a is the bimolecular rate constant for the reaction between monomers and fibril tips. We define protofilament as a single stack of peptide chains (Fig. 3.5) [215, 228], although alternative definitions exist [212, 213, 216]. The expression for R is akin to the result of a model, which assumes a two-step reaction of monomer association to the fibril tip, followed by incorporation into the fibril, under conditions where the first step is rate-limiting [110]. The constant k_a assumes values between 1.8×10^4 and 2.8×10^5 M^{-1} s^{-1}, depending on the urea concentration (Fig. 3.2C). These values are significantly slower than the expected diffusion limit for association of about 10^{10} M^{-1} s^{-1} [115]. The rate constant can be written as $k_a = k_o \exp(-\Delta G^{\ddagger}/k_B T)$, where k_B is the Boltzmann constant and T is temperature. We assume $k_o = 10^{10}$ M^{-1} s^{-1} as the diffusion limit [115]. It has been argued that k_o for Aβ40 fibril growth should be closer to 10^9 M^{-1} s^{-1} [110]; the exact value of k_o, however, does not modify the arguments presented below. We assume that the rotational and orientational entropy contributions to k_o are not substantially affected by urea. We note that urea increases the solution viscosity by 4% at 1 M and 6% at 1.5 M [231]. Accounting for this increase would depress the values of $G^{\ddagger}$ in the presence of urea by about 0.1 kJ mol^{-1}, which is within the experimental uncertainty of this variable (Fig. 3.2E). With this, the free energy barrier $\Delta G^{\ddagger}$ decreases from 33.0 ± 0.1 kJ mol^{-1} in the absence of urea to 28.1 ± 0.2 kJ mol^{-1} at 1.0 M urea and to 26.2 ± 0.2 kJ mol^{-1} at 1.5 M urea, that is, the barrier reduces by about 4 kJ mol^{-1} (mole urea)$^{-1}$ (Fig. 3.2E and G). Importantly, the correlation between $\Delta G^{\ddagger}$ and the urea concentration is linear

(Fig. 3.2E). In analyses of protein folding kinetics, such linearity is taken as evidence that urea does not greatly modify the conformation of the transition state. In folding, observed kinetics nonlinearities have been shown to correlate to flatter free energy profiles with "malleable" transition states [29]. The linearity here, while based on only three concentrations, suggests that lack of urea-enforced structure change in the transition state is a good first approximation.

3.4 A Frustrated Complex at the Fibril Tip

The opposing activation free energy $\Delta G^{\ddagger}$ and fibrillization free energy ΔG^{o} responses to urea eliminate certain mechanisms of amyloid fibril growth that have previously been suggested based on simulations. One such proposal assumes that monomeric peptides undergo a conformational transformation into an aggregation-prone state, whose lifetime is longer than the time required for collision with a fibril tip [129]. In this scenario, the depression of the free energy of the peptides in the solution enforced by urea would boost the free energy barrier for incorporation (Fig. 3.2F) and impose slower fibril growth, contrary to actual observations. From a broader perspective, the opposing $\Delta G^{\ddagger}$ and ΔG^{o} trends defy any mechanism that constrains the urea impact to the peptide chains in the solution.

The essential identity of the bulk fibril structure in the presence and absence of urea eliminates urea-driven bulk fibril structure modifications as the mechanism that regulates the high sensitivity of $\Delta G^{\ddagger}$ to urea. The exclusion of peptides in the solution and fibril structure as targets for urea attack implies an incoming chain passes through an intermediate state, in which it attaches, but only partially, to the fibril tip. The substantial magnitude of $\Delta G^{\ddagger}$ and its sensitivity to urea together imply that the intermediate complex

is bound by strong hydrophobic contacts, distinct from the native contacts that support the fibril structure and dictate ΔG^{o}. The unraveling of the initial nonnative contacts between the incoming and terminal fibril monomers, in search of the native conformation typical of the bulk fibril, becomes the rate-limiting step for the attachment of the monomer to the fibril tip and contributes to $\Delta G^{\ddagger}$. The extension of the linear R(C) correlation to dissolution in undersaturated solutions (Fig. 3.2A) indicates that disorder at the tip is an equilibrium feature of the fibril structure. Urea, by interacting with the backbones of monomers at the fibril tip, weakens the nonnative contacts and thereby destabilizes the intermediate state, which lowers $\Delta G^{\ddagger}$ (Fig. 3.2G) [230, 231]. Importantly, the linear correlation of $\Delta G^{\ddagger}$ with the urea concentration (Fig. 3.2E) indicates that the urea-induced weakening of the nonnative contacts likely stops short of modifying the structure of the intermediate and transition states. In protein folding, such energy-rich nonnative contacts have been called frustrated [234]. Whereas simulations have foreseen frustrated states as amyloid peptides fold to incorporate into fibrils [111, 125, 205], the opposing $\Delta G^{\ddagger}$ and ΔG^{o} responses to urea, based on the divergent effects of urea on fibril solubility and growth rate, provide direct experimental evidence for the role of frustration in fibrillization.

The pathway of association of peptides with the fibril tips suggested by the rates of fibril growth (Fig. 3.2) shares certain features with a mechanism put forth by simulations. In this mechanism, the incorporation of a monomer into a fibril divides in two steps. First, the association of an unstructured monomer to the fibril tip (often called docking), followed by conformational rearrangement toward the peptide structure in the fibril bulk (locking) [115, 206]. In the simplest lock-and-dock scenario, the conformational transformation of each captured peptide chain is templated by the previously arrived peptide. The magnitude

of $\Delta G^{\ddagger}$ and the opposing $\Delta G^{\ddagger}$ and ΔG^{o} trends that we observe advocate a more complex picture whereby the docked state evolves to a frustrated complex, in which a monomer makes many nonnative contacts in the fibril tip.

Additional characteristics of the frustrated complex emerge when we quantitatively compare the urea-induced weakening of the frustrated contacts to what is seen for protein unfolding [237]. Statistics over 45 proteins have revealed that urea-induced lowering of the free energy of unfolding scales with the protein surface area exposed to solvent upon unfolding [237]. This proportionality indicates that the thermodynamic effect of urea of about 3 kJ mol^{-1} $(mole\ of\ urea)^{-1}$ is associated with the loss of about 3,200 $Å^2$ of solvent accessible surface area (SASA) upon monomer incorporation into the fibril; we designate this loss as$\Delta SASA^0 = -3200\ Å^2$. The urea-induced activation free energy drop of about 4 kJ mol^{-1} $(mole\ of\ urea)^{-1}$ corresponds to the exposure of $\Delta SASA^{\ddagger} = 5{,}300\ Å^2$. The evaluations of $\Delta SASA^0$ and $\Delta SASA^{\ddagger}$ afford the opportunity to compare the results of the kinetics experiments to those of simulations and thus attain additional insights in the incorporation pathway.

3.5 Interaction of the Monomer with the Fibril Tip during Binding and Folding

To achieve greater molecular-level understanding of how an incoming peptide chain acquires the structure typical of the fibril bulk as it incorporates into a fibril, we carried out simulations using the associative memory, water-mediated structure, and energy model for molecular dynamics (AWSEM-MD) [238]. The coarse-grained nature of the AWSEM simulation Hamiltonian leads to much more rapid sampling than models with explicit solvent molecules. Owing to the lack of solvent, 1 ps of simulation time compares to longer than a nanosecond of laboratory time. We used the Protein Database entry 2LMN,

the polymorph examined with AFM in Chapter 2, to construct the fibril structure. We evaluated the free energy profile for an incoming monomer to associate with a fibril composed of five chains arranged in a single stack (Fig. 3.3A). We characterized the conformational ensembles in terms of the distance between the center of mass of the peptide chain and the fibril end and by the similarity of the structure of the incoming monomer to that of a chain in the fibril bulk (Fig. 3.3B). We explored about 30 select configurations, divided into six groups, along the reaction pathway (Fig. 3.3A and B). We then computed the SASA of fully atomic models generated from the coarse-grained structures (Fig. 3.3C).

The computed change, $\Delta SASA_{eq} = SASA_6 - SASA_1$ (Fig. 3.3C), defines the sensitivity of the equilibrium ΔG^o to the addition of denaturant, and the model result $\Delta SASA_{eq} = 3400$ Å^2 agrees well with the estimate based on the measured urea dependence of the fibril solubility. The simulations reveal that the SASA passes through a minimum at position 3 (Fig. 3.3A and C). In this group of structures, an incoming monomer partially binds to itself forming nonnative inter- and intrachain contacts rather than forming native contacts with the fibril tip (Fig. 3.3A and B). These frustrated contacts must unravel as the peptide reconfigures to fully integrate into the fibril in the cluster 6 structures, labeled in Fig. 3.3B. Remarkably, the finding of an intermediate frustrated complex at the fibril tip agrees with the conclusions implied by the responses of experimentally measured $\Delta G^{\ddagger}$ and ΔG^o to added urea.

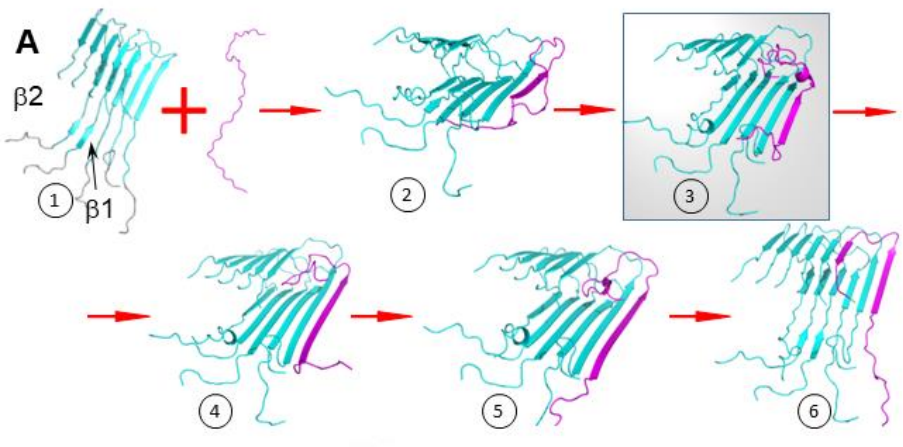

Fig. 3.3 (1) Microscopic View of Monomer Association to a Fibril Tip.

Figure 3.3 (1) **(A).** Select successive conformations of a monomer peptide (magenta) associating to an even end (where the β-1 strand of a 2LMN protofilament is open) of a fibril comprised one protofilament (cyan), computed using AWSEM-MD simulations. 1, a dissociated peptide; 2 to 5, intermediate conformations; 6, peptide fully integrated in the fibril.

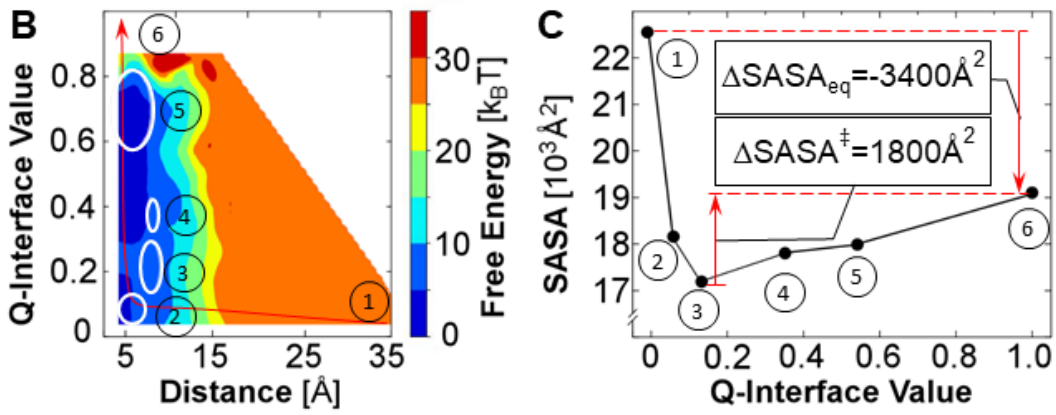

Fig. 3.3 (2) Microscopic View of Monomer Association to a Fibril Tip.

Figure 3.3 (2) **(B).** The free energy as a function of the distance from monomer end and Q-interface, which measures the similarity of the monomer structure to that in the fibril bulk. The white ovals next to 2 to 5 highlight pools of conformations, from which respective SASAs were sampled and averaged. The red arrow schematically depicts a reaction pathway. **(C).** Total SASA of the fibril and monomer in positions 1 to 6. Computed $\Delta SASA_{eq}$, corresponding to equilibrium, and $\Delta SASA^{\ddagger}$, representative of the activation barrier, are shown.

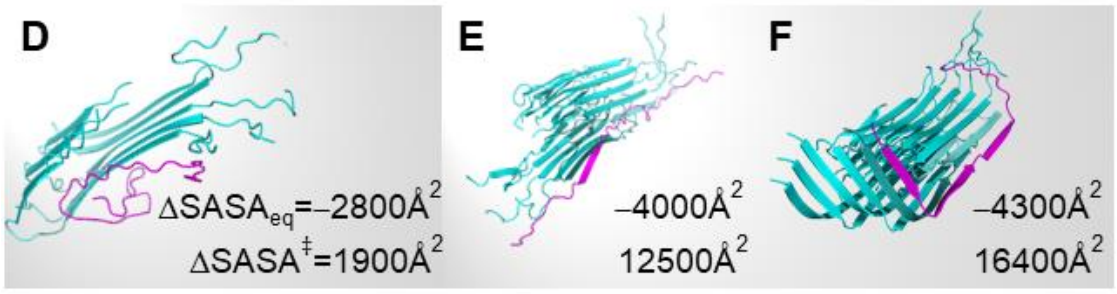

Fig. 3.3 (3) Microscopic View of Monomer Association to a Fibril Tip.

Figure 3.3 (3) **(D–F).** Conformations of a monomer peptide (magenta) associating with three different fibril tips (cyan) at which SASA is minimal, as conformation 3 in A. Listed negative areas represent $\Delta SASA_{eq}$ and positive areas, $\Delta SASA^{\ddagger}$. **(D).** The odd end of a 2LMN fibril comprised of one protofilament. **(E).** A fibril comprised of two protofilaments of equal length. **(F).** A fibril comprised of two protofilaments, of which one is longer by one monomer.

The positive ΔSASA between positions 3 and 6 represents only a rough estimate of the effects of urea on the activation free energy $\Delta G^{\ddagger}$. All-atom simulations of the

conformations of the peptides at the fibril tip yield $\Delta SASA^{\ddagger}$ = 1800 Å^2. The results for monomer association to the opposite, odd, fibril end (Figs. 3.3D and 3.7) are similar. Importantly, both values of $\Delta SASA^{\ddagger}$ are only about one-third of the value inferred from the response to urea of the growth kinetics of individual fibrils, measured by AFM. The discrepancy between the simulated and measured $\Delta SASA^{\ddagger}$s suggests that the structure of the frustrated complex at the fibril tip is probably more elaborate than what has emerged from these initial simulations.

We envision two possible models of a more elaborate frustrated intermediate. First, the frustrated complex may involve more than one peptide chain within a single protofilament; the ratio between the experimental and simulated $\Delta SASA^{\ddagger}$ suggests that three or four monomers would need to be involved. Simulations of a peptide chain association with a disordered fibril tip would involve characterizing a multidimensional free energy landscape and require significant additional efforts. Alternatively, the intermediate frustrated state may involve binding of the incoming monomers to both protofilaments in a filament. The experimentally measured thicknesses of the fibrils monitored by AFM indicate that the majority of the filaments are built of two parallel protofilaments, represented by the 2LMN structure in Chapter 2.

We explore the possibility where the incoming peptide chain associates to both protofilaments in a filament. We note that the addition of monomers to a double filament must ultimately preserve the structure of the twinned protofilaments, and this involves at least two alternating conformations of the fibril tip: one where the two protofilaments exactly match in length and one where one of the protofilaments is ahead by one monomer. AWSEM simulations of monomer attachment to the tip of a two-protofilament structure

reveal that, instead of folding on top of one of the two monomers at the fibril tip, an incoming peptide chain spans both stacks and enforces a stabilized frustrated conformation that may be incapable of further growth (Figs. 3.3E, F and 3.8). This state was predicted for both the matched and the mismatched protofilaments (Fig. 3E and F). $\Delta SASA^{\ddagger}$ from such frustrated states to the final conformation are greater than 12000 $Å^2$ (Fig. 3E and F).

3.6 The Growth of Fibrils with Bulk Structure of Their Tip

To discriminate experimentally whether the complex frustrated state at the fibril tip recruits more than one disordered peptide chain that crown a single protofilament or structures as a single chain that spans both protofilaments in a filament, we monitored the growth rates of freshly cut fibrils (Fig. 3.4A). In freshly cut fibrils, the peptides at the tip initially should carry the structure of monomers in the fibril bulk, and an intermediate state composed of more than one frustrated chain may not have had time to evolve. Thus, if the slow growth rate observed in the AFM experiments is due to a frustrated complex composed of several chains, freshly cut fibrils will grow faster than fibrils with normal tips. By contrast, if the high $\Delta G^{\ddagger}$ deduced from AFM experiments is due to interactions of a single incoming chain with two adjacent protofilaments, the frustrated complex that crowns the freshly cut fibril tips will be identical to the one at equilibrated tips, and the freshly cut tips will grow with rates similar to those of normal tips.

The AFM measurements reveal that freshly cut fibrils initially grow about twice as fast as fibrils with equilibrated tips (Fig. 3.4B and C). In five of the cut fibrils, the growth rate transitioned to its “normal” value after 6 to 8 min, during which time the fibrils grew about 10 nm (Fig. 3.4B). The observed faster growth rates indicate that the freshly cut fibrils carry a simpler frustrated complex than equilibrated fibril tips. For a second test of

the distinction between the kinetics of growth of freshly cut and mature fibrils, we measured the effects of 1 M urea on the growth of freshly cut fibrils and compare them to the growth rate of mature fibrils (Fig. 3.4C). The results reveal that urea accelerates the growth rate constant of freshly cut fibrils by about threefold, significantly weaker than its ca. sixfold effect on normal tips (Fig. 3.4C).

Collectively, the outcomes of the two tests with freshly cut fibrils indicate that the frustrated complex at equilibrated fibril tips comprises more than one peptide chain but is probably constrained to a single protofilament.

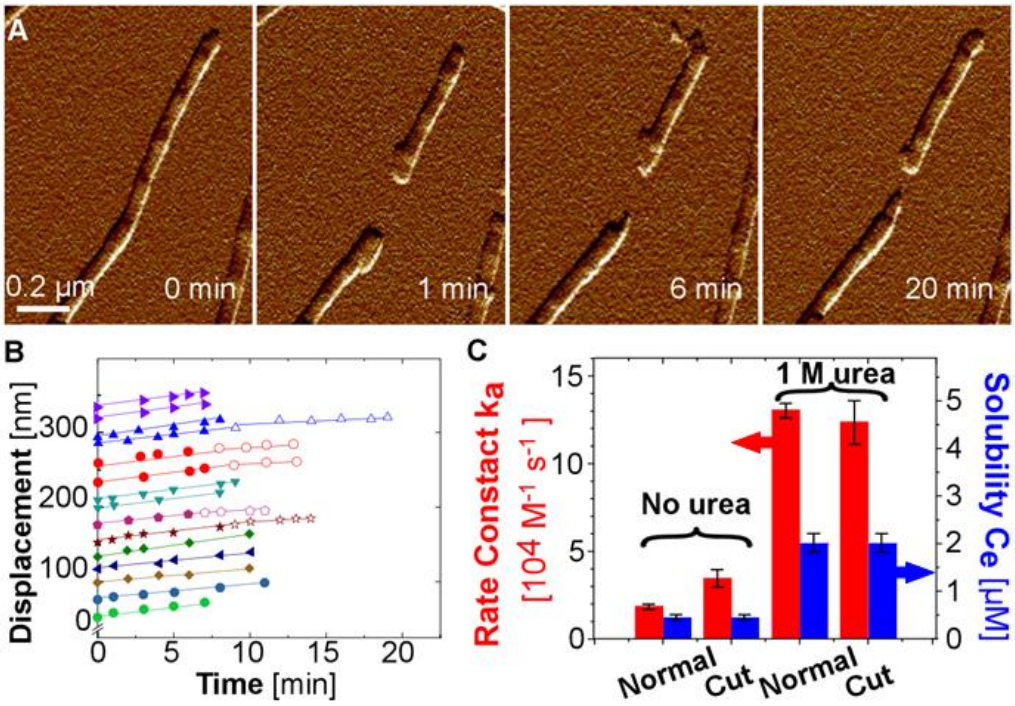

Fig. 3.4 The Growth of Fibrils with Bulk Structure of the Peptides at the Tip.

Figure 3.4 **(A).** AFM micrographs of growth of freshly cut fibrils. **(B).** The displacement of the freshly cut ends. Five of the freshly cut tips transition to slower growth depicted with

open symbols. **(C).** The rate constants k_a (red bars and Left axis) and the solubilities C_e (blue bars and Right axis) of fibrils with normal equilibrated tips and with freshly cut tips in the absence of urea and in the presence of 1 M urea. The error bars represent the SD from the mean evaluated from about 400 fibril tip displacement measurements for the normal fibrils and 100 fibril tip displacement measurements for the freshly cut as in Fig. 3.2A and C.

3.7 Conclusions

Time-resolved in situ AFM measurements of the growth kinetics of individual fibrils and molecular simulations suggest a two-step mechanism of growth of Aβ40 fibrils, whereby an incoming monomeric solute peptide first associates to a complex residing at the fibril tip and composed of several other monomers that have nonnative conformations. The unraveling of the frustrated initial contacts during the conformational rearrangement of one of the constituent peptides to the bulk fibril structure constitute the rate-limiting step for fibril assembly. The proposed reaction pathway should help guide the search for fibrillization inhibitors by finding small molecules that bind to the frustrated complex at the fibril tip and increase the free energy cost of rearranging it.

In a broader context, our findings indicate that the coupled dynamics of structuring and assembly during fibril growth are more complex than observed for the folding of most globular proteins, since they involve the collective motions of several peptide chains that comprise the initial frustrated complex and simultaneously strain nonnative contacts in the transition state. Furthermore, the substantial kinetic consequences of this frustrated complex indicate that fibril growth does not enjoy a fully funneled energy landscape.

In the context of Alzheimer's disease, the low concentration of fibril tips in the fibrillization reaction mixture suggests that the tips may be suitable targets for attack by potential suppressors of fibrillization. The distinct structure of the fibril tip proposed here may guide the computational search for small molecule compounds and antibodies that bind to the tip and stunt fibril growth.

3.8 Supplementary Results

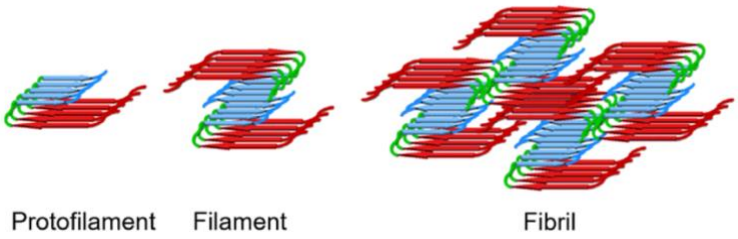

Fig. 3.5 The Structure Hierarchy of the Two-fold Symmetric Aβ40 Fibrils.

Figure 3.5 Schematic of the structures of a protofilament, a two-fold symmetric filament composed of two protofilaments, and a fibril comprising several filaments.

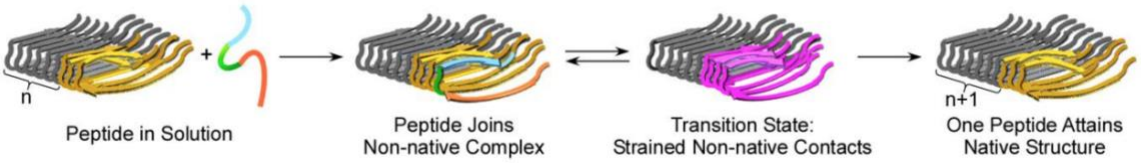

Fig. 3.6 Schematic of the Reaction Mechanism of Fibril Growth Suggested by the Correlations of the Rate Constant ka and the Fibrillization Equilibrium Constant K with the Concentration of Urea.

Figure 3.6 Aβ40 peptides with native contacts in the fibril bulk are drawn in gray; peptides at fibril tip with non-native contacts, in gold; peptides in solution and newly attached to non-native complex at fibril tip, in blue, green, and orange; peptides with frustrated contacts that constitute the transition state, from which one of them attains native structure, are drawn in pink. n denotes the number of peptides in native conformation in the fibril bulk.

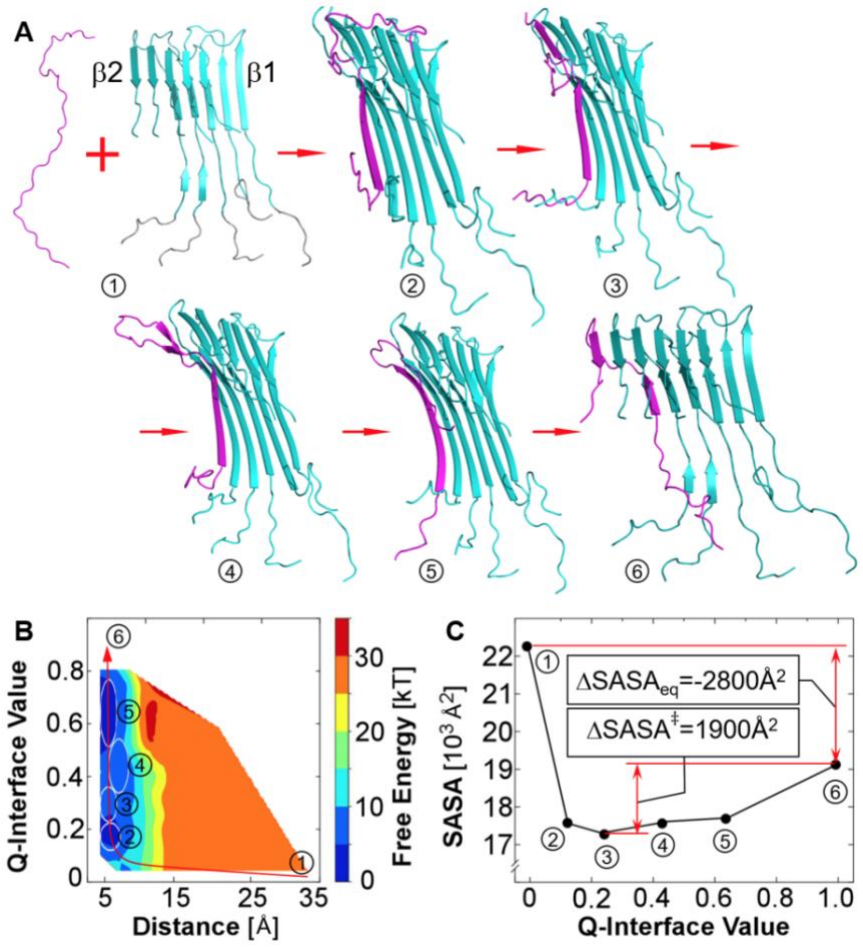

Fig. 3.7 AWSEM – MD Simulations of the Association of an Aβ40 Peptide Monomer to the Odd Fibril End, where the β2 Strand is Open.

Figure 3.7 **(A).** Select successive conformations of a monomer peptide (magenta) and a fibril end (cyan) computed using AWSEM-MD. 1, a dissociated peptide; 2 – 5, intermediate conformations; 6, peptide fully integrated in the fibril. Grey tails in conformation 1 depict eight residues added to the N-terminus of each chain to fill the void in the published structure of the 2LMN polymorph (see discussion in Methods and Fig. 3.9). **(B).** The free energy as a function of the distance from monomer end and Q-interface, which measures the similarity of the monomer structure to that in the fibril bulk. Ovals next to 2 – 5 highlight pools of conformations, from which respective SASAs were sampled and averaged. Red arrow schematically depicts reaction pathway. **(C).** Total solvent accessible surface area (SASA) of the fibril and monomer in positions 1 – 6. Computed $\Delta SASA_{eq}$, corresponding to equilibrium, and $\Delta SASA^{\ddagger}$, representative of the transition state, are shown.

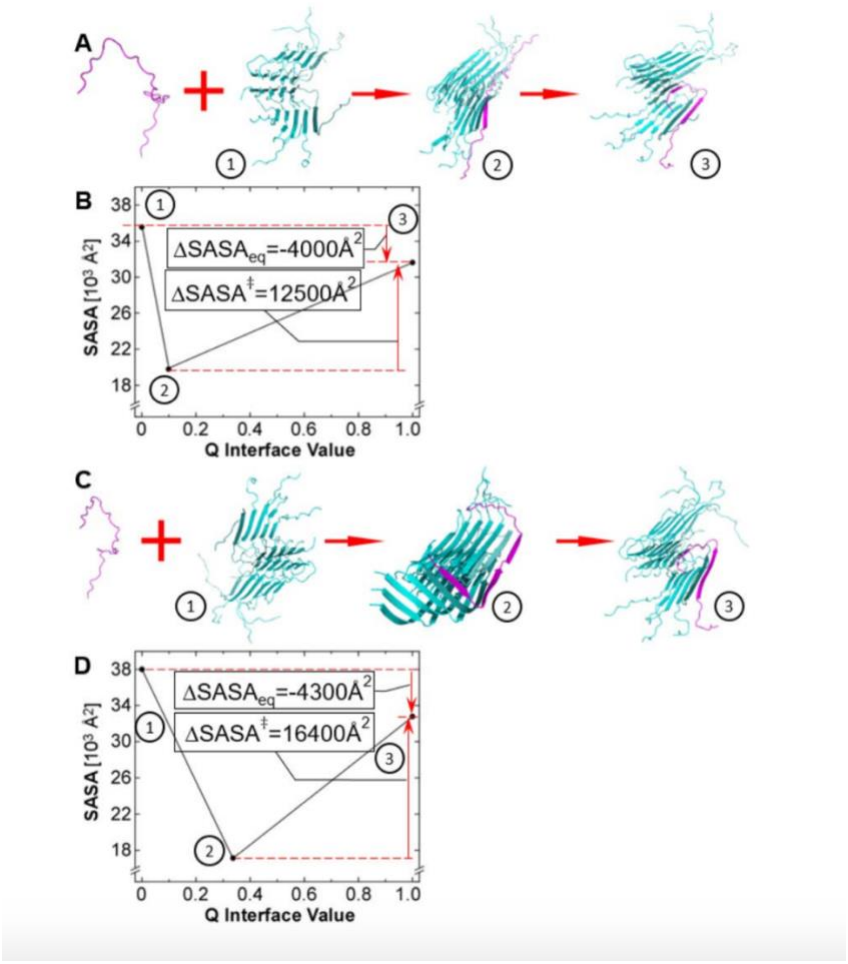

Fig. 3.8 AWSEM – MD Simulations of the Association of an Aβ40 Peptide Monomer to a 2LMN Filament Composed of Two Protofilaments.

Figure 3.8 **(A-B).** The tow protofilaments contain the same number of monomers and are aligned at the fibril tip. **(C-D).** One of the protofilaments is longer by one monomer. **(A and C).** Select successive conformations of a monomer peptide (magenta) and a fibril end (cyan) computed using AWSEM-MD. 1, a dissociated peptide; 2, intermediate conformation; 3, peptide fully integrated in the fibril. **(B and D).** Total solvent accessible surface area (SASA) of the fibril and monomer in positions 1 – 3. Computed $\Delta SASA_{eq}$,

corresponding to equilibrium, and $\Delta SASA^{\ddagger}$, representative of the transition state, are shown.

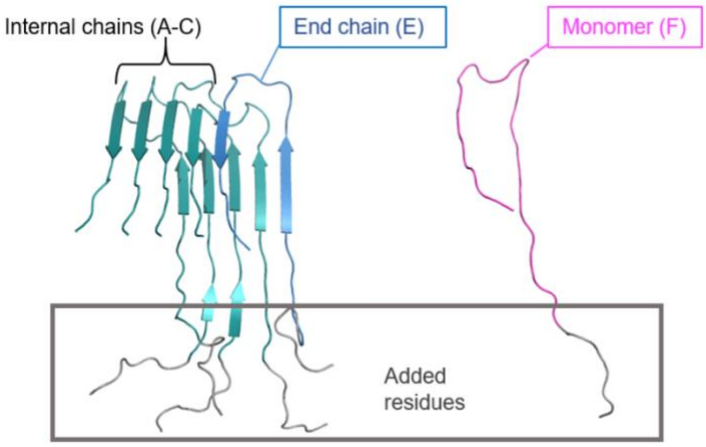

Fig. 3.9 The Structures of the Aβ40 Monomers and Fibrils Assumed in the AWSEM – MD Simulations.

Chapter 4: The Role of Amyloid-β E22 Residue and the Accelerated Fibrillization of E22Q Amyloid-β Dutch Variant

4.1 Backgrounds

Dutch variant E22QAβ is responsible for one type of early-onset AD, cerebral amyloid angiopathy (CAA), caused by extensive amyloid deposition near the vasculature. Position 22 plays an important role in both inter- and intra- molecular interactions and is heavily involved in the frustrated intermediate state of Aβ fibrillization as indicated in simulation study [125]. We proved experimentally, in Chapter 3 that there exist multiple frustrated peptide chains at the fibril tip that control the kinetics of growth of Aβ fibrils. In order to gain insights on how the Dutch variant E22QAβ fibrillizes differently from the wild type, we employed similar techniques and rationales to design and perform experiments with the AFM. The E22QAβ peptide exhibits a ~ 35% lower solubility than the wild type but ~15 times higher fibril growth rate constant, confirming the role of E22 residue in the frustrated contacts that impedes the growth of Aβ fibrils. This also implies the change of the free energy barrier associated with monomer rearranging dominates over the destabilization of the Aβ monomer because of the mutant [155]. Urea elicits similar response from E22QAβ peptide solubility and fibril growth rate constant as in the wild type, except that the effect on rate constant enhancement is weaker, indicating a simpler frustrated complex. The kinetics of growth of freshly cut fibrils corroborate the conjecture that E22QAβ carries a simpler frustrated complex in the equilibrium structure of the fibril tip.

Our experiment is a good indication that the change of specific contacts in the Aβ affects the fibrillization kinetics via modifying the frustrated intermediate complex and the intermediate state with frustrated monomers exists solely based on the premature contacts between the incoming monomer and the existing fibril instead of being based on native contacts between fibrils and the monomer.

4.2 Materials and Methods

All procedures regarding solution preparation, Aβ expression and purification, LC/MS analysis, fibril formation, AFM sample preparation and operation, and freshly cut fibril experiment are the same as in Chapters 2.2 and 3.2 unless specified otherwise.

PCR and E22QAβ40 Dutch Variant Cloning Procedures. pET-Sac-Abeta(M1-40) plasmid inserted in E. coli DH5alpha was purchased from Addgene as a template for constructing plasmid for Dutch variant Aβ40 peptide. The E22Q replacement was achieved by two pairs of primers: 5'- CTCCCTTATGCGACTCCTGC- 3' (forward primer upstream of position 22); 5'- TGTTAGAACCCACGTCCTGAGC- 3' (reverse primer near position 22); 5'- GCTCAGGACGTGGGTTCTAACA- 3' (forward primer near position 22); 5'- GAGGCCCTTTCGTCTTCAAG- 3' (reverse primer downstream of position 22). Primer sequences were sent to Integrated DNA Technologies and the primers were sent to us in lyophilized powder and were dissolved to 100 μM and stored in -20 °C for future use.

To produce Dutch variant Aβ40 plasmid insert, a 50 μL reaction mix of 1x Phusion High-Fidelity GC buffer (NEB), 200 μM deoxynucleoside triphosphate (dNTPs), 0.5 μM primers (one pair per reaction), 50 ng template plasmid and one unit of Phusion DNA polymerase (NEB) was prepared in nuclease free water. The mix was then subject to 30 PCR cycles with an annealing temperature of 57 °C. The two resulted Dutch variant inserts

(458 kb upstream of position 22 and 608 kb downstream of position 22) were separated by agarose gel and recovered using a gel recovery kit. To prepare the vector for Dutch variant Aβ40, the original pET-Sac-Abeta(M1-40) plasmid was digested by EcoRI and EcoNI restriction enzymes in CutSmart Buffer (NEB) and separated by agarose gel and recovered using the same kit. The two inserts and the vector were subsequently subject to Gibson Assembly in NEBuilder Hifi DNA assembly Master Mix (NEB) to construct the plasmid with Dutch variant insertion.

The Dutch variant plasmid obtained from previous steps was transformed into E. Coli BL21(DE3) by electroporation and incubated in 1 mL of SOC at 37 °C for one hour. The entire SOC culture was then pelleted and 800 μL was discarded. The 200 μL culture containing the cells was spread on LB agar plate with 100 μg ml^{-1} ampicillin and incubated at overnight. The next morning, 5 isolated colonies were picked and inoculated into 5 mL of LB culture with 100 μg/ml ampicillin at 37 °C. After the OD_{600} reached desired level, the cells were pelleted, and the Dutch variant Aβ40 plasmid was extracted using a QIAprep Spin Miniprep Kit (QIAGEN).

4.3 Growth Kinetics of E22QAβ40

To monitor the growth of Aβ40 fibrils, we use time-resolved in situ AFM just as in Chapters 2 and 3 (Fig. 4.1). We deposit fibril seeds on mica and monitor the growth of both fibril ends in solutions of E22QAβ40 monomer with known concentrations. We evaluate the fibril growth rate as the slope of the time correlation of the fibril tip displacement as in Chapters 2 and 3. The work in Chapters 2 and 3 indicated that the fibril growth rates, and solubility measured using in situ AFM are close to those determined from time-dependent bulk growth of fibrils in solution [110]. We also established that the opposite ends of

individual fibrils grow at similar rates and the growth was relatively steady in Chapter 2. Our data show that E22QAβ40 fibrils share similar behaviors as the WTAβ40 fibrils.

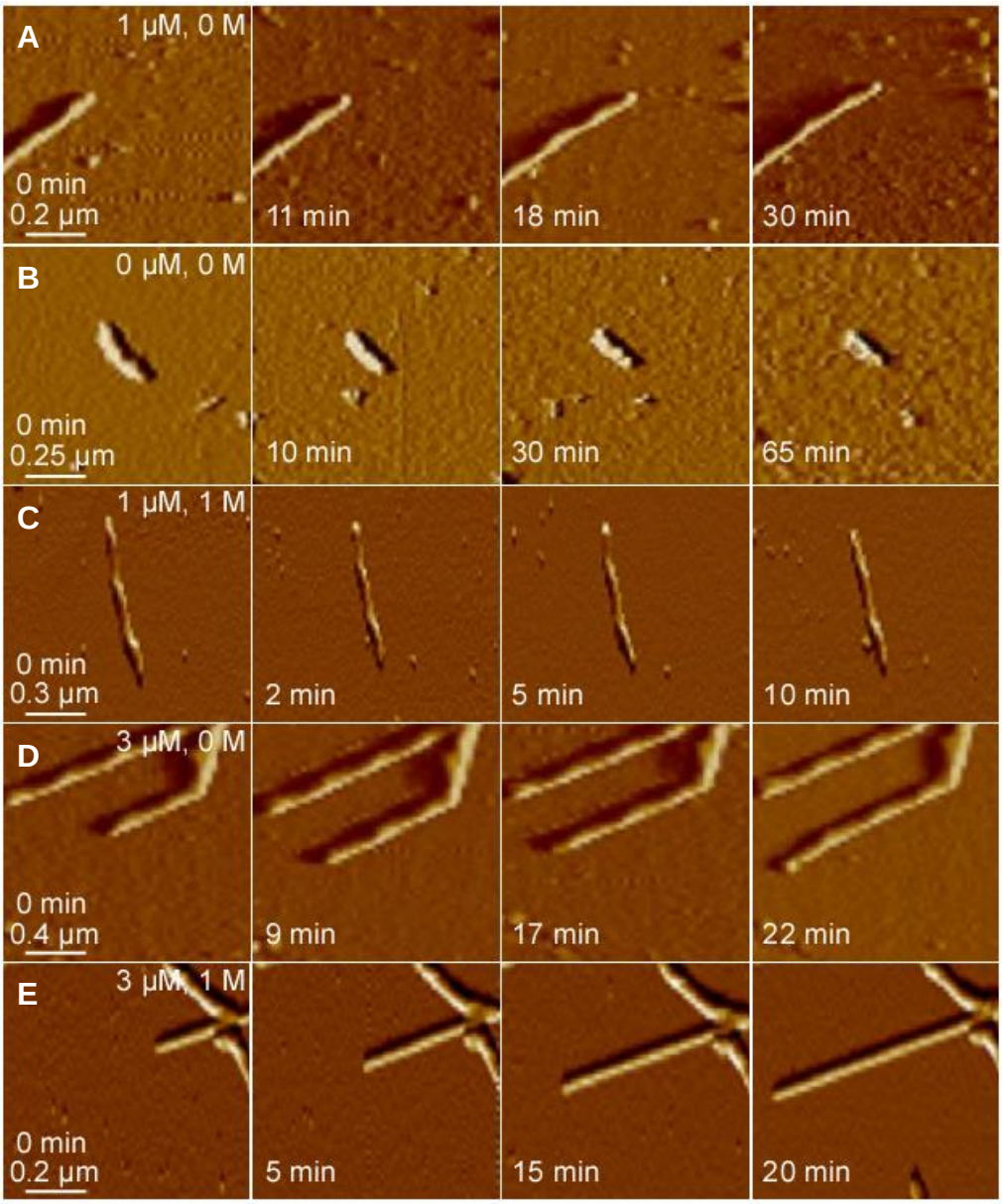

Fig. 4.1 Growth and Dissolution of E22QAβ40 Fibrils.

Figure 4.1 **(A-E).** Time-resolved in situ atomic force microscopy monitoring of the evolution of growth and dissolution of E22QAβ40 fibrils at different concentrations of E22QAβ40 in μM and urea in M.

The addition of urea led to a significant boost of the fibril solubility: the fibrils dissolved at concentrations at which they otherwise grew in urea-free solutions (Fig. 4.1A and C). Urea's known function as a chaotropic protein denaturant via interacting with amide groups of peptide backbones includes thermodynamic fibril destabilization and boosts peptide solubility. Similar behavior was observed using WTAβ40 fibrils in Chapter 3 [223, 224]. Adding urea to the system, however, leads to growth rates faster than the values recorded at the same peptide concentration in the absence of urea (Fig. 4.1D and E). The stimulated fibril growth in the presence of urea would appear contrary to destabilization of the contacts that support the fibril structure [225].

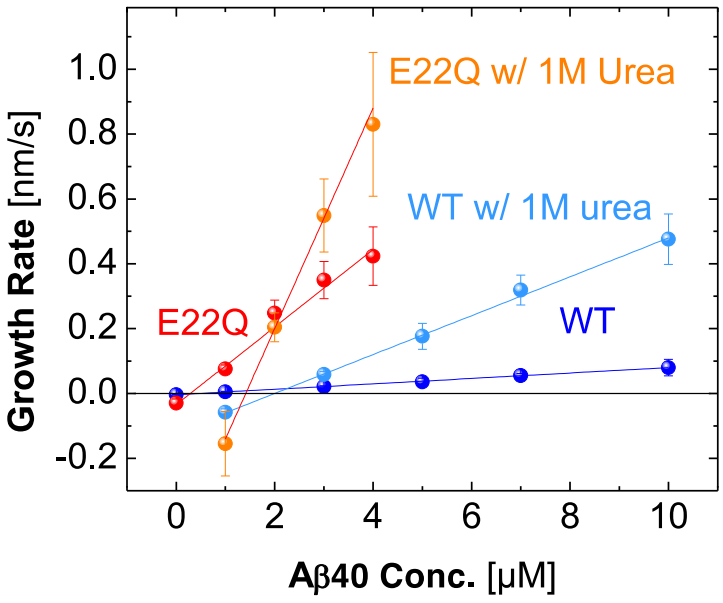

Fig. 4.2 Growth Kinetics of E22QAβ40 in Comparison to WTAβ40.

Figure 4.2 The dependences of the growth rates of individual fibrils on the concentrations of E22QAβ40 in the absence and the presence of 1 M urea in comparison to WTAβ40. The error bars correspond to the SD from the mean for 20 to 50 measurements. The intercepts with x-axis mark the respective solubilities C_e. The rate constants ka are determined from the slopes of the linear correlations.

The correlation between the fibril growth rates and the E22QAβ40 concentrations is linear (Fig. 4.2), similar to that for WTAβ40, implies that the fibrils grow by association of the dominant solution Aβ40 species, whether it be monomer, dimer, or a heavier oligomer [228]. We tentatively conclude that E22QAβ40 fibrils grow by association of monomers just as do WTAβ40 fibrils. The growth-rate-concentration correlation crosses the interpolated line of zero growth at $C_e = 0.29 \pm 0.03$ μM. Negative values of growth rate correspond to fibril dissolution (Fig. 4.1B and C). A solution with concentration C_e is in equilibrium with the fibrils (i.e., C_e is the Aβ solubility with respect to the fibrils). We approximate the equilibrium monomer concentration $[M]_e$ with the total peptide concentration C_e at equilibrium with the fibrils and arrive at $K = C_e^{-1}$. With 1 M urea in the system, the solubility increases to $C_e = 1.4 \pm 0.1$ μM. The E22QAβ40 has a ~35% lower solubility than WTAβ40, indicating poorer stability in solution. It is consistent with multiple simulation studies, which concluded that E22QAβ40 has a more flexible hydrogen bonding network in the β turn region and its central hydrophobic core is destabilized, leading to a less stable peptide when in solution [155, 209].

To examine the frustrated complexes at the Dutch variant fibril tip, we measured the growth-rate-concentration correlations in the presence of 1 M urea (Fig. 4.2). The growth and dissolution dynamics revealed by AFM images (Fig. 4.1) and the correlations (Fig. 4.2) demonstrate that urea acts as a stimulus for growth and dissolution. It leads to both faster fibril growth and faster dissolution (Fig. 4.2), while increasing the E22QAβ40 solubility with respect to the fibrils. The solubility boosts with added urea define gains of standard free energy of fibrillization, $\Delta G^o = -RT \ln K = RT \ln C_e$, from -37.5 ± 0.7 kJ mol^{-1} in the absence of urea to -33.6 ± 0.2 kJ mol^{-1} at 1 M urea, about 4 kJ mol^{-1} (mole urea)$^{-1}$. The increasing ΔG^o corroborates the anticipated urea-triggered destabilization of the fibrils relative to the solute monomers. We use fibrils seeds generated without urea and only added urea during AFM experiments to ensure the same polymorphism, and previous work has established that the structure of a fibril persists even with growth conditions distinct from those during fibril nucleation [109, 183, 184]. In addition, the urea effect on ΔG^o of E22QAβ40 is comparable to that of WTAβ40, further implying the structural similarities between the two peptides [64, 155, 157, 159, 209].

We model the linear growth-rate-concentration correlation as $R = ak_a(C - C_e)$, where a = 0.47 nm is the unit length of a single incorporated monomer to the protofilament length [214], and k_a is the bimolecular rate constant for the reaction between monomers and fibril tips. The rate coefficient k_a value escalates from 2.5×10^5 to 7.7×10^5 M^{-1} s^{-1} under the impact of 1 M urea (Fig. 4.3). These values are significantly slower than the expected diffusion limit for association of about 10^{10} M^{-1} s^{-1}, just as WTAβ40 fibrils [115]. It is worthwhile to notice that the k_a of E22QAβ40 is almost 14 times to that of WTAβ40. We attributed this change to the frustrated intermediate state structural modification E22Q

enforced on the peptide [155]. The central hydrophobic core is less stabilized and more exposed, forcing the peptide to favor dock onto the peptide to bury the hydrophobic region. Because of this, the free energy barrier of central hydrophobic core restructuring after binding to the fibril is lowered, leading to faster incorporation and ultimately faster growth [155, 160]. The rate constant can be written as $k_a = k_o \exp(-\Delta G^{\ddagger}/k_B T)$, where k_B is the Boltzmann constant and T is temperature. We adopt the same $k_o = 10^{10}$ M^{-1} s^{-1} for WTAβ40 as the diffusion limit. It has been found that Dutch variant and WT Aβ40 share similar diffusion limit [239]. We note that urea increases the solution viscosity by 4% at 1 M [229]. Accounting for this increase would depress the values of $G^{\ddagger}$ in the presence of urea by about 0.1 kJ mol^{-1}, which is within the experimental uncertainty of this variable (Fig. 4.3). With this, the free energy barrier $\Delta G^{\ddagger}$ decreases from 26.4 ± 0.2 kJ mol^{-1} in the absence of urea to 23.8 ± 0.2 kJ mol^{-1} at 1 M urea, that is, the barrier reduces by about 2.5 kJ mol^{-1} $(mole\ urea)^{-1}$ (Fig. 4.3E).

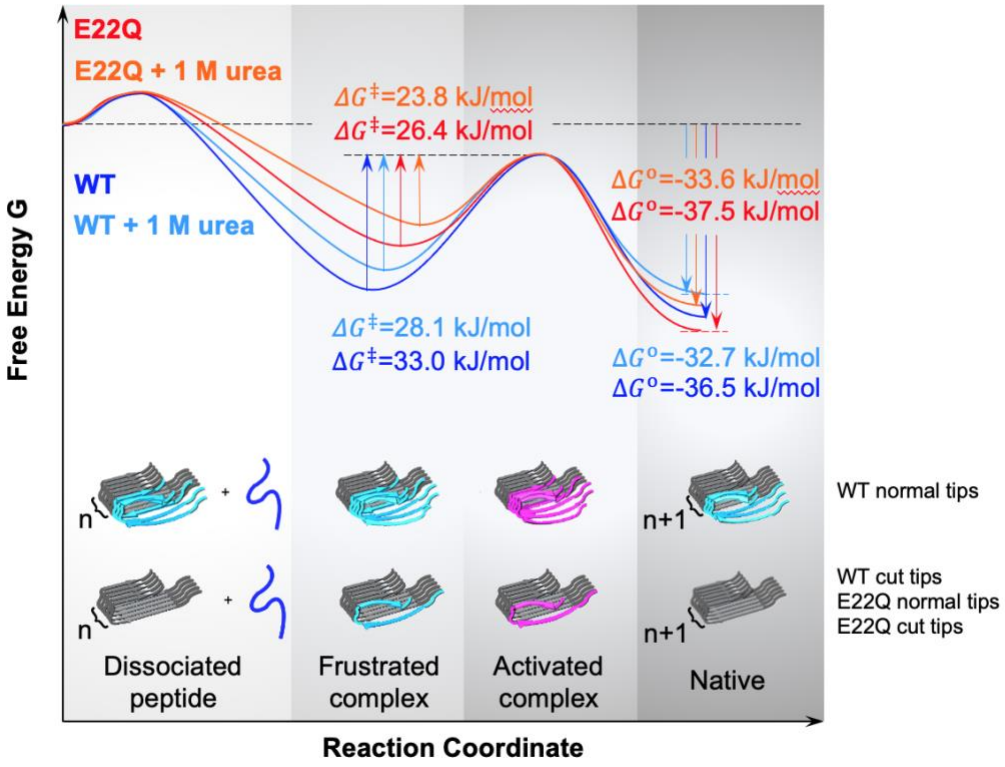

Fig. 4.3 Free Energy Landscape of Dutch and WT Aβ Fibrillization.

Figure 4.3 Schematic of free energy landscape along a pathway of incorporation of a peptide into a fibril tip that passes through a frustrated state. The cartoons are a representation of fibril tip structures at different stages.

4.4 The Modified Frustrated Complex at the Fibril Tip

The opposing activation free energy $\Delta G^{\ddagger}$ and fibrillization free energy ΔG^{o} responses to urea found in WTAβ40 lead to experimental discovery of the frustrated intermediate complex at the fibril tip in Chapter 3. We suspect that E22QAβ40 also possesses such frustrated complex, and it might be the key to its fibrillization behaviors.

We have proven in Chapter 3 that the substantial magnitude of $\Delta G^{\ddagger}$ and its sensitivity to urea together imply that the intermediate complex is bound by strong hydrophobic contacts, distinct from the native contacts that support the fibril structure and dictate ΔG^{o}. The unraveling of the initial nonnative contacts between the incoming and terminal fibril monomers, in search of the native conformation typical of the bulk fibril, becomes the rate-limiting step for the attachment of the monomer to the fibril tip and contributes to $\Delta G^{\ddagger}$. Urea, by interacting with the backbones of monomers at the fibril tip, weakens the nonnative contacts and thereby destabilizes the intermediate state, which lowers $\Delta G^{\ddagger}$ (Fig. 4.3) [230, 231]. The extent of frustration in the intermediate state can correlate to change in k_a and $\Delta G^{\ddagger}$ in response to urea. As discussed in Chapter 3. For WTAβ40, 1 M urea results in 7-fold increase in rate constant and lowers the $\Delta G^{\ddagger}$ by 4 kJ mol^{-1} (mole urea)$^{-1}$, implying extensive nonnative contacts in the intermediate state. Further analysis and simulations also showed that there might be three to four frustrated peptide chains constrained to a single protofilament. In the case of E22QAβ40, 1 M urea elicits 3-fold increase in rate constant and lowers the barrier by 2.5 kJ mol^{-1} (mole urea)$^{-1}$, indicating less frustration in the intermediate state. E22QAβ40 should carry a simpler intermediate state for fibrillization compare to WTAβ40.

We performed quantitative comparison between the urea-induced weakening of the frustrated contacts to what is studied for protein unfolding [237]. Statistics over 45 proteins have revealed that urea-induced lowering of the free energy of unfolding scales with the protein surface area exposed to solvent upon unfolding [237]. This proportionality indicates that the thermodynamic effect of urea of about 4 kJ mol^{-1} (mole of urea)$^{-1}$ is associated with the loss of about 5000 $Å^2$ of solvent accessible surface area (SASA) upon

monomer incorporation into the fibril; we designate this loss as$\Delta SASA^0 = -5000$ Å^2. The urea-induced activation free energy drop of about 2.5 kJ mol^{-1} (mole of urea)$^{-1}$ corresponds to the exposure of $\Delta SASA^{\ddagger} = 2300$ Å^2. This value corresponds to one or two monomers in the intermediate state [237]. The evaluations of $\Delta SASA^0$ and $\Delta SASA^{\ddagger}$ afford the opportunity to compare the results of the kinetics experiments to those of simulations and thus attain additional insights in the incorporation pathway. We should also bear in mind that, when comparing the fibrilization kinetics of the Dutch variant and WT Aβ40, the free energy change in response to urea of WTAβ40 is fit from 3 data points (0 M, 1 M, and 1.5 M urea) while that of E22QAβ40 is deduced from 2 data points (0 M and 1 M urea).

4.5 The Growth of Fibrils with Bulk Structure of Their Tip

To determine whether the E22QAβ40 fibril carries a simpler frustrated state than the WT Aβ40 fibril, we monitored the growth rates of freshly cut fibrils (Fig. 4.4). In freshly cut fibrils, the peptides at the tip initially should carry the structure of monomers in the fibril bulk, and an intermediate state composed of more than one frustrated chain may not have had time to evolve just as in WTAβ40. Thus, if the slow growth rate observed in the AFM experiments is due to a frustrated complex composed of several chains, freshly cut fibrils will grow faster than fibrils with normal tips. In contrast if an intermediate state consists of a simple frustrated complex, i.e., one or two such monomer as opposed to three or four in the WT Aβ40 fibrillization intermediate state, the fresh cut fibril should grow comparably fast to the normal fibril tip as it would not take significant amount time to recover from the cut.

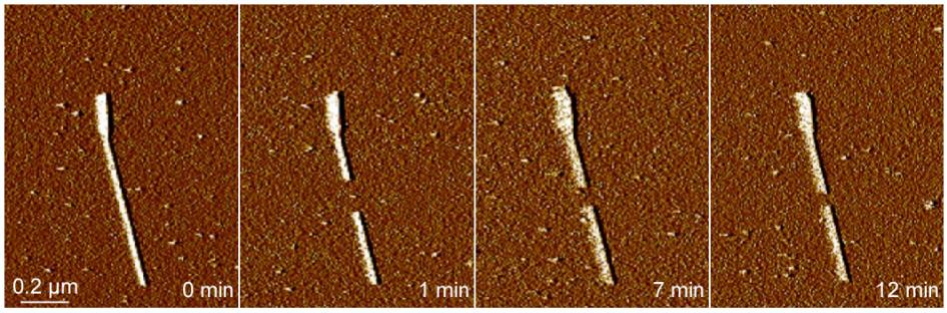

Fig. 4.4 Cut Fibril Growth Image Sequence.

Figure 4.4 A sequence of fresh cut fibril growth. The middle section was cut by reducing the AFM tip set point. After the cut, the fibril ends grow back and closes the gap.

The AFM measurements reveal that freshly cut Dutch variant fibrils grow about as fast as fibrils with equilibrated tips (Fig. 4.5). The observed similar growth rates indicate that the freshly cut fibrils carry a similar frustrated complex to the equilibrated fibril tips. As discussed, a fresh cut fibril initially carries the structure of a monomer in bulk. We can conclude that the intermediate state of Dutch variant fibrils should carry a simple frustrated complex with a structure similar to that of the fibril bulk.

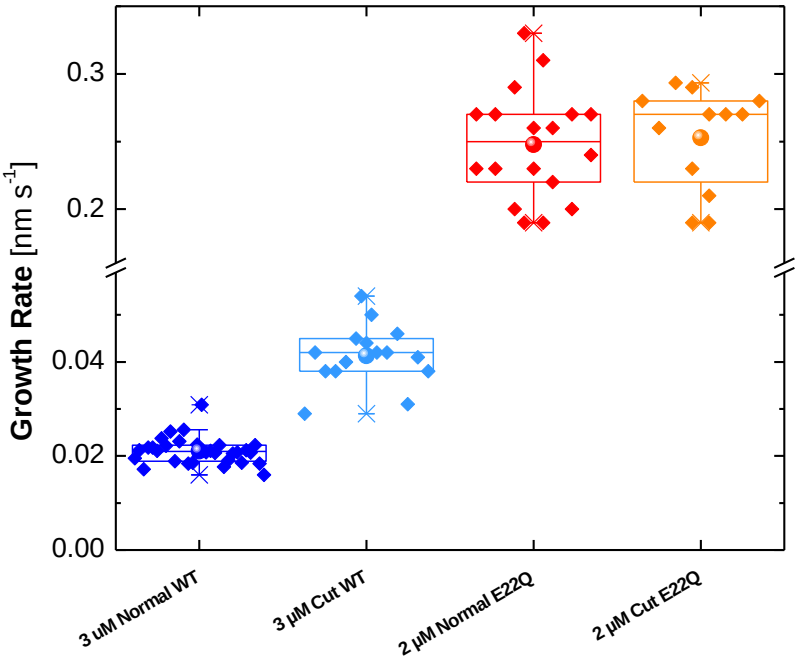

Fig. 4.5 Fibril Growth Rates Comparison between Normal and Freshly Cut Fibrils of Different Types.

Figure 4.5 Growth rate of single fibril tip represented in jitter plots. The symbol representation is the same as in Fig. 2.1.

4.6 Conclusions

Time-resolved in situ AFM measurements of the growth kinetics of individual fibrils reveals a two-step mechanism of growth of E22QAβ40 fibrils similar to that for WTAβ40, whereby an incoming monomeric solute peptide first attaches to a complex residing at the fibril tip that have nonnative conformations. The unraveling of the frustrated initial contacts during the conformational rearrangement of one of the constituent peptides to the bulk fibril structure constitute the rate-limiting step for fibril assembly. The proposed

reaction pathway should help guide the search for fibrillization inhibitors by finding small molecules that bind to the frustrated complex at the fibril tip and increase the free energy cost of rearranging it. It may also deepen the understanding of FAD, provide some perspectives for other mutations, and guide more detailed research in this area. FAD is among the easiest identifiable cases of AD due to its purely genetic nature. Our research could be insightful for further studies.

In a broader context, our findings indicate that the charge state of individual amino acid in the Aβ sequence can have a significant impact on the bend motifs, lead to changed stability of the peptide and modify the growth or the structure of frustrated intermediate state entirely. It paves the way for taking amino acid characteristics into considerations when investigating fibrillization kinetics. It might also provide an answer to why some FAD patients have extensive amyloid buildup in vasculatures: the mutated fibrils simply grow too fast.

4.7 Supplementary Results

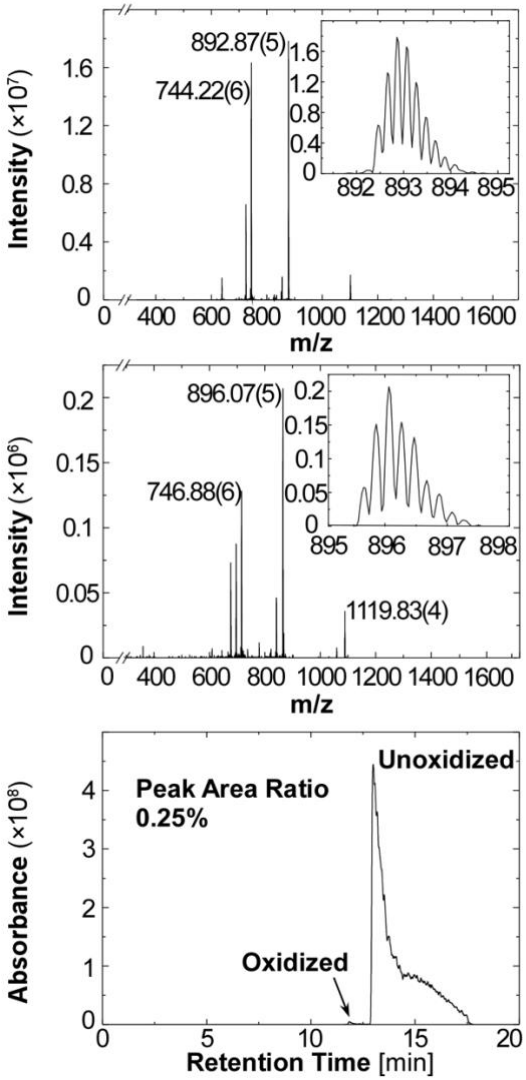

Fig. 4.6 LC-MS Characterizations of the E22QAβ(M1-40) Peptide. Top.

Figure 4.6 The mass spectrum of the unoxidized E22QAβ(M1-40) peptide. The inset shows a zoom-in of the peak at m/z 892.87 (5). m/z of major peaks is indicated. Numbers in parenthesis represents the charge carried by the molecules. **Middle.** The mass spectrum of the oxidized E22QAβ(M1-40) peptide. The inset shows a zoom-in of the peak at 896.07 (5) The mass difference between the unoxidized and the oxidized peptide is 16 g mol^{-1},

corresponding to one oxygen atom. **Bottom.** Chromatogram of the E22QAβ(M1-40) peptide sample. The fractions represented by the oxidized and the unoxidized peaks were used for the mass spectrometry. The peak area ratio between the oxidized and the unoxidized fraction is shown in the plot. The amount of oxidized peptide is insignificant.

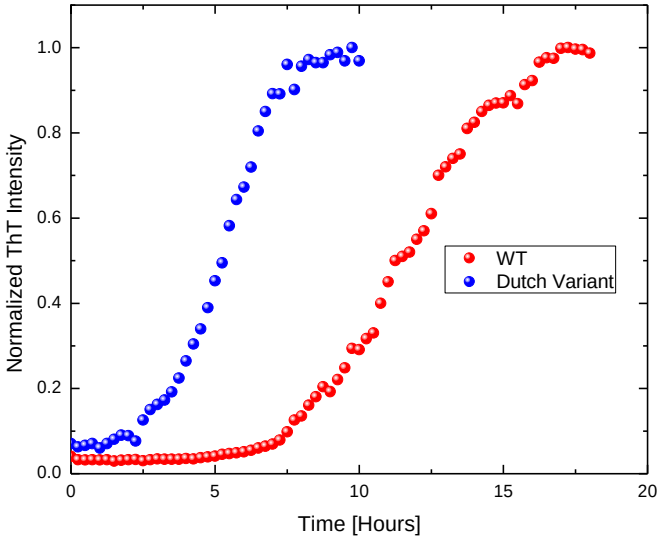

Fig. 4.7 ThT Assay of Fibril Growth.

Figure 4.7 ThT fluorescence assay of E22Q and WTAβ40 fibrillization over the period of 18 hrs. Both concentrations are 30 μM. β-sheet structure starts to appear after four hours indicated by increasing fluorescence signal. Fibril formation completes after 10-18 hrs.

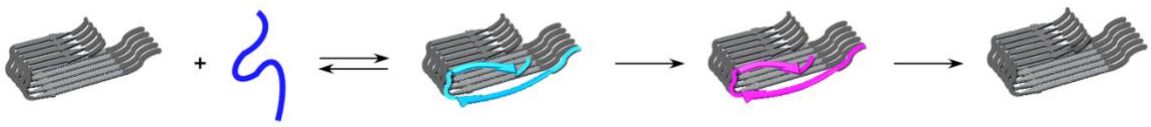

Fig. 4.8 Schematic of the Reaction Mechanism of Dutch Variant Fibril Growth.

Figure 4.8 E22QAβ40 peptides with native contacts in the fibril bulk are drawn in gray; peptides in solution and newly attached to non-native complex at fibril tip, in light blue; peptides with frustrated contacts that constitute the transition state, from which one of them attains native structure, are drawn in pink.

Chapter 5: Impacts on Amyloid-β Fibrillization Induced by Interactions with Lipid Bilayers

5.1 Backgrounds

Aβ fibrillization in the presence of lipid bilayers has received much attention for it might answer many questions as to the underlying mechanism of fibrillization in vivo. Existing studies have shown a certain level of variance regarding many important aspects, for example, whether the lipid bilayers accelerate or inhibit fibrillization, or whether the lipid bilayers bind to a certain form of Aβ[160]–[163]. To provide more perspective to the current situation and to provide a reliable method to study this topic, we employed time-resolved in situ atomic force microscopy to monitor several different scenarios of Aβ40 fibrillization. We monitored Aβ40 fibril growth on a supported lipid bilayer (SLB) of 1,2-dipalmitoyl-sn-glycero-3-phosphocholine (DPPC), the growth of Aβ40 fibril nucleated on DPPC SLB on mica, and the growth of Aβ40 fibril nucleated on DPPC SLB on DPPC SLB. Combining these observations with previous data on the growth of Aβ40 fibrils on mica surface and ThT assay and spectroscopical characterizations, we may help answer some of the most important questions. How do lipid bilayers interact with Aβ40? Do lipid bilayers induce a distinct polymorph of Aβ40 fibril? Is there a modified frustrated intermediate state in the presence of lipid bilayers?

5.2 Materials and Methods

All the procedures regarding solution preparation, Aβ expression and purification, fibril formation, and AFM sample preparation and operation are the same as those described in Chapters 2.2 and 3.2 unless specified otherwise.

Lipid Vesicle and Supported Lipid Bilayer Preparation. 1,2-dipalmitoyl-sn-glycero-3-phosphocholine (DPPC, Avanti Polar Lipids) lipid was purchased in powder form. Lipid powder was weighed as desired for a final concentration of 1.5 mM and then was dissolved in chloroform. The DPPC in chloroform solution was then subjected to nitrogen flow to evaporate the chloroform to obtain a thin lipid film on the wall of the glass vial. The vial containing DPPC thin film was then placed in a desiccator for a minimum of 12 hours to remove and remaining traces of water. Fibril incubation buffer was subsequently added to hydrate the DPPC thin film, the final lipid concentration was controlled to 1.5 mM. The lipid solution was kept under at least 45 ^{o}C with occasional shaking (phase transition temperature of DPPC is 41.3 ^{o}C) to let the thin film hydrate and form liposomes (multilamellar vesicles, MLV). When the thin film is fully dissolved in the fibril incubation buffer, forming a milky solution without any visible lipid clusters, the lipid solution was extruded on a Avanti Mini-extruder through 100 nm polycarbonate membrane for at least 20 passes until the lipid solution is clear (small unilamellar vesicles, SUV). The extrusion was done on a heat plate to keep the apparatus over the DPPC phase transition temperature. The size of the SUV was evaluate using DLS.

Supported lipid bilayer (SLB) was prepared on freshly cleaved mica surface through direct fusion. Droplets of extruded DPPC solutions were placed on the freshly cleaved mica surface and was incubated for 45 minutes under at least the DPPC phase transition temperature. After 45 minutes, allowing SUVs to fuse onto the mica surface, remaining lipid solutions on the mica surface was washed away gently using DI water. The surface must be kept moist at all times afterwards. To check SLB coverage, the mica

surface with SLB was rigorously washed by streams of DI water and was subsequently imaged using AFM.

Lipid Vesicle and Amyloid-β 40 Fibrils Interactions. Interactions between lipid vesicles and Aβ40 fibrils were monitored through ThT assay. Stock Aβ40 was adjusted to a final concentration of 30 μM using fibril incubation buffer and the DPPC SUV solution (in fibril incubation buffer) was added to make the final DPPC concentrations at 60, 150, 300, 600, and 900 μM. To monitor fibril formation, ThT was added to the DPPC/Aβ40 mixture to a final concentration of 100 μM. The ThT fluorescence was monitored at 37 °C with mixing. Measurements were taken every 15 minutes with excitation and emission at 442 nm and 488 nm, respectively, using a SpectraMax Gemini EM Microplate Reader (Molecular Devices).

To distinguish at which stage DPPC vesicles bind to Aβ40, DPPC vesicles were added at different time points based on the sigmodal curves generated from the solution of 5:1 DPPC to Aβ40 concentrations. The control group contains the same amount of Aβ40 as the experimental group, at different time points (0, 1, 2, 3, 4, and 5 hours), DPPC SUV solution was added to the experimental group to a final concentration of 150 μM and fibril incubation of the same volume was added to the control group to ensure same dilution. The amount of Aβ40 was pre-calculated so that after addition of DPPC SUV solution (fibril incubation buffer), the concentration of Aβ40 would be at 30 μM.

Stock Aβ40 and DPPC SUV interaction was also checked using a DU800 Spectrophotometer (Beckman Coulter). Extinction coefficient of DPPC was adopted as $\varepsilon = 19500\ M^{-1}\ cm^{-1}$ [240]. Spectrum of pure Aβ40 was recorded at 30 μM, followed by pure

DPPC SUV solution at 100 μM and then Aβ40 and DPPC SUV mixture at the same concentration.

Sample Preparations for AFM. Three different types of samples were prepared for imaging under AFM. To determine if DPPC SUV vesicles bind to Aβ40 fibrils, DPPC SUV and Aβ40 were mixed at 150 μM and 30 μM, respectively, and incubated on a table Inkubator 1000 (Heidolph) for 24 hours at 37 ºC. The fibril seed solution was then sonicated in a Cole Palmer bath sonicator for 10 minutes to scatter clustered fibrils. After that, 2 uL of the seed solution was mixed with fibril incubation buffer to a final volume of 1 mL and was observed under AFM using the same procedure as in Chapter 2.2. To monitor Aβ40 growth on the SLB, Aβ40 fibril seed solution was prepared as in Chapter 2.2 and was deposited on mica surface with freshly prepared SLB. AFM sample preparation and operation were the same as in Chapter 2.2. To monitor the growth of Aβ40 fibrils nucleated in the presence of SLB, stock Aβ40 was adjusted to 100 μM and droplets were placed on mica surface with freshly prepared SLB. The mica surface was then placed in a petri dish to reduce evaporation. Incubation was allowed for a minimum of two days. After incubation, the remaining liquid on the mica was blotted away from the side using kimwipes, then, the mica surface was washed using fibril incubation buffer and the buffer was collected rather than discarded. The collected mica-surface-washing fibril incubation buffer would contain Aβ40 fibrils nucleated on the SLB. The collected solution was treated the same as the Aβ40 fibril seed solution, and all subsequent fibril growth experiments under AFM followed the same procedures in Chapter 2.2.

5.3 DPPC SUV Hinders Aβ40 Fibrillization by Interacting with Oligomers and Fibrils

Aβ40 forms fibrils via self-polymerization with a characteristic sigmoidal curve (Figs. 2.11 and 4.7). The underlying mechanisms of how fibrils form and are impacted by biologically relevant environment are important for understanding of neuropathology of AD as well as therapeutics designs. We used DPPC SUV as model lipids to mimic the abundant lipid bilayer environment that is the extracellular space.

Amyloid fibrillization and polymorphism are strongly influenced by the presence of lipid bilayers [110, 212]. Emerging evidence suggests that the polymorphs that form in the presence of lipid membranes may be highly neurotoxic [120, 121]. We aim to explore the significance of the frustrated intermediate state for the growth of fibrils in interaction with lipid environment, and ThT was employed to monitor fibril growth in the presence of DPPC SUV [134, 136]. The resulting normalized data that show fibril formation as a function of time are plotted in Fig. 5.1. It appears that DPPC SUV prolongs the lag time, during which Aβ40 peptides form oligomers but not yet β-sheet stuctures, by a total factor of 2 with an increasing prolonging effect as its concentration increases from 0 to 150 μM. As the concentration of DPPC SUV increases, the growth phase of the curve, during which fibril elongation occurs, slows down. The final ThT fluorescence intensity also decreases as the concentration of DPPC SUV increases. The effect of DPPC on fibrillization in this experiment can be treated as the sole effect of DPPC SUV, rather than single DPPC molecule as all the concentrations are orders of magnitude beyond the critical micelle concentration [241].

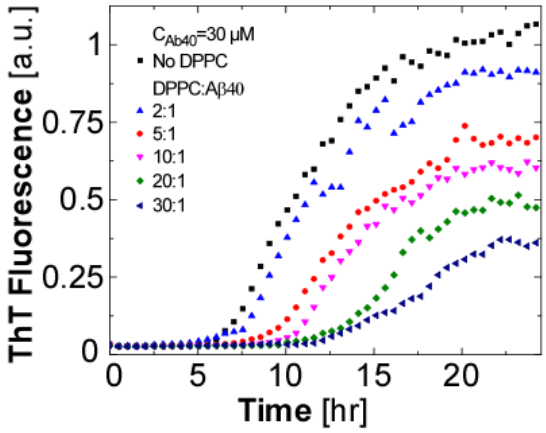

Fig. 5.1 ThT Assay of Fibril Growth in the Presence of DPPC SUV.

Figure 5.1 ThT fluorescence assay of Aβ40 fibril formation with different concentrations of DPPC SUVs over the period of 25 hours. Fibrils rich in β-sheet structure starts to appear after 5-10 hours indicated by increasing fluorescence signal. Fibril formation completes after 20 hours. Different color of curves represents different initial DPPC SUV and Aβ40 concentrations.

From the ThT curves in Fig. 5.1, we can conclude that DPPC SUVs bind to Aβ40 and impact the fibrillization pathway, yet no conclusions can be made regarding what species of Aβ40 they bind to. To distinguish this, we performed UV-vis experiments and another ThT assay with varying DPPC addition time. First, we recorded the spectra of pure Aβ40 peptide and pure DPPC SUV. The arithmetic sum of these two spectra should match the spectrum of the mixture of these two if there were no interactions. We can see that the arithmetic sum of the two pure species spectra matches the spectrum of the mixed sample without and peak shifting, amplification, or suppression, indicating that Aβ40 peptide does not interact with DPPC SUV (Fig. 5.2). This finding is consistent with earlier studies done

on Aβ42 peptide, which has striking physiochemical similarities to Aβ40 when in solution [162, 240]. It is also consistent with previous findings that Aβ peptides display weak to no binding to zwitterionic lipid membranes in neutral pH (DPPC is zwitterionic) [120, 162, 241].

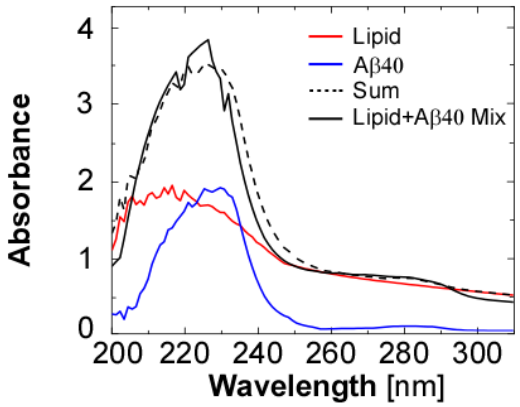

Fig. 5.2 UV-vis Spectra of DPPC SUV and Aβ40.

Figure 5.2 UV-vis spectra of Aβ40 (blue), DPPC SUV (red) and mixture of same concentrations (black). Dashed line represents arithmetic summation of the red and blue spectra. The 280 nm peak represents the Aβ40, 220-230 nm peak represents peptide bonds, 210-220 nm peak is typical of DPPC. Aβ40 samples have a concentration of 30 μM while the DPPC samples have a concentration of 90 μM. All experiments were done at consistent level of dilution.

To evaluate at which stage in the fibrillization process the DPPC SUV interferes, at each time point (Fig. 5.3), DPPC SUV solution was added to assay wells containing solutions of Aβ40 peptides and the same amount of buffer was added to the control well as

described in Chapter 5.2. When DPPC SUV was added during the lag phase at different time points (0-4 hours), the lag time was delayed by 2.5-4.5 hours. When the addition was made when ThT signal just started to spike, that is, the beginning of elongation phase, the signal continued to grow but with a slower rate than the control group and had a weaker final fluorescence intensity.

We believe that the data collected clearly show that DPPC vesicles can interfere with the fibrillization of Aβ40 peptide, and our experiments help elucidate during which stages the interferences take place. Three scenarios for how DPPC SUVs can affect the fibrillization of Aβ40 could explain the delayed lag-time and the slower elongation phase. First, the Aβ40 oligomers can aggregate at the lipid membrane surface. The process can take place in association with lipid membranes, especially the higher partitioning of Aβ to gel state lipid bilayers (DPPC with a phase transition temperature of 41.3 ^{o}C while the experiments were conducted in environments no higher than 37 ^{o}C), which effectively lower the concentration of oligomers in the bulk solution, therefore delays the lag phase [163]. Previous studies have supported the idea that Aβ has a higher binding specificity for gel phase lipid bilayers compare to liquid crystalline lipid bilayers [160, 242]. Second, we have proved in Chapters 2 and 3 that fibril growth is not a diffusion-limited reaction; however, the same cannot be concluded during the lag phase of growth in the presence of lipid bilayer. We have shown that DPPC SUV interacts with Aβ40 oligomers rather than monomers, yet unlike fibrils, oligomers are of a fluid nature and the Aβ oligomerization process could involve oligomer to oligomer association [243]. It is not the same as fibril growth, which, we modeled in Chapters 2 and 3, is by monomer addition [245]. This is particularly important in the case of Aβ oligomers association with gel phase lipid vesicles.

Aβ oligomers would be significantly more hindered in the translational diffusion in the membrane surface of DPPC SUVs, which is a solid bilayer, rather than a liquid crystalline bilayer. In such case, this might provide an explanation for the results showing DPPC SUV delays the lag time of fibrillization.

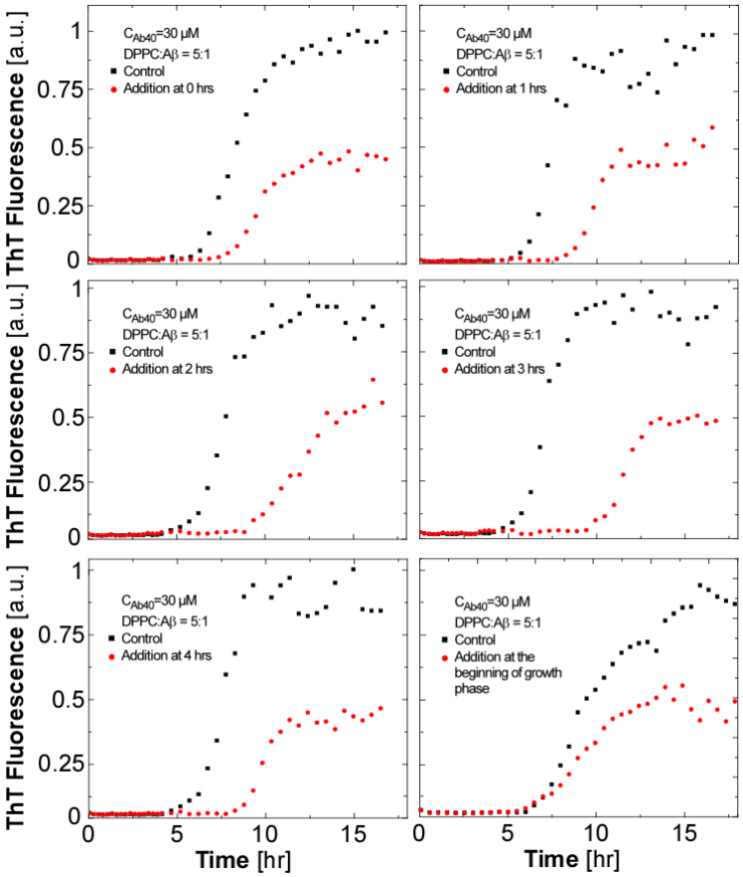

Fig. 5.3 ThT Curves of Fibril Formation with Different DPPC SUV Addition Time.

Figure 5.3 ThT curves showing fibrillization with different DPPC addition time. Control groups have addition of buffer to ensure the same dilution. Change in kinetics is purely due to addition of DPPC, rather than dilution.

The third scenario is that DPPC SUV binds to fibrils, which can be observed by the AFM directly (Fig. 5.4). The images show several Aβ fibrils a few hundred nanometers in length and the DPPC SUVs appear to attach to the fibrils in a bead on a string fashion, with varying locations on the fibrils. This is also reflected in the ThT assays. ThT binds to β-sheet structures and the signal strength is proportional to the amount of β-sheet content [134, 136]. With DPPC SUV competing for binding sites on fibrils, and possibly capping the end of fibrils which prevents further growth and accumulation of β-sheet structures, the signal during the fibril elongation phase slows down and the final ThT fluorescence intensity decreases. In addition, this finding is also consistent with a theoretical study of transferring of peptides/amino acids from lipid membranes to water (~-9 kcal/mol for Aβ40 peptide, indicating its readiness to transfer from membrane to water) [162, 244].

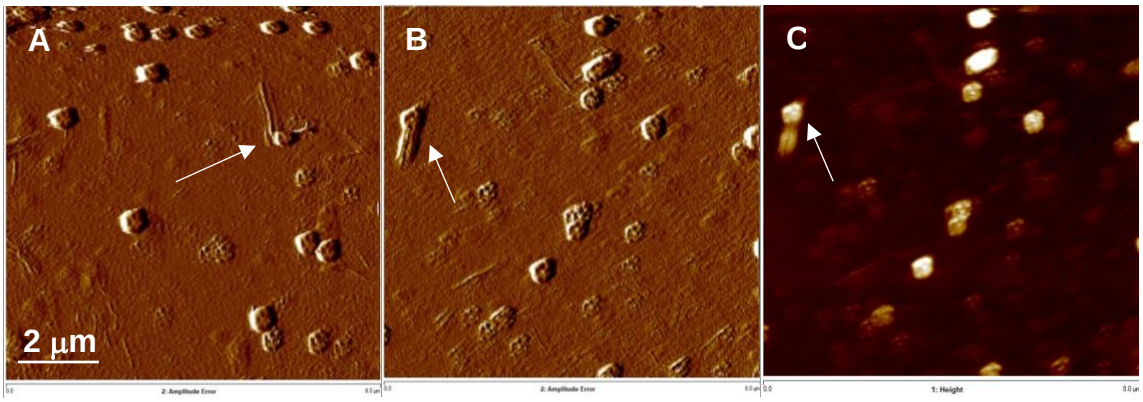

Fig. 5.4 AFM Images of DPPC SUV Binding to Aβ Fibrils.

Figure 5.4 **(A-B).** Amplitude images. White arrows point to DPPC SUV binding to Aβ fibril. **(C).** Height image of B for a clearer representation.

5.4 Aβ40 Fibrils Nucleated on DPPC SLB Assume a Different Polymorph and Grow Faster

There are three types of fibril growth we would like to explore: normal fibril growth on DPPC SLB, growth of fibrils nucleated on DPPC SLB, and growth on DPPC SLB of fibrils nucleated on DPPC SLB. Combining all these experiments, we may be able to address the following questions: (1) does lipid bilayer alter normal Aβ40 fibril growth (modifying frustrated intermediate state)? (2) does fibril nucleated on lipid bilayer have a different polymorph? (3) does Aβ40 fibril growth on lipid bilayer disrupt the lipid bilayer and do fibrils with different polymorphs affect this process differently?

Having had only limited time, the current experiments have focused on growth of fibrils nucleated on DPPC SLB. The combination with data of normal fibril growth should help answer the question: does fibril nucleated on a lipid bilayer have a different polymorph? We employed AFM to monitor the growth on mica of Aβ40 fibrils nucleated on DPPC SLB with different Aβ40 concentrations. We measured the thickness of 80 Aβ40 fibrils and plotted the distribution. In comparison to the normal Aβ40 fibrils which were nucleated in bulk, the thickness distribution is clearly different (Fig. 5.5). Overall, fibrils nucleated on the DPPC SLB are thinner and have a narrower distribution compared to normal Aβ40 fibrils. This finding is consistent with earlier studies showing that DPPC SLBs progressively accumulate Aβ40 oligomers and shorter and thinner fibrils [154]. Due to the fact that DPPC SLBs are always in the gel phase during the experiment, the lipid bilayer is tightly packed, it is mostly like that Aβ40 fibrils nucleate on the surface of DPPC SLB, interacting with DPPC head groups, instead of incorporating into the layers.

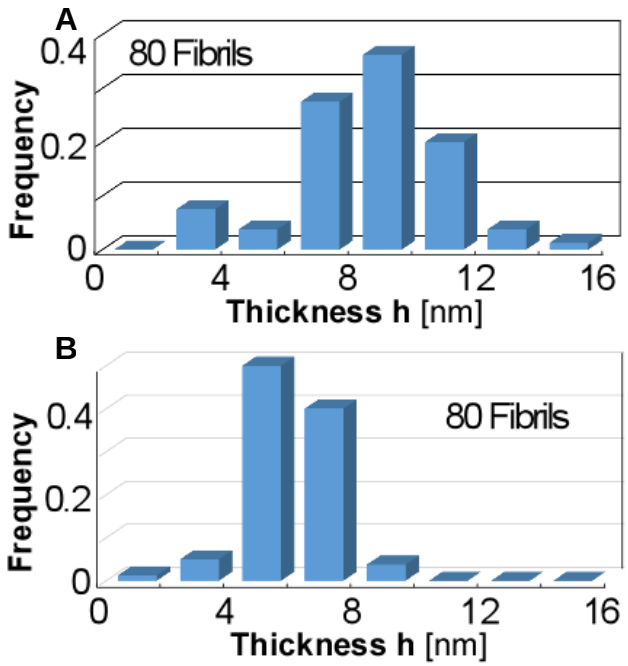

Fig. 5.5 Fibril Thickness Distributions.

Figure 5.5 **(A).** Normal Aβ40 fibrils. **(B).** Aβ40 fibrils nucleated on the DPPC SLB.

We measured the growth rate of Aβ40 fibrils nucleated on DPPC SLB, on a mica surface at 5 μM Aβ40 concentration. From the jitter plot we could see that they grow faster than the normal Aβ40 fibrils and the two ends on a single fibril grow increasingly dissimilar (Figs. 5.6, 5.7 and 2.3). All of these indicate that a different polymorph of fibril is in play and possibly an entirely different frustrated intermediate state dictating the growth of the fibril. We still need to perform more experiments to verify the polymorph and the nature of the frustrated intermediate state, but the existing literature provides some ideas for why the presence of lipid bilayers could induce a different fibril structure. In the case of lipid SUVs, because the membrane has a big curvature, Aβ has the chance to enter the water-accessible hydrophobic regions to form weak hydrophobic interactions with the lipid

bilayers, therefore polymorphism could change, as well as oligomerization and fibrillization kinetics [156, 161]. These hydrophobic interactions will likely slow down the original kinetics as we have observed; however, because monomeric Aβ40 does not interact with DPPC SUV, diffusion limit probably will not play a role in preventing fibrillization. In the case of lipid SLB, because specifically, DPPC is in gel phase and is flat, Aβ40 oligomers and fibrils will bind to the SLB with a higher affinity than to the SUV, leading to possible weaker ability to backtrack during fibrillization, therefore thinner fibrils may become dominant [154, 156].

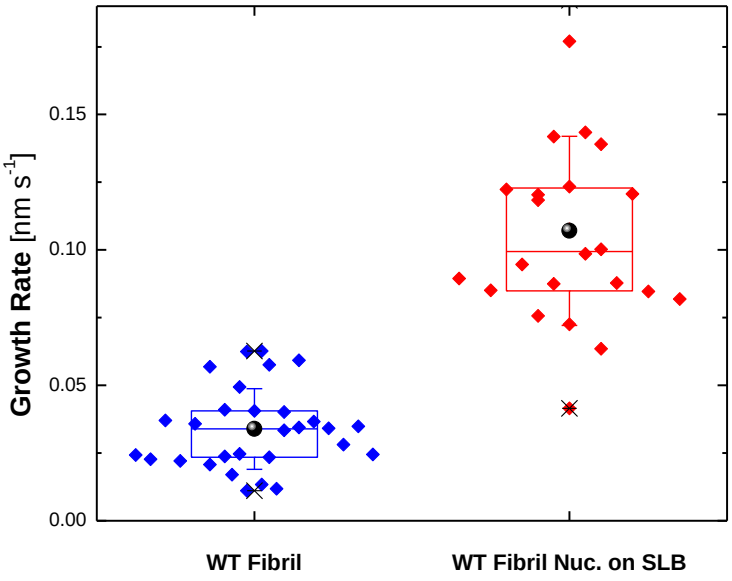

Fig. 5.6 Fibril Growth Rate Comparison.

Figure 5.6 Fibril end growth rates comparison at peptide concentration of 5 μM in jitter plots. Symbol representation is the same as in Fig. 2.1.

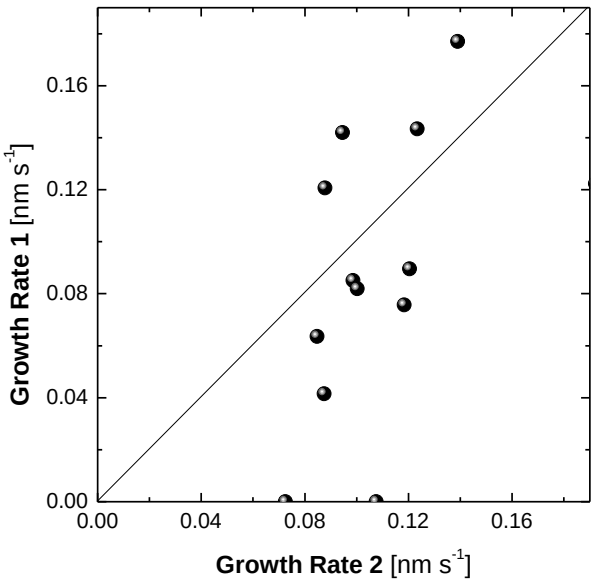

Fig. 5.7 Two Ends on a Single Fibril Growth Rate Comparison.

Figure 5.7 Correlation between rates of growth of the two fibrils ends. Solution concentration is at 5 μM.

5.5 Partial Conclusions and Future Experiments

We showed that DPPC SUV alters Aβ40 fibrillization kinetics by binding to oligomers and fibrils instead of monomers. In addition, it appears that Aβ40 fibrils nucleated on the DPPC SLB carry a different polymorphism and grow differently than do the normal Aβ40 fibrils. To find out the reason behind this, whether the phenomenon is due to different solubility or to different frustrated intermediate states, requires further experiments. Full data of growth rates of Aβ40 fibrils nucleated on DPPC SLB at different

concentrations would help answer this question. As mentioned before, there are three types of experiments to be done: (1), normal fibril growth on DPPC SLB, (2), growth of fibrils nucleated on DPPC SLB, and (3), growth on DPPC SLB of fibrils nucleated on DPPC SLB, in addition to previous experiments done on mica surface with normal fibrils, numbered as (4). To answer the question of whether Aβ40 fibrils nucleated on lipid bilayer have a different polymorph, (2) and (4) need to be combined. To answer whether lipid bilayers alter Aβ40 fibril growth (modifying the frustrated intermediate state), (1) and (4) (or (2) and (3)) need to be combined. To answer whether Aβ40 fibril growth on lipid bilayer disrupts the lipid bilayer and whether fibrils with different polymorphs affect this process differently, (1) and (3) need to be evaluated together. There could be a lot of interesting answers to be found.

Cholesterol incorporation into lipid layers could also be investigated as it effectively stabilizes phospholipid bilayers and alter the fluidity, which could have a major impact on interaction with Aβ molecules [245, 246]. This could further induce different polymorphs and different fibrillization kinetics that are of significant interest to this thesis.

5.6 Supplementary Results

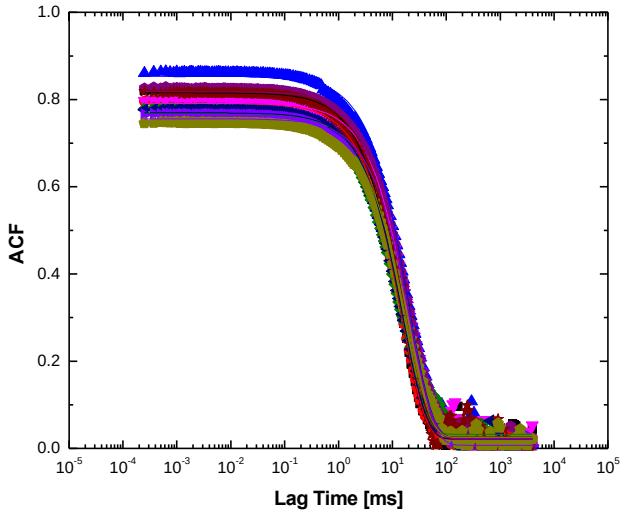

Fig. 5.8 Autocorrelation Function of Unextruded DPPC Liposomes.

Figure 5.8 Function of lag time for unextruded DPPC liposomes. All dynamic light scattering measurements were performed at a detector angle of 90°, corresponding to a scattering vector q = 18.7 μm^{-1}. Measured size is 2.5 μm.

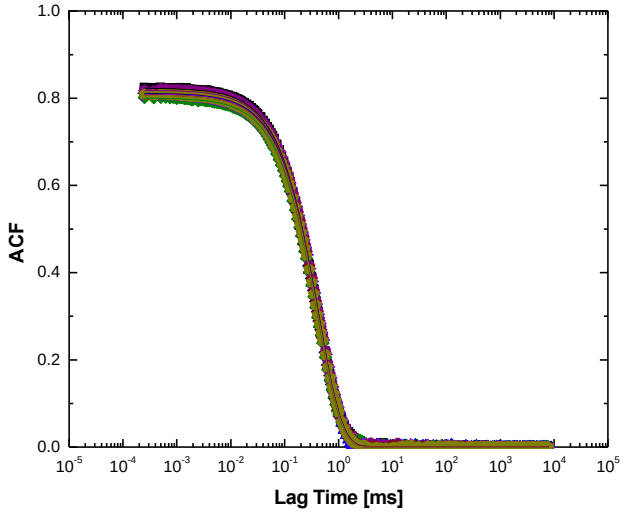

Fig. 5.9 Autocorrelation Function of Extruded DPPC Liposomes.

Figure 5.9 Function of lag time for extruded DPPC liposomes. All dynamic light scattering measurements were performed at a detector angle of 90°, corresponding to a scattering vector q = 18.7 μm^{-1}. Measured size is 70 μm.

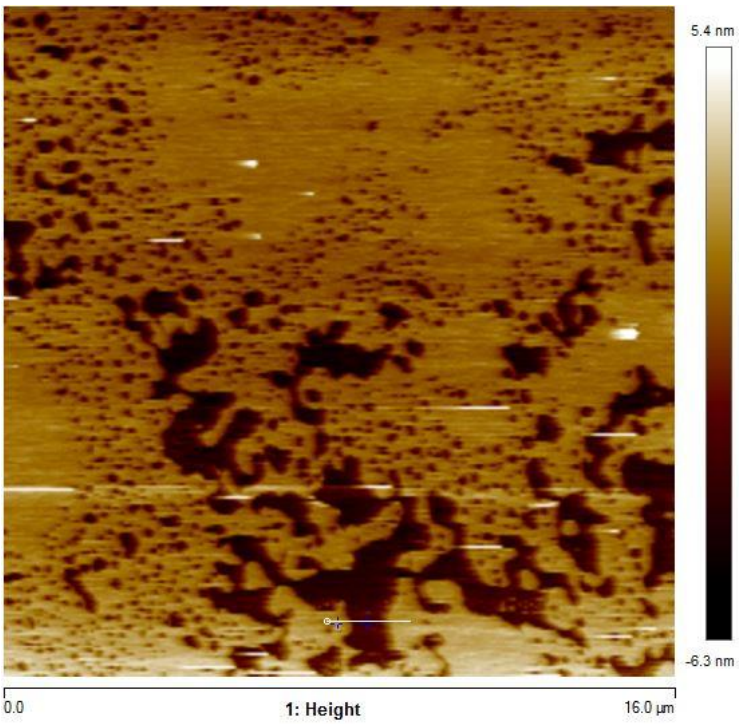

Fig. 5.10 AFM Height Image of Complete DPPC SLB Coverage with Holes.

Figure 5.10 Mica surface with complete DPPC SLB coverage. Holes were created by vigorous wash of DI water. Holes are 5 nm in depth, typical of DPPC bilayer thickness.

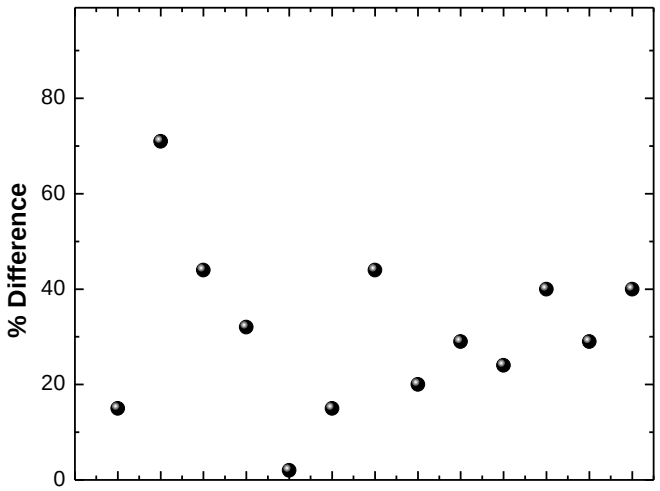

Fig. 5.11 Magnitude of the Relative Discrepancy between the Growth Rates of the Two Fibril Ends in Fig. 5.7.

Figure 5.11 In comparison to Fig. 2.3H, representing the normal Aβ fibrils, the discrepancies from fibrils nucleated on DPPC SLB are larger.

References

[1] P. D. Sun, C. E. Foster, and J. C. Boyington, "Overview of Protein Structural and Functional Folds," *Current Protocols in Protein Science*, vol. 35, no. 1. pp. 17.1.1-17.1.189, 2004. doi: 10.1002/0471140864.ps1701s35.

[2] J. Z. Zaretsky and D. H. Wreschner, "Protein Multifunctionality: Principles and Mechanisms," *Translational Oncogenomics*, vol. 3, pp. 99–136, 2008.

[3] P. E. Wright and H. J. Dyson, "Intrinsically Unstructured Proteins: Re-assessing the Protein Structure-Function Paradigm," *Journal of Molecular Biology*, vol. 293, no. 2, pp. 321–331, 1999, [Online]. Available: http://www.idealibrary.com

[4] P. Tompa, "Intrisically Unstructured Protein," *Trends in Biochemical Sciences*, vol. 27, no. 10, pp. 527–533, 2002.

[5] R. P. Joosten, "X-ray Structure Re-refinement: Combining Old Data with New Methods for Better Structural Bioinformatics," 2010.

[6] H. Deng, Y. Jia, and Y. Zhang, "Protein Structure Prediction," *International Journal of Modern Physics B*, vol. 32, no. 18, Jul. 2018, doi: 10.1142/S021797921840009X.

[7] I. Rehman, M. Farooq, and S. Botelho, *Biochemistry, Secondary Protein Structure*. 2017.

[8] A. B. Reiss, H. A. Arain, M. M. Stecker, N. M. Siegart, and L. J. Kasselman, "Amyloid Toxicity in Alzheimer's Disease," *Reviews in the Neurosciences*, vol. 29, no. 6, pp. 613–627, Feb. 2018, doi: 10.1515/revneuro-2017-0063.

[9] K. E. Badior and J. R. Casey, “Molecular Mechanism for the Red Blood Cell Senescence Clock,” *IUBMB Life*, vol. 70, no. 1, pp. 32–40, Jan. 2018, doi: 10.1002/iub.1703.

[10] A. B. Snyder, M. Zhou, R. Theodore, M. O. Quarmyne, J. Eckman, and P. A. Lane, “Improving an Administrative Case Definition for Longitudinal Surveillance of Sickle Cell Disease,” *Public Health Reports*, vol. 134, no. 3, pp. 274–281, May 2019, doi: 10.1177/0033354919839072.

[11] I. Rehman, C. C. Kerndt, and S. Botelho, *Biochemistry, Tertiary Protein Structure*. 2017.

[12] J. S. Richardson, “The Anatomy and Taxonomy of Protein Structure,” *Advances in Protein Chemistry*, vol. 34, pp. 169–339, 1981.

[13] W. Wriggers, S. Chakravarty, and P. A. Jennings, “Control of Protein Functional Dynamics by Peptide Linkers,” *Biopolymers - Peptide Science Section*, vol. 80, no. 6. pp. 736–746, 2005. doi: 10.1002/bip.20291.

[14] E. Santonico, L. Castagnoli, and G. Cesareni, “Methods to Reveal Domain Networks,” *Drug Discovery Today*, vol. 10, no. 16. pp. 1111–1117, Aug. 15, 2005. doi: 10.1016/S1359-6446(05)03513-0.

[15] S. W. Englander and L. Mayne, “The Nature of Protein Folding Pathways,” *Proceedings of the National Academy of Sciences*, vol. 111, no. 45, pp. 15873–15880, Nov. 2014, doi: 10.1073/pnas.1411798111.

[16] C. B. Anfinsen, E. Haber, M. Selajf, and F. H. White, “The Kinetics of Formation of Native Ribonuclease during Oxidation of the Reduced Polypeptide Chain,” *Proceedings of the National Academy of Science*, vol. 47, no. 9, 1961.

[17] K. A. Dill, S. B. Ozkan, M. Scott Shell, and T. R. Weikl, “The Protein Folding Problem,” *Annual Reviews of Biophysics*, vol. 37, pp. 289–316, 2008.

[18] C. Levinthal, “How to Fold Graciously,” *Mossbauer Spectroscopy in Biological Systems*, vol. 67, pp. 22–24, 1967.

[19] C. Levinthal, “Are There Pathways for Protein Folding?,” *Journal de Chimie Physique*, vol. 65, pp. 44–45, 1968.

[20] C. B. Anfinse, “Principles that Govern the Folding of Protein Chains,” *Science*, vol. 181, no. 4096, pp. 223–230, 1973.

[21] E. Habert, A. Christiax, and B. Anfinsen, “Side-chain Interactions Governing the Pairing of Half-cystine Residues in Ribonuclease*,” *TIIE JOURNAL OF BIOLOGICAL CHEMISTRY*, vol. 237, no. 6, 1962.

[22] P. G. Wolynes, J. N. Onuchic, and D. Thirumalai, “Navigating the Folding Routes,” *Science-AAAS-Weekly Paper*, vol. 267, no. 5204, pp. 1619–1620, 1995.

[23] J. D. Bryngelson, J. Nelson Onuchic, N. D. Socci, and P. G. Wolynes, “Funnels, Pathways, and the Energy Landscape of Protein Folding: A Synthesis,” *Proteins: Structure, Function, and Bioinformatincs*, vol. 21, no. 3, pp. 167–195, 1995.

[24] K. A. Dill and H. S. Chan, “From Levinthal to Pathways to Funnels,” *Nature Structual Biology*, vol. 4, no. 1, pp. 10–19, 1997, [Online]. Available: http://www.nature.com/nsmb

[25] A. Sali, E. Shakhnovlch, and M. Karplus, “How does a Protein Fold?,” *Nature*, vol. 369, pp. 248–251, 1994.

[26] C. M. Dobson, “Principles of Protein Folding, Misfolding and Aggregation,” *Seminars in Cell & Developmental Biology*, vol. 15, no. 1, pp. 3–16, 2004.

[27] K. A. Dill, “Polymer Principles and Protein Folding,” *Protein Science*, vol. 8, no. 6, pp. 1166–1180, 1999.

[28] P. E. Leopold, M. Montal, and J. N. Onuchic, “Protein Folding Funnels: A Kinetic Approach to the Sequence-structure Relationship,” *Biophysics*, vol. 89, pp. 8721–8725, 1992.

[29] M. Oliveberg and P. G. Wolynes, “The Experimental Survey of Protein-folding Energy Landscapes,” *Quarterly Reviews of Biophysics*, vol. 38, no. 3, pp. 245–288, Aug. 2005, doi: 10.1017/S0033583506004185.

[30] P. G. Wolynes’, Z. Luthey-Schultenl, and J. N. Onuchic, “Fast-folding Experiments and the Topography of Protein Folding Energy Landscapes,” *Chemistry & Biology*, vol. 3, pp. 425–432, 1996.

[31] J. N. Onuchic, H. Nymeyer, A. E. Garcia, J. Chahine, and N. D. Socci, “The Energy Landscape Theory of Protein Folding: Insights into Folding Mechanisms and Scenarios,” *Advances in Protein Chemistry*, vol. 53, pp. 87–152, 2000.

[32] J. N. Onuchic, Z. Luthey-Schulten, and P. G. Wolynes, “Theory of Protein Folding: The Energy Landscape Perspective,” *Annual Review of Physical Chemistry*, vol. 48, no. 1, pp. 545–600, 1997.

[33] T. E. Creighton, “Protein Folding,” *Biochem. J*, vol. 270, pp. 1–16, 1990.

[34] R. Zwanzig, A. Szabo, and B. Bagchi, “Levinthal’s Paradox,” *Proc. Natl. Acad. Sci. USA*, vol. 89, pp. 20–22, 1992.

[35] R. L. Baldwin and B. H. Zimm, “Are denatured proteins ever random coils?,” *Proceedings of the National Academy of Sciences*, vol. 97, no. 23, pp. 12391–12392, 2000, [Online]. Available: www.pnas.org

[36] J.-S. Hu and A. Bax, “Measurement of Three-Bond 13 C-13 C J Couplings between Carbonyl and Carbonyl/Carboxyl Carbons in Isotopically Enriched Proteins,” *Journal of the American Chemical Society*, vol. 118, no. 34, pp. 8170–8171, 1996, [Online]. Available: https://pubs.acs.org/sharingguidelines

[37] C. Tanford, “Protein Denaturation,” *Advances in Protein Chemistry*, vol. 23, pp. 121–282, 1968.

[38] Y. V. Griko, P. L. Privalov, S. Y. Venyaminov, and V. P. Kutyshenko, “Thermodynamics Study of the Apomyoglobin Structure,” *Journal of Molecular Biology*, vol. 202, no. 1, pp. 127–138, 1988.

[39] P. L. Privalov, E. I. Tiktopulo, S. Y. Venyaminov, Y. v. Griko, G. I. Makhatadze, and N. N. Khechinashvili, “Heat Capacity and Conformation of Proteins in the Denatured State,” *Journal of Molecular Biology*, vol. 205, no. 4, pp. 737–750, Feb. 1989, doi: 10.1016/0022-2836(89)90318-5.

[40] O. W. Howarth and L. Y. Lian, “Ribonuclease A: Carbon-13 Nuclear Magnetic Resonance Assignments, Binding Sites, and Conformational Flexibility1,” *Biochemistry*, vol. 23, pp. 3515–3521, 1984, [Online]. Available: https://pubs.acs.org/sharingguidelines

[41] C. M. Dobson, P. A. Evans, and K. L. Williamson, “Proton NMR Studies of Denatured Lysozyme,” *FEBS Letters*, vol. 168, no. 2, pp. 331–334, 1984.

[42] P. L. Privalov, “Stability of Proteins Smaill Globular Proteins,” *Advances in Protein Chemistry*, vol. 33, pp. 167–241, 1979.

[43] Wikimedia Commons Contributors, “File: ACBP MSM from Folding@home.tiff,” *Wikimedia Commons, the Free Media Repository*, Sep. 08, 2021.

[44] K. Kuwajima, “The Molten Globule State as a Clue for Understanding the Folding and Cooperativity of Globular-Protein Structure,” *PROTEINS: Structure, Function, and Genetics*, vol. 6, pp. 87–103, 1989.

[45] O. B. Ptitsyn, “Protein Folding: Hypotheses and Experiments,” *Journal of Protein Chemistry*, vol. 6, no. 4, 1987.

[46] K. S. Vassilenko and V. N. Uversky, “Native-like Secondary Structure of Molten Globules,” *Biochimica et Biophysica Acta - Protein Structure and molecular Enzymology*, vol. 1594, no. 1, pp. 168–177, 2002, [Online]. Available: www.bba-direct.com

[47] F. Edwin, Y. Valkya Sharma, and M. v. Jagannadham, “Stabilization of Molten Gobule State of Papain by Urea,” *Biochemical and Biophysical Research Communications*, vol. 290, no. 5, pp. 1441–1446, 2002, doi: 10.1006/bbrc.2002.6368.

[48] J. Chamani, A. A. Moosavi-Movahedi, A. A. Saboury, M. Gharanfoli, and G. H. Hakimelahi, “Calorimetric Indication of the Molten globule-like State of Cytochrome c Induced by n-alkyl Sulfates at Low Concentrations,” *J. Chem. Thermodynamics*, vol. 35, pp. 199–207, 2003, [Online]. Available: www.elsevier.com/locate/jct

[49] P. Kumar and U. Mina, *Life Sciences*, 6th ed. New Delhi: Pathfinder Publication, 2018.

[50] K. Wiithrich, “Protein Structure Determination in Solution by NMR Spectroscopy,” *THE JOURNAL. OF BIOLOGICAL CHEMISTRY*, vol. 265, no. 36, pp. 22059–22062, 1990.

[51] M. S. Smyth and J. H. J. Martin, “Review X Ray Crystallography,” *J Clin Pathol: Mol Pathol*, vol. 53, pp. 8–14, 2000.

[52] R. Zhou, X. Huang, C. J. Margulis, and B. J. Berne, “Hydrophobic Collapse in Multidomain Protein Folding,” *Science*, vol. 305, no. 5690, pp. 1605–1609, 2004.

[53] L. J. Lapidus, S. Yao, K. S. McGarrity, D. E. Hertzog, E. Tubman, and O. Bakajiny, “Protein Hydrophobic Collapse and Early Folding Steps Observed in a Microfluidic Mixer,” *Biophysical Journal*, vol. 93, no. 1, pp. 218–224, 2007, doi: 10.1529/biophysj.106.103077.

[54] S. Govindarajan and R. A. Goldstein, “On the Thermodynamic Hypothesis of Protein Folding,” *Proceedings of the National Academy of Sciences*, vol. 95, no. 10, pp. 5545–5549, 1998, [Online]. Available: www.pnas.org.

[55] C. Tanford, “The Hydrophobic Effect and the Organization of Living Matter,” *Science*, vol. 200, no. 4345, pp. 1012–1018, 1978.

[56] P. J. Guyett and L. M. Gloss, “3.4 Intermediates in Protein Folding,” *Comprehensive Biophysics*, vol. 3, pp. 43–71, Jan. 2012, doi: 10.1016/B978-0-12-374920-8.00304-0.

[57] R. L. Baldwin and G. D. Rose, “How the Hydrophobic Factor Drives Protein Folding,” *Proceedings of the National Academy of Sciences of the United States of America*, vol. 113, no. 44, pp. 12462–12466, Nov. 2016, doi: 10.1073/pnas.1610541113.

[58] C. M. Dobson, “Protein Misfolding, Evolution and Disease,” *Trends in Biochemical Sciences*, vol. 24, no. 9, pp. 329–332, 1999.

[59] F. U. Hartl, A. Bracher, and M. Hayer-Hartl, “Molecular Chaperones in Protein Folding and Proteostasis,” *Nature*, vol. 475, no. 7356, pp. 324–332, Jul. 2011, doi: 10.1038/nature10317.

[60] J. S. Valastyan and S. Lindquist, “Mechanisms of Protein-folding Disease at a Glance,” *Disease Models & Mechanisms*, vol. 7, no. 1, pp. 9–14, 2014, doi: 10.1242/dmm.013474.

[61] M. H. Smith, H. L. Ploegh, and J. S. Weissman, “Road to Ruin: Targeting Proteins for Degradation in the Endoplasmic Reticulum,” *Proc. Natl. Acad. Sci. U.S.A*, vol. 333, p. 44, 2011, doi: 10.1126/science.1209126.

[62] N. B. Nedelsky, P. K. Todd, and J. P. Taylor, “Autophagy and the Ubiquitin-proteasome System: Collaborators in Neuroprotection,” *Biochimica et Biophysica Acta (BBA) - Molecular Basis of Disease*, vol. 1782, no. 12, pp. 691–699, Dec. 2008, doi: 10.1016/J.BBADIS.2008.10.002.

[63] E. A. Greenbaum, C. L. Graves, A. J. Mishizen-Eberz, M. A. Lupoli, D. R. Lynch, S. W. Englander, P. H. Axelsen, and B. I. Giasson, “The E46K Mutation in α-synuclein Increases Amyloid Fibril Formation,” *Journal of Biological Chemistry*, vol. 280, no. 9, pp. 7800–7807, Mar. 2005, doi: 10.1074/jbc.M411638200.

[64] S. Tsubuki, Y. Takaki, and T. C. Saido, “Dutch, Flemish, Italian, and Arctic Mutations of APP and Resistance of A-beta to Physiologically Relevant Proteolytic Degradation,” *THE LANCET*, vol. 361, no. 9373, pp. 1957–1958, 2003, [Online]. Available: www.thelancet.com

[65] A. I. Azuaga, C. M. Dobson, P. L. Mateo, and F. Conejero-Lara, “Unfolding and Aggregation during the Thermal Denaturation of Streptokinase,” *European*

Journal of Biochemistry, vol. 269, no. 16, pp. 4121–4133, 2002, doi: 10.1046/j.1432-1033.2002.03107.x.

[66] F. G. de Felice, M. N. N. Vieira, M. N. L. Meirelles, L. A. Morozova-Roche, C. M. Dobson, and S. T. Ferreira, "Formation of Amyloid Aggregates from Human Lysozyme and Its Disease-associated Variants Using Hydrostatic Pressure," *The FASEB Journal*, vol. 18, no. 10, pp. 1099–1101, Jul. 2004, doi: 10.1096/fj.03-1072fje.

[67] K. Giri, N. P. Bhattacharyya, and S. Basak, "pH-Dependent Self-Assembly of Polyalanine Peptides," *Biophysical Journal*, vol. 92, no. 1, pp. 293–302, Jan. 2007, doi: 10.1529/BIOPHYSJ.106.091769.

[68] E. Herczenik and M. F. B. G. Gebbink, "Molecular and Cellular Aspects of Protein Misfolding and Disease," *The FASEB Journal*, vol. 22, no. 7, pp. 2115–2133, Jul. 2008, doi: 10.1096/fj.07-099671.

[69] B. Caughey and P. T. Landbury Jr., "Protofibrils, Pores, Fibrils and Neurodegeneration: Separating the Responsible Protein Aggregates from the Innocent Bystanders," *Annual Review of Neuroscience*, vol. 26, no. 1, pp. 267–298, 2003.

[70] D. F. Jarosz, M. Taipale, and S. Lindquist, "Protein Homeostasis and the Phenotypic Menifestation of Genetic Diversity: Principles and Mechanisms," *Annual Review of Genetics*, vol. 44, pp. 189–216, 2010.

[71] T. Hidvegi, B. Z. Schmidt, P. Hale, and D. H. Perlmutter, "Accumulation of Mutant α1-antitrypsin Z in the Endoplasmic Reticulum Activities Caspases-4 and -12, NFκB, and BAP31 but not the Unfolded Protein Response," *Journal of*

Biological Chemistry, vol. 280, no. 47, pp. 39002–39015, Nov. 2005, doi: 10.1074/jbc.M508652200.

[72] J. C. Chamcheu, G. S. Wood, I. A. Siddiqui, D. N. Syed, V. M. Adhami, J. M. Teng, and H. Mukhtar, "Progress towards Genetic and Pharmacological Therapies for Keratin Genodermatoses: Current Perspective and Future Promise," *Experimental Dermatology*, vol. 21, no. 7, pp. 481–489, Jul. 2012, doi: 10.1111/j.1600-0625.2012.01534.x.

[73] A. H. Futerman and G. van Meer, "The Cell Biology of Lysosomal Storage Disorders," *Nature Reviews Molecular Cell Biology*, vol. 5, no. 7, pp. 554–565, Jul. 2004, doi: 10.1038/nrm1423.

[74] Alzheimer's News Today, "Alzheimer's Disease Statistics," *https://alzheimersnewstoday.com/alzheimers-disease-statistics/*, 2021.

[75] Alzheimer's Association, "Alzheimer's and Dementia Facts and Figures," *https://www.alz.org/alzheimers-dementia/facts-figures*, 2021.

[76] R. Brookmeyer, E. Johnson, K. Ziegler-Graham, and M. H. Arrighi, "Forecasting the Global Burden of Alzheimer's Disease," *Alzheimer's & Dimentia*, vol. 3, no. 3, pp. 186–191, 2007.

[77] A. Serrano-Pozo, M. P. Frosch, E. Masliah, and B. T. Hyman, "Neuropathological Alterations in Alzheimer Disease," *Cold Spring Harbor Perspectives in Medicine*, vol. 1, no. 1, Sep. 2011, doi: 10.1101/cshperspect.a006189.

[78] N. Bogdanovic, "The Challenges of Diagnosis in Alzheimer's Disease," *US Neurology*, vol. 14, no. 1, pp. 15–16, Mar. 2018, doi: 10.17925/usn.2018.14.1.15.

[79] E. Karran and J. Hardy, “Antiamyloid Therapy for Alzheimer’s Disease-Are We on the Right Road?,” *The New England Journal of Medicine*, vol. 23, pp. 377–378, 2014, doi: 10.1056/NEJMe1313943.

[80] J. K. Lui, S. M. Laws, Q. X. Li, V. L. Villemagne, D. Ames, B. Brown, A. I. Bush, K. de Ruyck, J. Dromey, K. A. Ellis, N. G. Faux, J. Foster, C. Fowler, V. Gupta, P. Hudson, K. Laughton, C. L. Masters, K. Pertile, A. Rembach, “Plasma Amyloid-β as a Biomarker in Alzheimer’s Disease: The AIBL Study of Aging,” *Journal of Alzheimer’s Disease*, vol. 20, no. 4, pp. 1233–1242, 2010, doi: 10.3233/JAD-2010-090249.

[81] J. Liu, I. Costantino, N. Venugopalan, R. F. Fischetti, B. T. Hyman, M. P. Frosch, T. Gomez-Isla, and L. Makowski, “Amyloid Structure Exhibits Polymorphism on Multiple Length Scales in Human Brain Tissue,” *Scientific Reports*, vol. 6, Sep. 2016, doi: 10.1038/srep33079.

[82] C. A. Mathis, Y. Wang, and W. E. Klunk, “Imaging beta-amyloid Plaques and Neurofibrillary Tangles in the Aging Human Brain,” *Current Pharmaceutical Desgin*, vol. 10, no. 13, pp. 1469–1492, 2004.

[83] R. J. O’brien and P. C. Wong, “Amyloid Precursor Protein Processing and Alzheimer’s Disease,” *Annual Review of Neuroscience*, vol. 34, pp. 185–204, 2011, doi: 10.1146/annurev-neuro-061010-113613.

[84] R. D. Moir, R. Lathe, and R. E. Tanzi, “The Antimicrobial Protection Hypothesis of Alzheimer’s Disease,” *Alzheimer’s & Dementia*, vol. 14, no. 12, pp. 1602–1614, 2018.

[85] J. A. Duce, A. Tsatsanis, M. A. Cater, S. A. James, E. Robb, K. Wikhe, S. L. Leong, K. Perez, T. Johanssen, M. A. Greenough, H. H. Cho, D. Galatis, R. D. Moir, C. L. Masters, C. McLean, R. E. Tanzi, R. Cappai, K. J. Barnham, G. D. Ciccotosto, "Iron-Export Ferroxidase Activity of β-Amyloid Precursor Protein is Inhibited by Zinc in Alzheimer's Disease," *Cell*, vol. 142, no. 6, pp. 857–867, 2010, doi: 10.1016/j.cell.2010.08.014.

[86] C. Priller, T. Bauer, G. Mitteregger, B. Krebs, H. A. Kretzschmar, and J. Herms, "Synapse Formation and Function is Modulated by the Amyloid Precursor Protein," *The Journal of Neuroscience*, vol. 26, no. 27, pp. 7212–7221, 2006, doi: 10.1523/JNEUROSCI.1450-06.2006.

[87] U. C. Müller and H. Zheng, "Physiological Functions of APP Family Proteins," *Cold Spring Harbor Perspectives in Medicine*, vol. 2, no. 2, 2012, doi: 10.1101/cshperspect.a006288.

[88] S. Wegge and D. Beher, "Molecular Consequences of Amyloid Precursor Protein and Presenilin Mutations Causing Autosomal-dominant Alzheimer's Disease," *Alzhiemer's Research & Therapy*, vol. 4, no. 1, pp. 1–14, 2012.

[89] S. A. Gravina, L. Ho, C. B. Eckman, K. E. Long, L. Otvos, L. H. Younkin, N. Suzuki, and S. G. Younkin, "Amyloid β protein (Aβ) in Alzheimer's disease brain. Biochemical and immunocytochemical analysis with antibodies specific for forms ending at Aβ40 or Aβ42(43)," *Journal of Biological Chemistry*, vol. 270, no. 13, pp. 7013–7016, 1995, doi: 10.1074/jbc.270.13.7013.

[90] T. Iwatsubo, A. Odaka, N. Suzuki, H. Mizusawa, N. Nukina, and Y. Ihara, "Visualization of Aβ42(43) and Aβ40 in senile plaques with end-specific Aβ

monoclonals: Evidence that an initially deposited species is Aβ42(43)," *Neuron*, vol. 13, no. 1, pp. 45–53, Jul. 1994, doi: 10.1016/0896-6273(94)90458-8.

[91] R.-W. Shin, K. Ogino, A. Kondo, T. C. Saido, J. Q. Trojanowski, T. Kitamoto, and J. Tateishi, "Amyloid-Protein 1-40 but Not 1-42 Contributes to the Experimental Formation of Alzheimer Disease Amyloid Fibrils in Rat Brain," *Journal of Neuroscience*, vol. 17, no. 21, pp. 8187–8193, 1997.

[92] C. Haass and D. J. Selkoe, "Soluble Protein Oligomers in Neurodegeneration: Lessons from the Alzheimer's Amyloid β-peptide," *Nature Reviews Molecular Cell Biology*, vol. 8, no. 2, pp. 101–112, Feb. 2007, doi: 10.1038/nrm2101.

[93] J. Brenfer, "Abeta 2lfm," *Wikimedia*, Jan. 27, 2012.

[94] B. A. Willis, K. Sundell, D. R. Lachno, L. R. Ferguson-Sells, M. G. Case, K. Holdridge, R. B. Demattos, J. Raskin, E. R. Siemers, and R. A. Dean, "Central Pharmacodynamic Activity of Solanezumab in Mild Alzheimer's Disease Dementia," *Alzheimer's & Dimentia: Translational Research & Clinical Interventions*, vol. 4, pp. 652–660, 2018, doi: 10.1016/j.trci.2018.10.001.

[95] J. Kim, L. Onstead, S. Randle, R. Price, L. Smithson, C. Zwizinski, D. W. Dickson, T. Golde, and E. McGowan, "Aβ40 Inhibits Amyloid Deposition in vivo," *Journal of Neuroscience*, vol. 27, no. 3, pp. 627–633, Jan. 2007, doi: 10.1523/JNEUROSCI.4849-06.2007.

[96] P. Edison, H. A. Archer, R. Hinz, A. Hammers, N. Pavese, Y. F. Tai, G. Hotton, D. Cutler, N. Fox, A. Kennedy, and M. M. D. D. Rossor, "Amyloid, Hypometabolism, and Cognition in Alzheimer Disease: an [11C] PIB and [18F] FDG PET Study," *Neurology*, vol. 68, no. 7, pp. 501–518, 2007.

[97] Y. Li, J. O. Rinne, L. Mosconi, E. Pirraglia, H. Rusinek, S. DeSanti, N. Kemppainen, K. Någren, B.-C. Kim, W. Tsui, M. J. de Leon, Y. Li, L. Mosconi, E. Pirraglia, H. Rusinek, S. DeSanti, B. Kim, W. Tsui, M. J. de Leon, "Regional Analysis of FDG and PIB-PET Images in Normal Aging, Mild Cognitive Impairment, and Alzheimer's Disease," *Eur J Nucl Med Mol Imaging*, vol. 35, pp. 2169–2181, 2008, doi: 10.1007/s00259-008-0833-y.

[98] M. Verma, A. Vats, and V. Taneja, "Toxic Species in Amyloid Disorders: Oligomers or Mature Fibrils," *Annals of Indian Academy of Neurology*, vol. 18, no. 2, pp. 138–145, Apr. 2015, doi: 10.4103/0972-2327.144284.

[99] A. Lorenzo and B. A. Yanker, "Amyloid Fibrils Toxicity in Alzheimer's Disease and Diabetes," *Annals of the New York Academy of Sciences*, vol. 777, no. 1, pp. 89–95, 1996.

[100] A. Stéphan, S. Laroche, and S. Davis, "Generation of Aggregated-Amyloid in the Rat Hippocampus Impairs Synaptic Transmission and Plasticity and Causes Memory Deficits," *The Journal of Neuroscience*, vol. 21, no. 15, pp. 5703–5714, 2001.

[101] R. Nortley, N. Korte, P. Izquierdo, C. Hirunpattarasilp, A. Mishra, Z. Jaunmuktane, V. Kyrargyri, T. Pfeiffer, L. Khennouf, C. Madry, H. Gong, A. Richard-Loendt, W. Huang, T. Saito, T. C. Saido, S. Brandner, H. Sethi, and D. Attwell, "Amyloid-b Oligomers Constrict Human Capillaries in Alzheimer's Disease via Signaling to Pericytes," *Science*, vol. 365, no. 6450, Jul. 2019, doi: 10.1126/science.aav9518.

[102] R. Kayed, E. Head, J. L. Thompson, T. M. McIntire, S. C. Milton, C. W. Cotman, and C. G. Glabel, "Common Structure of Soluble Amyloid Oligomers Implies Common Mechanism of Pathogenesis," *Science*, vol. 300, no. 5618, pp. 486–489, Apr. 2003, doi: 10.1126/science.1079469.

[103] G. M. Shankar, S. Li, T. H. Mehta, A. Garcia-Munoz, N. E. Shepardson, I. Smith, F. M. Brett, M. A. Farrell, M. J. Rowan, C. A. Lemere, C. M. Regan, D. M. Walsh, B. L. Sabatini, and D. J. Selkoe, "Amyloid-β Protein Dimers Isolated Directly from Alzheimer's Brains Impair Synaptic Plasticity and Memory," *Nature Medicine*, vol. 14, no. 8, pp. 837–842, Aug. 2008, doi: 10.1038/nm1782.

[104] Y. He, M. M. Zheng, Y. Ma, X. J. Han, X. Q. Ma, C. Q. Qu, and Y. F. Du, "Soluble Oligomers and Fibrillar Species of Amyloid β-peptide Differentially Affect Cognitive Functions and Hippocampal Inflammatory Response," *Biochemical and Biophysical Research Communications*, vol. 429, no. 3–4, pp. 125–130, Dec. 2012, doi: 10.1016/J.BBRC.2012.10.129.

[105] C. G. Glabe, "Structural Classification of Toxic Amyloid Oligomers," *Journal of Biological Chemistry*, vol. 283, no. 44, pp. 29639–29643, Oct. 2008, doi: 10.1074/jbc.R800016200.

[106] M. Sakono and T. Zako, "Amyloid Oligomers: Formation and Toxicity of Aβ Oligomers," *FEBS Journal*, vol. 277, no. 6, pp. 1348–1358, Mar. 2010, doi: 10.1111/j.1742-4658.2010.07568.x.

[107] M. P. Lambert, A. K. Barlow, B. A. Chromy, C. Edwards, R. Freed, M. Liosatos, T. E. Morgan, I. Rozovsky, B. Trommer, K. L. Viola, P. Wals, C. Zhang, C. E. Finch, G. A. Krafft, and W. L. Klein, "Diffusible, Nonfibrillar Ligands Derived

from AB 1-42 are Potent Central Nervous System nNeurotoxins," *Proceedings of the Natioanl Academy of Sciences*, vol. 95, no. 11, pp. 6448–6453, 1998, [Online]. Available: www.pnas.org.

[108] A. Prasansuklab and T. Tencomnao, "Amyloidosis in Alzheimer's Disease: The Toxicity of Amyloid beta (Aβ), Mechanisms of Its Accumulation and Implications of Medicinal Plants for Therapy," *Evidence-based Complementary and Alternative Medicine*, vol. 2013, 2013, doi: 10.1155/2013/413808.

[109] J. X. Lu, W. Qiang, W. M. Yau, C. D. Schwieters, S. C. Meredith, and R. Tycko, "Molecular Structure of β-amyloid Fibrils in Alzheimer's Disease Brain Tissue," *Cell*, vol. 154, no. 6, p. 1257, Sep. 2013, doi: 10.1016/j.cell.2013.08.035.

[110] W. Qiang, K. Kelley, and R. Tycko, "Polymorph-specific kinetics and thermodynamics of β-amyloid Fibril Growth," *Journal of the American Chemical Society*, vol. 135, no. 18, pp. 6860–6871, May 2013, doi: 10.1021/ja311963f.

[111] M. Chen, N. P. Schafer, and P. G. Wolynes, "Surveying the Energy Landscapes of Aβ Fibril Polymorphism," *Journal of Physical Chemistry B*, vol. 122, no. 49, pp. 11414–11430, Dec. 2018, doi: 10.1021/acs.jpcb.8b07364.

[112] Y. C. Lin, C. Li, and Z. Fakhraai, "Kinetics of Surface-Mediated Fibrillization of Amyloid-β(12-28) Peptides," *Langmuir*, vol. 34, no. 15, pp. 4665–4672, Apr. 2018, doi: 10.1021/acs.langmuir.7b02744.

[113] W. Zheng, M. Y. Tsai, and P. G. Wolynes, "Comparing the Aggregation Free Energy Landscapes of Amyloid Beta(1-42) and Amyloid Beta(1-40)," *Journal of the American Chemical Society*, vol. 139, no. 46, pp. 16666–16676, Nov. 2017, doi: 10.1021/jacs.7b08089.

[114] M. Bacci, J. Vymětal, M. Mihajlovic, A. Caflisch, and A. Vitalis, "Amyloid β Fibril Elongation by Monomers Involves Disorder at the Tip," *Journal of Chemical Theory and Computation*, vol. 13, no. 10, pp. 5117–5130, Oct. 2017, doi: 10.1021/acs.jctc.7b00662.

[115] N. Schwierz, C. v. Frost, P. L. Geissler, and M. Zacharias, "Dynamics of Seeded Aβ40-Fibril Growth from Atomistic Molecular Dynamics Simulations: Kinetic Trapping and Reduced Water Mobility in the Locking Step," *Journal of the American Chemical Society*, vol. 138, no. 2, pp. 527–539, Jan. 2016, doi: 10.1021/jacs.5b08717.

[116] T. Watanabe-Nakayama, B. R. Sahoo, A. Ramamoorthy, and K. Ono, "High-speed Atomic Force Microscopy Reveals the Structural Dynamics of the Amyloid-β and Amylin Aggregation Pathways," *International Journal of Molecular Sciences*, vol. 21, no. 12, pp. 1–30, Jun. 2020, doi: 10.3390/ijms21124287.

[117] C. G. Alexander, S. Emerson, and A. S. Kesselheim, "Evaluation of Aducanumab for Alzheimer Disease: Scientific Evidence and Regulatory Review Involving Efficacy, Safety, and Futility," *JAMA*, vol. 325, no. 17, pp. 1717–1718, 2021.

[118] R. E. Uhlmann, C. Rother, J. Rasmussen, J. Schelle, C. Bergmann, E. M. Ullrich Gavilanes, S. K. Fritschi, A. Buehler, F. Baumann, A. Skodras, R. Al-Shaana, N. Beschorner, L. Ye, S. A. Kaeser, U. Obermüller, S. Christensen, F. Kartberg, J. B. Stavenhagen, J. U. Rahfeld, "Acute Targeting of Pre-amyloid Seeds in Transgenic Mice Reduces Alzheimer-like Pathology Later in Life," *Nature Neuroscience*, vol. 23, no. 12, pp. 1580–1588, Dec. 2020, doi: 10.1038/s41593-020-00737-w.

[119] R. Tycko, “Physical and Structural Basis for Polymorphism in Amyloid Fibrils,” *Protein Science*, vol. 23, no. 11, pp. 1528–1539, Nov. 2014, doi: 10.1002/pro.2544.

[120] K. Matsuzaki, “Physicochemical Interactions of Amyloid β-peptide with Lipid Bilayers,” *Biochimica et Biophysica Acta (BBA) - Biomembranes*, vol. 1768, no. 8, pp. 1935–1942, Aug. 2007, doi: 10.1016/J.BBAMEM.2007.02.009.

[121] Z. Niu, Z. Zhang, W. Zhao, and J. Yang, “Interactions between Amyloid β Peptide and Lipid Membranes,” *Biochimica et Biophysica Acta (BBA) - Biomembranes*, vol. 1860, no. 9, pp. 1663–1669, Sep. 2018, doi: 10.1016/J.BBAMEM.2018.04.004.

[122] C. Nilsberth, A. Westlind-Danielsson, C. B. Eckman, M. M. Condron, K. Axelman, C. Forsell, C. Stenh, J. Luthman, D. B. Teplow, S. G. Younkin, J. Näslund, and L. Lannfelt, “The ‘Arctic’ APP Mutation (E693G) Causes Alzheimer’s Disease by Enhanced Aβ Protofibril Formation,” *Nature Neuroscience*, vol. 4, no. 9, pp. 887–893, 2001, [Online]. Available: http://neurosci.nature.com

[123] A. Päiviö, J. Jarvet, A. Gräslund, L. Lannfelt, and A. Westlind-Danielsson, “Unique Physicochemical Profile of β-Amyloid Peptide Variant Aβ1–40E22G Protofibrils: Conceivable Neuropathogen in Arctic Mutant Carriers,” *Journal of Molecular Biology*, vol. 339, no. 1, pp. 145–159, May 2004, doi: 10.1016/J.JMB.2004.03.028.

[124] K. A. Knudsen, J. Rosand, D. Karluk, and S. M. Greenberg, “Clinical Diagnosis of Cerebral Amyloid Angiopathy: Validation of the Boston Criteria,” *Neurology*, vol. 56, no. 4, pp. 537–539, 2001.

[125] W. Zheng, M. Y. Tsai, M. Chen, and P. G. Wolynes, “Exploring the Aggregation Free Energy Landscape of the Amyloid-β Protein (1-40),” *Proceedings of the National Academy of Sciences of the United States of America*, vol. 113, no. 42, pp. 11835–11840, Oct. 2016, doi: 10.1073/pnas.1612362113.

[126] P. Hortschansky, V. Schroeckh, T. Christopeit, G. Zandomeneghi, and M. Fändrich, “The Aggregation Kinetics of Alzheimer’s β-amyloid Peptide is Controlled by Stochastic Nucleation,” *Protein Science*, vol. 14, no. 7, pp. 1753–1759, Jul. 2005, doi: 10.1110/ps.041266605.

[127] B. Caughey and P. T. Lansbury, “Protofibrils, Pores, Fibrils, and Neurodegeneration: Separating the Responsible Protein Aggregates from The Innocent Bystanders *,” *Annu. Rev. Neurosci*, vol. 26, pp. 267–98, 2003, doi: 10.1146/annurev.neuro.26.010302.081142.

[128] D. Kashchiev, “Modeling the Effect of Monomer Conformational Change on the Early Stage of Protein Self-assembly into Fibrils,” *Journal of Physical Chemistry B*, vol. 121, no. 1, pp. 35–46, Jan. 2017, doi: 10.1021/acs.jpcb.6b09302.

[129] J. E. Straub and D. Thirumalai, “Toward a Molecular Theory of Early and Late Events in Monomer to Amyloid Fibril Formation,” *Annu. Rev. Phys. Chem*, vol. 62, pp. 437–463, 2011, doi: 10.1146/annurev-physchem-032210-103526.

[130] T. P. J. Knowles, C. A. Waudby, G. L. Devlin, S. I. A. Cohen, A. Aguzzi, M. Vendruscolo, E. M. Terentjev, M. E. Welland, and C. M. Dobson, “An Analytical

Solution to the Kinetics of Breakable Filament Assembly," *Science*, vol. 326, no. 5959, pp. 1533–1537, 2009, doi: 10.1126/science.ll80350.

[131] F. S. Ruggeri, T. Šneideris, M. Vendruscolo, and T. P. J. Knowles, "Atomic Force Microscopy for Single Molecule Characterisation of Protein Aggregation," *Archives of Biochemistry and Biophysics*, vol. 664, pp. 134–148, Mar. 2019, doi: 10.1016/j.abb.2019.02.001.

[132] M. Törnquist, T. C. T. Michaels, K. Sanagavarapu, X. Yang, G. Meisl, S. I. A. Cohen, T. P. J. Knowles Bd, and S. Linse, "Secondary nucleation in amyloid formation," *Chem. Commun*, vol. 54, p. 8667, 2018, doi: 10.1039/c8cc02204f.

[133] D. Pinotsi, A. K. Buell, C. Galvagnion, C. M. Dobson, G. S. Kaminski Schierle, and C. F. Kaminski, "Direct Observation of Heterogeneous Amyloid Fibril Growth Kinetics via Two-color Super-resolution Microscopy," *Nano Letters*, vol. 14, no. 1, pp. 339–345, Jan. 2014, doi: 10.1021/nl4041093.

[134] T. Ban, D. Hamada, K. Hasegawall, H. Naiki, and Y. Goto, "Direct Observation of Amyloid Fibril Growth Monitored by Thioflavin T Fluorescence," *Journal of Biological Chemistry*, vol. 278, no. 19, pp. 16462–16465, May 2003, doi: 10.1074/jbc.C300049200.

[135] T. C. T. Michaels, A. Šarić, S. Curk, K. Bernfur, P. Arosio, G. Meisl, A. J. Dear, S. I. A. Cohen, C. M. Dobson, M. Vendruscolo, S. Linse, and T. P. J. Knowles, "Dynamics of Oligomer Populations Formed during the Aggregation of Alzheimer's Aβ42 Peptide," *Nature Chemistry*, vol. 12, no. 5, pp. 445–451, May 2020, doi: 10.1038/s41557-020-0452-1.

[136] M. Biancalana and S. Koide, “Molecular Mechanism of Thioflavin-T Binding to Amyloid Fibrils,” *Biochimica et Biophysica Acta - Proteins and Proteomics*, vol. 1804, no. 7, pp. 1405–1412, Jul. 2010, doi: 10.1016/j.bbapap.2010.04.001.

[137] M. S. Z Kellermayer, A. Karsai, M. Benke, K. Soó, and B. Penke, “Stepwise Dynamics of Epitaxially Growing Single Amyloid Fibrils,” *Proceedings of the National Academy of Science*, vol. 105, no. 1, pp. 141–144, 2007, [Online]. Available: www.pnas.org/cgi/content/full/

[138] Q. Huang, H. Wang, H. Gao, P. Cheng, L. Zhu, C. Wang, and Y. Yang, “In Situ Observation of Amyloid Nucleation and Fibrillation by FastScan Atomic Force Microscopy,” *Journal of Physical Chemistry Letters*, vol. 10, no. 2, pp. 214–222, Jan. 2019, doi: 10.1021/acs.jpclett.8b03143.

[139] M. Sleutel, I. van den Broeck, N. van Gerven, C. Feuillie, W. Jonckheere, C. Valotteau, Y. F. Dufrêne, and H. Remaut, “Nucleation and Growth of a Bacterial Functional Amyloid at Single-fiber Resolution,” *Nature Chemical Biology*, vol. 13, no. 8, pp. 902–908, Aug. 2017, doi: 10.1038/nchembio.2413.

[140] C. Goldsbury, J. Kistler, U. Aebi, T. Arvinte, and G. J. S. Cooper, “Watching Amyloid Fibrils Grow by Time-lapse Atomic Force Microscopy,” *Journal of Molecular Biology*, vol. 285, no. 1, pp. 33–39, 1999, [Online]. Available: http://www.idealibrary.com

[141] H. K. L. Blackley, G. H. W. Sanders, M. C. Davies, C. J. Roberts, S. J. B. Tendler, and M. J. Wilkinson, “In-situ Atomic Force Microscopy Study of β-amyloid Fibrillization,” *Journal of Molecular Biology*, vol. 298, no. 5, pp. 833–840, May 2000, doi: 10.1006/jmbi.2000.3711.

[142] W. Hoyer, D. Cherny, V. Subramaniam, and T. M. Jovin, “Rapid Self-assembly of α-synuclein Observed by in situ Atomic Force Microscopy,” *Journal of Molecular Biology*, vol. 340, no. 1, pp. 127–139, Jun. 2004, doi: 10.1016/j.jmb.2004.04.051.

[143] S. Banerjee, M. Hashemi, K. Zagorski, and Y. L. Lyubchenko, “Interaction of Aβ42 with Membranes Triggers the Self-assembly into Oligomers,” *International Journal of Molecular Sciences*, vol. 21, no. 3, Feb. 2020, doi: 10.3390/ijms21031129.

[144] M. M. Wördehoff, O. Bannach, H. Shaykhalishahi, A. Kulawik, S. Schiefer, D. Willbold, W. Hoyer, and E. Birkmann, “Single Fibril Growth Kinetics of α-synuclein,” *Journal of Molecular Biology*, vol. 427, no. 6, pp. 1428–1435, Mar. 2015, doi: 10.1016/j.jmb.2015.01.020.

[145] J. R. Kim, A. Muresan, K. Y. C. Lee, and R. M. Murphy, “Urea Modulation of β-amyloid Fibril Growth: Experimental Studies and Kinetic Models,” *Protein Science*, vol. 13, no. 11, pp. 2888–2898, Dec. 2008, doi: 10.1110/ps.04847404.

[146] X. Yu and J. Zheng, “Cholesterol Promotes the Interaction of Alzheimer β-Amyloid Monomer with Lipid Bilayer,” *Journal of Molecular Biology*, vol. 421, no. 4–5, pp. 561–571, Aug. 2012, doi: 10.1016/J.JMB.2011.11.006.

[147] I. Rivera, R. Capone, D. M. Cauvi, N. Arispe, and A. de Maio, “Modulation of Alzheimer’s amyloid β peptide oligomerization and toxicity by extracellular Hsp70,” *Cell Stress and Chaperones*, vol. 23, pp. 269–279, 2018, doi: 10.1007/s12192-017-0839-0.

[148] J. Luo, C.-H. Yu, H. Yu, R. Borstnar, S. C. L Kamerlin, A. Gra, J. Pieter Abrahams, and S. K. T S Wa, “Cellular Polyamines Promote Amyloid-Beta (Aβ)

Peptide Fibrillation and Modulate the Aggregation Pathways," *ACS Chem. Neurosci*, vol. 4, p. 39, 2013, doi: 10.1021/cn300170x.

[149] E. K. Esbjörner, F. Chan, E. Rees, M. Erdelyi, L. M. Luheshi, C. W. Bertoncini, C. F. Kaminski, C. M. Dobson, and G. S. Kaminski Schierle, "Direct Observations of Amyloid β Self-Assembly in Live Cells Provide Insights into Differences in the Kinetics of Aβ(1–40) and Aβ(1–42) Aggregation," *Chemistry & Biology*, vol. 21, no. 6, pp. 732–742, Jun. 2014, doi: 10.1016/J.CHEMBIOL.2014.03.014.

[150] D. M. Walsh, I. Klyubin, J. v Fadeeva, W. K. Cullen, R. Anwyl, M. S. Wolfe, M. J. Rowan, and D. J. Selkoe, "Naturally Secreted Oligomers of Amyloid-beta Protein Potently Inhibit Hippocampal Long-term Potentiation in vivo," *Nature*, vol. 416, no. 6880, pp. 535–539, 2002, [Online]. Available: www.nature.com

[151] D. J. Selkoe, "Folding Protein in Fatal Ways," *Nature*, vol. 426, no. 6968, pp. 900–904, 2003, doi: 10.1038/nature02264.

[152] M. Bokvist and G. Grö, "Misfolding of Amyloidogenic Proteins at Membrane Surfaces: The Impact of Macromolecular Crowding," *Journal of American Chemical Society*, vol. 129, pp. 14848–14849, 2007, doi: 10.1021/ja076059o.

[153] A. K. Srivastava, J. M. Pittman, J. Zerweck, B. S. Venkata, P. C. Moore, J. R. Sachleben, and S. C. Meredith, "β-Amyloid Aggregation and Heterogeneous Nucleation," *Protein Science*, vol. 28, no. 9, pp. 1567–1581, 2019, doi: 10.1002/pro.3674.

[154] F. Hane, E. Drolle, R. Gaikwad, E. Faught, and Z. Leonenko, "Amyloid-β aggregation on model lipid membranes: An atomic force microscopy study,"

Journal of Alzheimer's Disease, vol. 26, no. 3, pp. 485–494, 2011, doi: 10.3233/JAD-2011-102112.

[155] K. J. Korshavn, C. Satriano, Y. Lin, R. Zhang, M. Dulchavsky, A. Bhunia, M. I. Ivanova, Y. H. Lee, C. la Rosa, M. H. Lim, and A. Ramamoorthy, "Reduced Lipid Bilayer Thickness Regulates the Aggregation and Cytotoxicity of Amyloid-β," *Journal of Biological Chemistry*, vol. 292, no. 11, pp. 4638–4650, Mar. 2017, doi: 10.1074/jbc.M116.764092.

[156] M. S. Terakawa, Y. Lin, M. Kinoshita, S. Kanemura, D. Itoh, T. Sugiki, M. Okumura, A. Ramamoorthy, and Y. H. Lee, "Impact of Membrane Curvature on Amyloid Aggregation," *Biochimica et Biophysica Acta (BBA) - Biomembranes*, vol. 1860, no. 9, pp. 1741–1764, Sep. 2018, doi: 10.1016/J.BBAMEM.2018.04.012.

[157] C. C. Curtain, F. E. Ali, D. G. Smith, A. I. Bush, C. L. Masters, and K. J. Barnham, "Metal ions, pH, and Cholesterol Regulate the Interactions of Alzheimer's Disease Amyloid-β Peptide with Membrane Lipid," *Journal of Biological Chemistry*, vol. 278, no. 5, pp. 2977–2982, Jan. 2003, doi: 10.1074/jbc.M205455200.

[158] J. M. Cordy, N. M. Hooper, and A. J. Turner, "The Involvement of Lipid Rafts in Alzheimer's Disease," *Molecular Membrane Biology*, vol. 23, no. 1, pp. 111–122, Jan. 2006, doi: 10.1080/09687860500496417.

[159] C. M. Yip, E. A. Elton, A. A. Darabie, M. R. Morrison, and J. Mclaurin, "Cholesterol, a Modulator of Membrane-associated Aβ-fibrillogenesis and

Neurotoxicity," *Journal of Molecular Biology*, vol. 311, no. 4, pp. 723–734, Aug. 2001, doi: 10.1006/JMBI.2001.4881.

[160] A. Choucair, M. Chakrapani, B. Chakravarthy, J. Katsaras, and L. J. Johnston, "Preferential Accumulation of Aβ(1−42) on Gel Phase Domains of Lipid Bilayers: An AFM and Fluorescence Study," *Biochimica et Biophysica Acta (BBA) - Biomembranes*, vol. 1768, no. 1, pp. 146–154, Jan. 2007, doi: 10.1016/J.BBAMEM.2006.09.005.

[161] M. S. Terakawa, H. Yagi, M. Adachi, Y. H. Lee, and Y. Goto, "Small Liposomes Accelerate the Fibrillation of Amyloid β(1- 40)," *Journal of Biological Chemistry*, vol. 290, no. 2, pp. 815–826, Jan. 2015, doi: 10.1074/jbc.M114.592527.

[162] D. J. Lindberg, E. Wesén, J. Björkeroth, S. Rocha, and E. K. Esbjörner, "Lipid Membranes Catalyse the Fibril Formation of the Amyloid-β (1–42) Peptide through Lipid-fibril Interactions that Reinforce Secondary Pathways," *Biochimica et Biophysica Acta (BBA) - Biomembranes*, vol. 1859, no. 10, pp. 1921–1929, Oct. 2017, doi: 10.1016/J.BBAMEM.2017.05.012.

[163] E. Hellstrand, E. Sparr, and S. Linse, "Retardation of Aβ Fibril Formation by Phospholipid Vesicles Depends on Membrane Phase Behavior," *Biophysical Journal*, vol. 98, no. 10, pp. 2206–2214, May 2010, doi: 10.1016/J.BPJ.2010.01.063.

[164] M. Safieh, A. D. Korczyn, and D. M. Michaelson, "ApoE4: An Emerging Therapeutic Target for Alzheimer's Disease," *BMC Medicine*, vol. 17, no. 1, Mar. 2019, doi: 10.1186/s12916-019-1299-4.

[165] K. Blennow, M. J. de Leon, and H. Zetterberg, “Alzheimer’s Disease,” *The Lancet*, vol. 368, no. 9533, pp. 387–403, Jul. 2006, doi: 10.1016/S0140-6736(06)69113-7.

[166] Q. Jiang, C. Y. D. Lee, S. Mandrekar, B. Wilkinson, P. Cramer, N. Zelcer, K. Mann, B. Lamb, T. M. Willson, J. L. Collins, J. C. Richardson, J. D. Smith, T. A. Comery, D. Riddell, D. M. Holtzman, P. Tontonoz, and G. E. Landreth, “ApoE Promotes the Proteolytic Degradation of Aβ,” *Neuron*, vol. 58, no. 5, pp. 681–693, 2008.

[167] K. Hall, J. Murrell, A. Ogunniyi, M. Deeg, O. Baiyewu, S. Gao, O. Gureje, J. Dickens, R. Evans, V. Smith-Gamble, F. W. Unverzagt, J. Shen, and H. Hendrie, “Cholesterol, APOE Genotype, and Alzheimer Disease: An Epidemiologic Study of Nigerian Yoruba,” *Neurology*, vol. 66, no. 2, pp. 223–227, Jan. 2006, doi: 10.1212/01.wnl.0000194507.39504.17.

[168] O. Gureje, A. Ogunniyi, O. Baiyewu, B. Price, F. W. Unverzagt, R. M. Evans, V. Smith-Gamble, K. A. Lane, S. Gao, K. S. Hall, H. C. Hendrie, and J. R. Murrell, “APOE ε4 is not Associated with Alzheimer’s Disease in Elderly Nigerians,” *Annals of Neurology*, vol. 59, no. 1, pp. 182–185, Jan. 2006, doi: 10.1002/ana.20694.

[169] X.-D. Cai, T. E. Golde, and S. G. Younkin, “Release of Excess Amyloid Beta Protein from a Mutant Amyloid Beta Protein Precursor,” *Science*, vol. 1993, pp. 514–516, 1993.

[170] C. Haass, C. A. Lemere, A. Capell, M. Citron, P. Seubert, D. Schenk, L. Lannfelt, and D. J. Selkoe, “The Swedish Mutation Cause Early-onset Alzheimer’s Disease

by Beta-secretase Cleavage within the Secretory Pathway," *Nature Medicine*, vol. 1, no. 12, pp. 1291–1296, 1995.

[171] R. Vassar, B. D. Bennett, S. Babu-Khan, S. Kahn, E. A. Mendiaz, P. Denis, D. B. Teplow, S. Ross, P. Amarante, R. Loeloff, Y. Luo, S. Fisher, J. Fuller, S. Edenson, J. Lile, M. A. Jarosinski, A. L. Biere, E. Curran, T. Burgess, "β-Secretase Cleavage of Alzheimer's Amyloid Precursor Protein by the Transmembrane Aspartic Protease BACE," *Science*, vol. 286, no. 5440, pp. 735–741, Oct. 1999, doi: 10.1126/science.286.5440.735.

[172] E. H. Koo and S. L. Squazzo, "Evidence that Production and Release of Amyloid beta-protein Involves the Endocytic Pathway," *Journal of Biological Chemistry*, vol. 269, no. 26, pp. 17386–17389, Jul. 1994, doi: 10.1016/S0021-9258(17)32449-3.

[173] L. Miravalle, T. Tokuda, R. Chiarle, G. Giaccone, O. Bugiani, F. Tagliavini, B. Frangione, and J. Ghiso, "Substitutions at Codon 22 of Alzheimer's Ab Pinduce Diverse Conformational Changes and Apoptotic Effects Human Cerebral Endothelial Cells," *Journal of Biological Chemistry*, vol. 275, no. 35, pp. 27110–27116, Sep. 2000, doi: 10.1074/jbc.M003154200.

[174] A. Baumketner, M. Griffin Krone, and J.-E. Shea, "Role of the Familial Dutch Mutation E22Q in the Folding and Aggregation of the 15-28 Fragment of the Alzheimer amyloid-beta Protein," *PNAS*, vol. 105, no. 16, pp. 6027–6032, 2008.

[175] L. Morelli, R. Llovera, S. A. Gonzalez, J. L. Affranchino, F. Prelli, B. Frangione, J. Ghiso, and E. M. Castaño, "Differential Degradation of Amyloid β Genetic Variants Associated with Hereditary Dementia or Stroke by Insulin-degrading

Enzyme," *Journal of Biological Chemistry*, vol. 278, no. 26, pp. 23221–23226, Jul. 2003, doi: 10.1074/jbc.M300276200.

[176] D. Type Author, E. Levy, M. D. Carman, I. J. Fernandez-Madrid, M. D. Power, I. Lieberburg, S. G. van Duinen, G. A. Th M Bots, W. Luyendijk, and B. Frangione, "Mutation of the Alzheimer's Disease Amyloid Gene in Hereditary Cerebral Hemorrhage, Dutch Type," *Science*, vol. 248, no. 4959, pp. 1124–1126, 1990.

[177] D. J. Watson, A. D. Lander, and D. J. Selkoe, "Heparin-binding Properties of the Amyloidogenic Peptides Aβ and Amylin: Dependence on Aggregation State and Inhibition by Congo Red," *Journal of Biological Chemistry*, vol. 272, no. 50, pp. 31617–31624, Dec. 1997, doi: 10.1074/jbc.272.50.31617.

[178] A. K. Sian, E. R. Frears, O. M. A. El-Agnaf, B. P. Patel, M. F. Manca, G. Siligardi, R. Hussain, and B. M. Austen, "Oligomerization of β-amyloid of the Alzheimer's and the Dutch-cerebral-hemorrhage Types," *Biochem. J*, vol. 349, pp. 299–308, 2000.

[179] W. P. Esler, A. M. Felix, E. R. Stimson, M. J. Lachenmann, J. R. Ghilardi, Y. A. Lu, H. v. Vinters, P. W. Mantyh, J. P. Lee, and J. E. Maggio, "Activation Barriers to Structural Transition Determine Deposition Rates of Alzheimer's Disease Aβ Amyloid," *Journal of Structural Biology*, vol. 130, no. 2–3, pp. 174–183, Jun. 2000, doi: 10.1006/JSBI.2000.4276.

[180] N. G. Sgourakis, Y. Yan, S. A. McCallum, C. Wang, and A. E. Garcia, "The Alzheimer's Peptides Aβ40 and 42 Adopt Distinct Conformations in Water: A Combined MD / NMR Study," *Journal of Molecular Biology*, vol. 368, no. 5, pp. 1448–1457, May 2007, doi: 10.1016/J.JMB.2007.02.093.

[181] L. Hou, H. Shao, Y. Zhang, H. Li, N. K. Menon, E. B. Neuhaus, J. M. Brewer, I. J. L. Byeon, D. G. Ray, M. P. Vitek, T. Iwashita, R. A. Makula, A. B. Przybyla, and M. G. Zagorski, "Solution NMR Studies of the Aβ(1-40) and Aβ(1-42) Peptides Establish that the Met35 Oxidation State Affects the Mechanism of Amyloid Formation," *Journal of the American Chemical Society*, vol. 126, no. 7, pp. 1992–2005, Feb. 2004, doi: 10.1021/ja036813f.

[182] P. Davies and A. J. F. Maloney, "Selective Loss of Central Cholinergic Neurons in Alzheimer'S Disease," *The Lancet*, vol. 308, no. 8000, p. 1403, Dec. 1976, doi: 10.1016/S0140-6736(76)91936-X.

[183] R. T. Bartus, "On Neurodegenerative Diseases, Models, and Treatment Strategies: Lessons Learned and Lessons Forgotten a Generation Following the Cholinergic Hypothesis," *Experimental Neurology*, vol. 163, no. 2, pp. 495–529, Jun. 2000, doi: 10.1006/EXNR.2000.7397.

[184] A. v. Terry and J. J. Buccafusco, "The Cholinergic Hypothesis of Age and Alzheimer's Disease-related Cognitive Deficits: Recent Challenges and Their Implications for Novel Drug Development," *Journal of Pharmacology and Experimental Therapeutics*, vol. 306, no. 3, pp. 821–827, Sep. 2003, doi: 10.1124/jpet.102.041616.

[185] J. A. Deutsch, "The Cholinergic Synapse and the Site of Memory," *Science*, vol. 174, no. 4011, pp. 788–794, 1971.

[186] J. J. Buccafusco and A. v Terry, "Multiple Central Nervous System Targets for Eliciting Beneficial Effects on Memory and Cognition," *Journal of Pharmacology*

and Experimental Therapeutics, vol. 295, no. 2, pp. 438–446, 2000, [Online]. Available: http://www.jpet.org

[187] P. T. Francis, A. M. Palmer, M. Snape, and G. K. Wilcock, "The Cholinergic Hypothesis of Alzheimer's Disease: A Review of Progress," *Journal of Neurology Neurosurgery and Psychiatry*, vol. 66, no. 2, pp. 137–147, 1999, doi: 10.1136/jnnp.66.2.137.

[188] K. L. Davis, R. C. Mohs, D. Marin, D. P. Purohit, D. P. Perl, M. Lantz, G. Austin, and V. Haroutunian, "Cholinergic Markers in Elderly Patients With Early Signs of Alzheimer Disease," *Jama*, vol. 281, no. 15, pp. 1401–1406, 1999, [Online]. Available: https://jamanetwork.com/

[189] S. T. DeKosky, M. D. Ikonomovic, S. D. Styren, L. Beckett, S. Wisniewski, D. A. Bennett, E. J. Cochran, J. H. Kordower, and E. J. Mufson, "Upregulation of Choline Acetyltransferase Activity in Hippocampus and Frontal Cortex of Elderly Subjects with Mild Cognitive Impairment," *Annals of Neurology: Official Journal of the American Neurological Association and the Child Neurology Society*, vol. 51, no. 2, pp. 145–155, 2002.

[190] M. Goedert, M. G. Spillantini, and R. A. Crowther, "Tau Proteins and Neurofibrillary Degeneration," *Brain Pathology*, vol. 1, pp. 279–286, 1991.

[191] K. Iqbal, A. del C. Alonso, S. Chen, M. O. Chohan, E. El-Akkad, C. X. Gong, S. Khatoon, B. Li, F. Liu, A. Rahman, H. Tanimukai, and I. Grundke-Iqbal, "Tau Pathology in Alzheimer Disease and Other Tauopathies," *Biochimica et Biophysica Acta - Molecular Basis of Disease*, vol. 1739, no. 2, pp. 198–210, Jan. 2005, doi: 10.1016/j.bbadis.2004.09.008.

[192] B. Frost, R. L. Jacks, and M. I. Diamond, “Propagation of Tau Misfolding from the Outside to the inside of a Cell,” *Journal of Biological Chemistry*, vol. 284, no. 19, pp. 12845–12852, May 2009, doi: 10.1074/jbc.M808759200.

[193] C. W. Wittmann, M. F. Wszolek, J. M. Shulman, P. M. Salvaterra, J. Lewis, M. Hutton, and M. B. Feany, “Tauopathy in Drosophila: Neurodegeneration without Neurofibrillary Tangles,” *Science*, vol. 293, no. 5530, pp. 711–714, Jul. 2001, doi: 10.1126/science.1062382.

[194] A. Boutajangot, J. Ingadottir, P. Davies, and E. M. Sigurdsson, “Passive Immunization Targeting Pathological Phopho-tau Protein in a mouse Reduces Functional Decline and Clears Tau Aggregates from the Brain,” *J. Neurochem*, vol. 118, no. 4, pp. 658–667, 2011, doi: 10.1111/j.1471-4159.2011.07337.x.

[195] P.-P. Liu, Y. Xie, X.-Y. Meng, and J.-S. Kang, “History and Progress of Hypotheses and Clinical Trials for Alzheimer’s Disease,” *Signal Transduction and Targeted Therapy*, vol. 4, no. 1, pp. 1–22, 2019, doi: 10.1038/s41392-019-0063-8.

[196] W. J. Brecht, F. M. Harris, S. Chang, I. Tesseur, G. Q. Yu, Q. Xu, J. D. Fish, T. Wyss-Coray, M. Buttini, L. Mucke, R. W. Mahley, and Y. Huang, “Neuron-Specific Apolipoprotein E4 Proteolysis Is Associated with Increased Tau Phosphorylation in Brains of Transgenic Mice,” *Journal of Neuroscience*, vol. 24, no. 10, pp. 2527–2534, Mar. 2004, doi: 10.1523/JNEUROSCI.4315-03.2004.

[197] C. J. Phiel, C. A. Wilson, V. M-Y Lee, and P. S. Klein, “GSK-3a Regulates Production of Alzheimer’s Disease Amyloid-b Peptides,” *Nature*, vol. 423, no. 6938, pp. 435–439, 2003, [Online]. Available: www.nature.com/nature

[198] G. M. Gibb, J. Pearce, J. C. Betts, S. Lovestone, M. M. Hoffmann, W. Maerz, W. P. Blackstock, and B. H. Anderton, "Differential Effects of Apolipoprotein E Isoforms on Phosphorylation at Specific Sites on Tau by Glycogen Synthase Kinase-3β Identified by Nano-electrospray Mass Spectrometry," *FEBS Letters*, vol. 485, no. 2–3, pp. 99–103, Nov. 2000, doi: 10.1016/S0014-5793(00)02196-7.

[199] X. Li, P. Lei, Q. Tuo, S. Ayton, Q.-X. Li, S. Moon, I. Volitakis, R. Liu, C. L. Masters, D. I. Finkelstein, and A. I. Bush, "Enduring Elevations of Hippocampal Amyloid Precursor Protein and Iron Are Features of β-Amyloid Toxicity and Are Mediated by Tau," *Neurotherapeutics*, vol. 12, no. 4, pp. 862–873, 2015, doi: 10.1007/s13311-015-0378-2.

[200] P. Lei, S. Ayton, D. I. Finkelstein, L. Spoerri, G. D. Ciccotosto, D. K. Wright, B. X. W Wong, P. A. Adlard, R. A. Cherny, L. Q. Lam, B. R. Roberts, I. Volitakis, G. F. Egan, C. A. McLean, R. Cappai, J. A. Duce, and A. I. Bush, "Tau Deficiency Induces Parkinsonism with Dementia by Impairing APP-Mediated Iron Export," *Nature Medicine*, 2012, doi: 10.1038/nm.2613.

[201] L. Gong, X. Tian, J. Zhou, Q. Dong, Y. Tan, Y. Lu, J. Wu, Y. Zhao, and X. Liu, "Iron Dyshomeostasis Induces Binding of APP to BACE1 for Amyloid Pathology, and Impairs APP/Fpn1 Complex in Microglia: Implication in Pathogenesis of Cerebral Microbleeds," *Cell Transplatation*, vol. 28, no. 8, pp. 1009–1017, 2019, doi: 10.1177/0963689719831707.

[202] C. Persichilli, S. E. Hill, J. Mast, and M. Muschol, "Does Thioflavin-T Detect Oligomers Formed during Amyloid Fibril Assembly," *Biophysical Jornal*, vol. 100, no. 3, p. 538a, 2011.

[203] I. W. Hamley, “The Amyloid beta Peptide: A Chemist’s Perspective. Role in Alzheimer’s and Fibrillization,” *Chemical Reviews*, vol. 112, no. 10, pp. 5147–5192, Oct. 2012, doi: 10.1021/cr3000994.

[204] Y. Xu, M. S. Safari, W. Ma, N. P. Schafer, P. G. Wolynes, and P. G. Vekilov, “Steady, Symmetric, and Reversible Growth and Dissolution of Individual Amyloid-β Fibrils,” *ACS Chemical Neuroscience*, vol. 10, no. 6, pp. 2967–2976, 2019, doi: 10.1021/acschemneuro.9b00179.

[205] G. Tesei, E. Hellstrand, K. Sanagavarapu, S. Linse, E. Sparr, R. Vácha, and M. Lund, “Aggregate Size Dependence of Amyloid Adsorption onto Charged Interfaces,” *Langmuir*, vol. 34, no. 4, pp. 1266–1273, Jan. 2018, doi: 10.1021/acs.langmuir.7b03155.

[206] M. v. Maslova, L. G. Gerasimova, and W. Forsling, “Surface Properties of Cleaved Mica,” *Colloid Journal*, vol. 66, no. 3, pp. 322–328, 2004.

[207] H. Schlichting and K. Gersten, *Boundary-layer Theory*. Springer, 2016.

[208] J. Dobson, A. Kumar, L. F. Willis, R. Tuma, D. R. Higazi, R. Turner, D. C. Lowe, A. E. Ashcroft, S. E. Radford, N. Kapur, D. J. Brockwell, and F. U. Hartl, “Inducing Protein Aggregation by Extensional Flow,” *Proceedings of the National Academy of Sciences*, vol. 114, no. 18, pp. 4673–4678, 2017, doi: 10.5518/125.

[209] L. Ashton, J. Dusting, E. Imomoh, S. Balabani, and E. W. Blanch, “Shear-induced Unfolding of Lysozyme Monitored in situ,” *Biophysical Journal*, vol. 96, no. 10, pp. 4231–4236, 2009, doi: 10.1016/j.bpj.2009.02.024.

[210] W. Zheng, N. P. Schafer, A. Davtyan, G. A. Papoian, and P. G. Wolynes, “Predictive Energy Landscapes for Protein-protein Association,” *Proceedings of*

the National Academy of Sciences of the United States of America, vol. 109, no. 47, pp. 19244–19249, Nov. 2012, doi: 10.1073/pnas.1216215109.

[211] M. C. Byington, M. S. Safari, J. C. Conrad, and P. G. Vekilov, "Protein Conformational Flexibility Enables the Formation of Dense Liquid Clusters: Tests Using Solution Shear," *Journal of Physical Chemistry Letters*, vol. 7, no. 13, pp. 2339–2345, Jul. 2016, doi: 10.1021/acs.jpclett.6b00822.

[212] M. C. Byington, M. S. Safari, J. C. Conrad, and P. G. Vekilov, "Shear Flow Suppresses the Volume of the Nucleation Precursor Clusters in Lysozyme Solutions," *Journal of Crystal Growth*, vol. 468, pp. 493–501, Jun. 2017, doi: 10.1016/j.jcrysgro.2016.12.080.

[213] W. Qiang, W. M. Yau, J. X. Lu, J. Collinge, and R. Tycko, "Structural Variation in Amyloid-β Fibrils from Alzheimer's Disease Clinical Subtypes," *Nature*, vol. 541, no. 7636, pp. 217–221, Jan. 2017, doi: 10.1038/nature20814.

[214] A. T. Petkova, R. D. Leapman, Z. Guo, W.-M. Yau, M. P. Mattson, and R. Tycko, "Self-propogating, Molecular-level Polymorphism in Alzheimer's Beta-amyloid Fibrils," *Science*, vol. 307, no. 5707, pp. 262–265, 2005.

[215] B. Chen, K. R. Thurber, F. Shewmaker, R. B. Wickner, and R. Tycko, "Measurement of Amyloid Fibril Mass-per-length by Tilted-beam Transmission Electron Microscopy," *Proceedings of the National Academy of Science*, vol. 106, no. 34, pp. 14339–14344, 2009, [Online]. Available: www.pnas.org/cgi/content/full/

[216] A. W. P. Fitzpatrick, G. T. Debelouchina, M. J. Bayro, D. K. Clare, M. A. Caporini, V. S. Bajaj, C. P. Jaroniec, L. Wang, V. Ladizhansky, S. A. Müller, C. E.

MacPhee, C. A. Waudby, H. R. Mott, A. de Simone, T. P. J. Knowles, H. R. Saibil, M. Vendruscolo, E. v. Orlova, R. G. Griffin, "Atomic Structure and Hierarchical Assembly of a Cross-β Amyloid Fibril," *Proceedings of the National Academy of Sciences of the United States of America*, vol. 110, no. 14, pp. 5468–5473, Apr. 2013, doi: 10.1073/pnas.1219476110.

[217] A. K. Paravastu, R. D. Leapman, W.-M. Yau, and R. Tycko, "Molecular structural basis for polymorphism in Alzheimer's-amyloid fibrils," *Proceedings of the National Academy of Science*, vol. 105, no. 47, pp. 18349–18354, 2008, [Online]. Available: www.pnas.org/cgi/content/full/

[218] O. Galkin, R. L. Nagel, and P. G. Vekilov, "The Kinetics of Nucleation and Growth of Sickle Cell Hemoglobin Fibers," *Journal of Molecular Biology*, vol. 365, no. 2, pp. 425–439, Jan. 2007, doi: 10.1016/j.jmb.2006.10.001.

[219] P. G. Vekilov, "Sickle-cell Hemoglobin Polymerization: Is it the Primary Pathogenic Event of Sickle-cell Anaemia?," *British Journal of Haematology*, vol. 139, no. 2. pp. 173–184, Oct. 2007. doi: 10.1111/j.1365-2141.2007.06794.x.

[220] J. Ferkinghoff-Borg, J. Fonslet, C. B. Andersen, S. Krishna, S. Pigolotti, H. Yagi, Y. Goto, D. Otzen, and M. H. Jensen, "Stop-and-go Kinetics in Amyloid Fibrillation," *Physical Review E - Statistical, Nonlinear, and Soft Matter Physics*, vol. 82, no. 1, Jul. 2010, doi: 10.1103/PhysRevE.82.010901.

[221] T. Ban, M. Hoshino, S. Takahashi, D. Hamada, K. Hasegawa, H. Naiki, and Y. Goto, "Direct Observation of Aβ Amyloid Fibril Growth and Inhibition," *Journal of Molecular Biology*, vol. 344, no. 3, pp. 757–767, Nov. 2004, doi: 10.1016/j.jmb.2004.09.078.

[222] N. P. Reynolds, J. Adamcik, J. T. Berryman, S. Handschin, A. A. H. Zanjani, W. Li, K. Liu, A. Zhang, and R. Mezzenga, “Competition between Crystal and Fibril Formation in Molecular Mutations of Amyloidogenic Peptides,” *Nature Communications*, vol. 8, no. 1, Dec. 2017, doi: 10.1038/s41467-017-01424-4.

[223] B. O’Nuallain, S. Shivaprasad, I. Kheterpal, and R. Wetzel, “Thermodynamics of Aβ(1-40) Amyloid Fibril Elongation,” *Biochemistry*, vol. 44, no. 38, pp. 12709–12718, Sep. 2005, doi: 10.1021/bi050927h.

[224] Y. Xu, K. Knapp, K. N. Le, N. P. Schafer, M. S. Safari, A. Davtyan, P. G. Wolynes, and P. G. Vekilov, “Frustrated Peptide Chains at the Fibril Tip Control the Kinetics of Growth of Amyloid-β Fibrils,” *Proceedings of the National Academy of Sciences*, vol. 118, no. 38, 2021, doi: 10.1073/pnas.2110995118/-/DCSupplemental.

[225] M. Auton, L. F. Marcelo Holthauzen, and D. Wayne Bolen, “Anatomy of Energetic Changes Accompanying Urea-induced Protein Denaturation,” *Proceedings of the National Academy of Sciences*, vol. 104, no. 39, pp. 15317–15322, 2007, [Online]. Available: www.pnas.org/cgi/content/full/

[226] L. Hua, R. Zhou, D. Thirumalai, and B. J. Berne, “Urea denaturation by stronger dispersion interactions with proteins than water implies a 2-stage unfolding,” *Proceedings of the National Academy of Sciences*, vol. 105, no. 44, pp. 16928–16933, 2008, [Online]. Available: www.pnas.orgcgidoi10.1073pnas.0808427105

[227] C.-L. Berthollet, *Essai de Statique Chimique*, vol. 1. 1803.

[228] M. Warzecha, L. Verma, B. F. Johnston, J. C. Palmer, A. J. Florence, and P. G. Vekilov, “Olanzapine Crystal Symmetry Originates in Preformed

Centrosymmetric Solute Dimers," *Nature Chemistry*, vol. 12, no. 10, pp. 914–920, Oct. 2020, doi: 10.1038/s41557-020-0542-0.

[229] B. Tarus, T. T. Tran, J. Nasica-Labouze, F. Sterpone, P. H. Nguyen, and P. Derreumaux, "Structures of the Alzheimer's Wild-Type Aβ1-40 Dimer from Atomistic Simulations," *Journal of Physical Chemistry B*, vol. 119, no. 33, pp. 10478–10487, Aug. 2015, doi: 10.1021/acs.jpcb.5b05593.

[230] J. C. Stroud, C. Liu, P. K. Teng, and D. Eisenberg, "Toxic Fibrillar Oligomers of Amyloid-β Have Cross-β Structure," *Proceedings of the National Academy of Sciences of the United States of America*, vol. 109, no. 20, pp. 7717–7722, May 2012, doi: 10.1073/pnas.1203193109.

[231] K. Kawahara and C. Tanford, "Viscosity and Density of Aqueous Solutions of Urea and Downloaded from," *Journal of Biological Chemistry*, vol. 241, no. 13, pp. 3228–3232, 1966, [Online]. Available: http://www.jbc.org/

[232] E. S. Courtenay, M. W. Capp, and A. M. T. Record, "Thermodynamics of Interactions of Urea and Guanidinium Salts with Protein Surface: Relationship between Solute Effects on Protein Processes and Changes in Water-accessible Surface Area," *Protein Science*, vol. 10, p. 2485, 2001, doi: 10.1101/ps.20801.

[233] H. J. Bakker and J. L. Skinner, "Vibrational Spectroscopy as a Probe of Structure and Dynamics in Liquid Water," *Chemical Reviews*, vol. 110, no. 3, pp. 1498–1517, Mar. 2010, doi: 10.1021/cr9001879.

[234] J. N. Onuchic, N. D. Socci, Z. Luthey-Schulten, and P. G. Wolynes, "Protein Folding Funnels: The Nature of the Transition State Ensemble," *Folding and Design*, vol. 1, no. 6, pp. 441–450, 1996.

[235] M. Chen and P. G. Wolynes, “Aggregation Landscapes of Huntingtin Exon 1 Protein Fragments and the Critical Repeat Length for the Onset of Huntington’s Disease,” *Proceedings of the National Academy of Sciences of the United States of America*, vol. 114, no. 17, pp. 4406–4411, Apr. 2017, doi: 10.1073/pnas.1702237114.

[236] W. P. Esler, E. R. Stimson, J. M. Jennings, H. v. Vinters, J. R. Ghilardi, J. P. Lee, P. W. Mantyh, and J. E. Maggio, “Alzheimer’s Disease Amyloid Propagation by a Template-dependent Dock- lock mechanism,” *Biochemistry*, vol. 39, no. 21, pp. 6288–6295, May 2000, doi: 10.1021/bi992933h.

[237] J. K. Myers, C. N. Pace, J. M. Scholtz, and M. Scholtz, “m Values and Heat Capacity Changes: Relation to Changes in Accessible Surface Areas of Protein Unfolding,” *Protein Science*, vol. 4, pp. 2138–2148, 1995.

[238] A. Davtyan, N. P. Schafer, W. Zheng, C. Clementi, P. G. Wolynes, and G. A. Papoian, “AWSEM-MD: Protein Structure Prediction using Coarse-grained Physical Potentials and Bioinformatically Based Local Structure Biasing,” *Journal of Physical Chemistry B*, vol. 116, no. 29, pp. 8494–8503, Jul. 2012, doi: 10.1021/jp212541y.

[239] F. Massi and J. E. Straub, “Probing the Origins of Increased Activity of the E22Q ‘Dutch’ Mutant Alzheimer’s-Amyloid Peptide,” *Biophysical Journal*, vol. 81, pp. 697–709, 2001.

[240] A. M. Siddiquee, I. Y. Hasan, S. Wei, D. Langley, E. Balaur, C. Liu, J. Lin, B. Abbey, A. Mechler, and S. Kou, “Visualization and Measurement of the Local Absorption Coefficients of Single Bilayer Phospholipid Membranes Using

Scanning Near-field Optical Microscopy," *Biomedical Optics Express*, vol. 10, no. 12, p. 6569, Dec. 2019, doi: 10.1364/boe.10.006569.

[241] R. Smith and C. Tanford, "The Critical Micelle Concentration of I-a-dipalmitoylphophatidylcholine in Water and Water/methanol Solutions," *Journal of Molecular Biology*, vol. 67, no. 1, pp. 75–83, 1972.

[242] J. Roche, Y. Shen, J. H. Lee, J. Ying, A. Bax, J. Hnhα, J. C′c′, J. C′hα, J. Hαcα, and J. Ncα, "Monomeric Aβ 1−40 and Aβ 1−42 Peptides in Solution Adopt Very Similar Ramachandran Map Distributions That Closely Resemble Random Coil," *Biochemistry*, vol. 39, p. 34, 2021, doi: 10.1021/acs.biochem.5b01259.

[243] J. J. Kremer, M. M. Pallitto, D. J. Sklansky, and R. M. Murphy, "Correlation of Beta-amyloid Size and Hydrophobicity with Decreased Bilayer Fluidity of Model Membranes," *Biochemistry*, vol. 39, p. 23, 2000, doi: 10.1021/bi0001980.

[244] M. Yoda, T. Miura, and H. Takeuchi, "Non-electrostatic Binding and Self-association of Amyloid β-peptide on the Surface of Tightly Packed Phosphatidylcholine Membranes," *Biochemical and Biophysical Research Communications*, vol. 376, no. 1, pp. 56–59, Nov. 2008, doi: 10.1016/J.BBRC.2008.08.093.

[245] E. Y. Hayden and D. B. Teplow, "Amyloid β-protein Oligomers and Alzheimer's Disease," *Alzheimer's Reserach & Therapy*, vol. 5, no. 6, pp. 1–11, 2013, [Online]. Available: http://alzres.com/content/5/6/60

[246] W. C. Wimley and S. H. White, "Experimentally Determined Hydrophobicity Scale for Proteins at Membrane Interfaces," *Nature Structual Biology*, vol. 3, no. 10, pp. 842–848, 1996, [Online]. Available: http://www.nature.com/nsmb

[247] G. J. Hardy, R. Nayak, S. Munir Alam, J. G. Shapter, F. Heinrich, and S. Zauscher, "Biomimetic Supported Lipid Bilayers with High Cholesterol Content Formed by α-helical Peptide-induced Vesicle Fusion," *Journal of Materials Chemistry*, vol. 22, no. 37, pp. 19506–19513, Oct. 2012, doi: 10.1039/c2jm32016a.

[248] J. C. Lawrence, D. E. Saslowsky, J. M. Edwardson, and R. M. Henderson, "Real-Time Analysis of the Effects of Cholesterol on Lipid Raft Behavior Using Atomic Force Microscopy," *Biophysical Journal*, vol. 84, no. 3, pp. 1827–1832, Mar. 2003, doi: 10.1016/S0006-3495(03)74990-X.